

CHIRAL SYMMETRY RESTORATION IN QUANTUM FIELD THEORIES AT FINITE TEMPERATURE

UNIVERSITÄT DORTMUND



CHIRAL SYMMETRY RESTORATION IN
QUANTUM FIELD THEORIES AT
FINITE TEMPERATURE

Dissertation

zur Erlangung des Grades eines
Doktors der Naturwissenschaften
am Fachbereich Physik
der Universität Dortmund

vorgelegt von

Stefan Michalski

Oktober 2006



Universität Dortmund

Tag der mündlichen Prüfung; 12. Januar 2007

Vorsitzender: Prof. Dr. M. Tolan

Erster Gutachter: Prof. Dr. J. Baacke

Zweiter Gutachter: Prof. Dr. D. Rischke

Vertreter der wissenschaftlichen Mitarbeiter: Priv.-Doz. Dr. R. Klingenberg

*There is something fascinating about science.
One gets such wholesale returns of conjecture
out of such a trifling investment of fact.*

MARK TWAIN

Contents

1	Introduction	1
1.1	Phase diagram of QCD	1
1.2	Chiral symmetry breaking	4
1.3	Experiments	6
1.4	Effective theories	6
1.5	Structure and goal of this thesis	7
1.6	Notations and conventions	8
I	Linear Sigma Models with Two Quark Flavors	9
2	The $U(2)_L \times U(2)_R$ linear sigma model	11
2.1	Classical action and symmetry breaking	11
2.2	Effective action	13
2.2.1	$1/N_f$ expansion	13
2.2.2	Leading order	14
2.2.3	Next-to-leading order	15
2.3	Equations of motion	17
3	The $O(N)$ linear sigma model	19
3.1	Classical action and symmetry breaking	19
3.2	Effective action and equations of motion	20
4	Loop graphs at finite temperature	23
4.1	Preliminaries	23
4.2	One-loop graphs	23

4.3	Sunset graph	24
4.4	High-temperature approximations	26
5	Numerical Results	31
5.1	Parameter fixing	31
5.2	$O(4)$ model	35
5.2.1	Chiral limit	35
5.2.2	Explicit symmetry breaking	38
5.3	$U(2)_L \times U(2)_R$ model	40
5.3.1	Explicit symmetry breaking with a fixed axial anomaly	40
5.3.2	Temperature-dependent $U(1)_A$ anomaly	43
5.3.3	Chiral limit	46
6	Conclusions and outlook	51
II	Testing and Comparing Resummation Schemes	55
7	Introduction	57
8	Effective action in different resummation schemes	61
8.1	2PI effective action at NLO	61
8.2	2PPI effective action at NLO	67
8.3	1PI effective action with auxiliary fields at NLO	70
9	Numerical results	73
10	Conclusions and outlook	79
A	Effective action of the $U(2)_L \times U(2)_R$ linear sigma model	81
B	Computation of the sunset graph	91
B.1	Sunset graph at zero temperature	91
B.2	Sunset graph at finite temperature	93
C	$1/N$ expansion and resummation schemes	99

C.1	Counting 1PI graphs	99
C.1.1	Leading order	100
C.1.2	Next-to-leading order	103
C.1.3	Higher orders	107
C.2	2PPI effective action	108
C.2.1	General formalism	108
C.2.2	Leading order	109
C.2.3	Next-to-leading order	110
C.3	1PI effective action with an auxiliary field	111
C.3.1	The formalism	111
C.3.2	Leading order	112
C.3.3	Next-to-leading order	112
C.4	2PI effective action	114
C.4.1	General formalism	114
C.4.2	Leading order	115
C.4.3	Next-to-leading order	116
C.4.4	Comparison with 1PI formalism	117
C.5	Conclusion	118

Bibliography	119
---------------------	------------

Chapter 1

Introduction

1.1 Phase diagram of QCD

What happens to matter under extreme conditions, at extremely high temperatures and at very high pressure? Water at standard pressure (1013 hPa) and room temperature, will turn into steam when heated up to 100°C and it will freeze when cooled down below 0°C and form ice. If put under pressure the crystalline structure of ice will vary, different types of ice will occur. Does nuclear matter exhibit such a rich phase structure, too? Indeed, it does. The appropriate theory of the substructure of nuclear matter is *quantum chromodynamics* (QCD), the fundamental theory of the strong interaction. It describes the interaction of quarks and gluons and how they form hadrons, *e.g.* protons and neutrons which ordinary matter is made of. QCD has been found to be asymptotically free (GROSS and WILCZEK, 1973; POLITZER, 1973), *i.e.* the strength of the interaction decreases with smaller distances or, equivalently, with higher exchanged momenta. At high energies, *i.e.* at large temperatures or densities, the interactions may become so small that quarks and gluons are no longer confined (COLLINS and PERRY, 1975) but form a new state of matter, called *quark-gluon plasma*.

A conjectured phase diagram of QCD is shown in Fig. 1.1. From that diagram one can read off the phase of (QCD) matter at a certain temperature and baryon chemical potential, where the latter can be considered as a measure for pressure and density at this point in the phase diagram.¹ To give an example, nuclear matter at zero temperature exists at a baryon chemical potential of about 922 MeV. It is a mixed phase as it consists of droplets of matter (atomic nuclei) and merely

¹The relation between chemical potential and number density, *e.g.*, is not linear so that at one chemical potential mixed states of different values of the density are allowed.

vacuum surrounding them. The line in the phase diagram starting at $T = 0$ and $\mu_B = 922$ MeV separates a liquid from a vapour phase of nuclear matter. The line is expected to have a critical endpoint at a temperature of about some 10 MeV and a chemical potential of about 900 MeV.

Starting with (liquid) nuclear matter at zero temperature we increase the pressure, and hence the chemical potential μ_B , more and more. At some point there is a transition to a phase of higher entropy dominated by quark degrees of freedom. With qualitative arguments it is possible to estimate where this transition takes place: The specific volume of nuclear matter at zero temperature and in the ground state is given by the reciprocal value of the number density of nucleons $n_B^{-1} \sim 6 \text{ fm}^3$. Increasing the density by a factor of three or more makes the nucleons overlap because they occupy a volume of about 2 fm^3 . At densities of several times the ground state density of nuclear matter the substructure, *i.e.* quarks and gluons, become important. For degenerate neutron matter the transition is at a density of about one nucleon per fm^3 or $\mu \simeq 1200$ MeV and the density suddenly increases by a factor of two to five (see *e.g.* HANDS, 2001, and references therein). At ultra-high densities it is favorable for quarks to form COOPER pairs in the color-flavor-locked (CFL) phase of color superconductivity (see *e.g.* RISCHKE, 2004). The nature of quark matter in the intermediate pressure region below the phase boundary to the CFL phase is not known very well; there might be other phases of color superconductivity or suprafluidity or something different. Nature may have realized the states with low temperature and high pressure only in the cores of neutron (or compact) stars which are difficult to access experimentally. However, it is possible to observe their cooling, spin-down, and precession to obtain information about the properties of their inner core.

At low temperature and low pressure nuclear matter behaves like an ensemble of nucleons inside a thermal bath of hadrons (mesons and baryons). At small densities (small baryon chemical potential) most of the thermal bath consists of pions. In a non-interacting classical system of particles the hadron number density for each species i is proportional to (RISCHKE, 2004)

$$n_i \sim m_i^2 T K_2\left(\frac{m_i}{T}\right) e^{\mu_i/T} ,$$

where m_i is the mass, μ_i the chemical potential and $K_2(x)$ is a modified BESSEL function of the second kind. Consequently, with increasing temperature the number density also increases such that above a certain temperature nucleon wavefunctions tend to overlap even for zero chemical potential; a description in terms of hadrons becomes inappropriate. So, at sufficiently low chemical potentials and temperatures $T < \Lambda_{\text{QCD}} \sim 200$ MeV nuclear matter is a gas of hadrons. But for temperatures

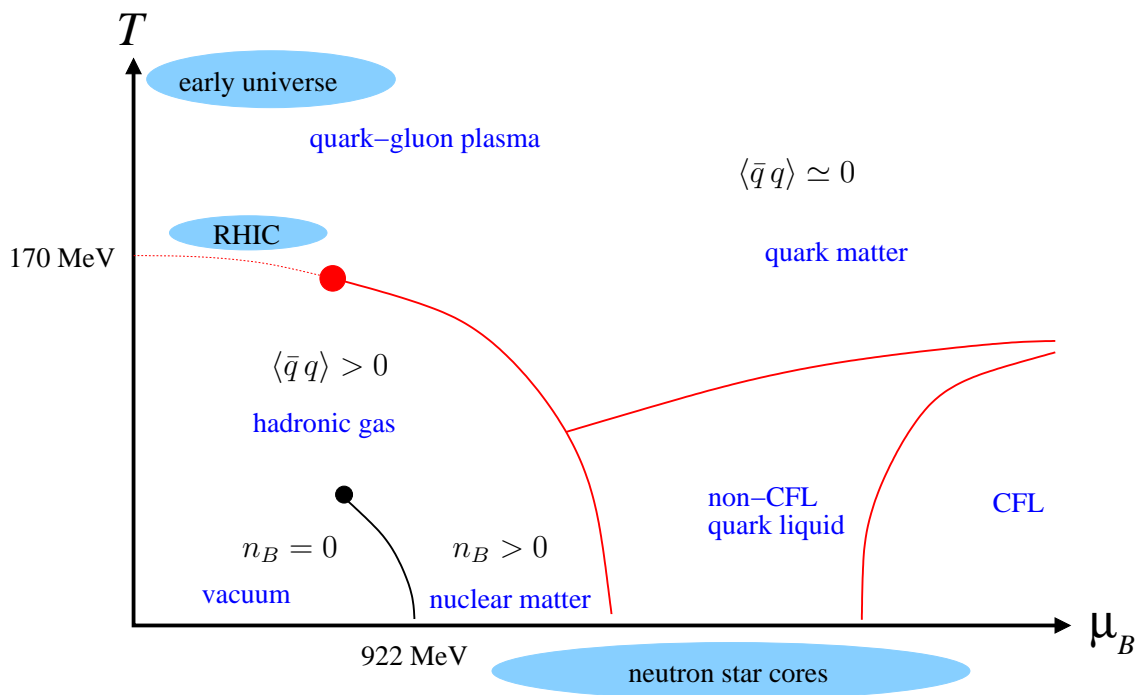


Figure 1.1: QCD phase diagram.

much greater than Λ_{QCD} thermal fluctuations break up the hadrons so that quarks and gluons are deconfined and freely flow in a plasma. The phase diagram (Fig.1.1) shows a crossover from the hadronic gas phase to the quark gluon plasma at $T \simeq 170$ MeV and zero baryon chemical potential. Lattice calculations indicate that such a state exists (see *e.g.* KARSCH, 2002). Probably, nature has realized a state of such high temperatures and low pressure only once; those conditions were found in the very early universe about 10^{-6} seconds after the Big Bang. The universe expanded and cooled down more or less along the T -axis and went through a crossover from the QGP phase, where quarks and gluons are deconfined, to the hadronic phase. At higher chemical potentials and lower temperatures one believes to find a phase transition of first-order between the confined (hadronic) and the QGP phase. This phase boundary goes down to zero temperature but also has a critical endpoint (marked with a circle in Fig.1.1) at which phenomena like critical opalescence are expected. Lattice calculations estimate the position of this endpoint to be at a temperature of $T_E \approx 0.95 T_c$ and at a baryon chemical potential of $\mu_B^E \approx 1.1 T_E$, where T_c is the crossover temperature at zero chemical potential (GAVAI and GUPTA, 2006a,b).

A comprehensive analysis of the phase structure of two-flavor massless QCD has been performed by HALASZ *et al.* (1998) using available experimental knowledge of QCD, insights gained from various models, as well as general and model-independent arguments. More about the physics of the quark-gluon plasma can be found in review articles (see *e.g.* HANDS, 2001; RISCHKE, 2004) or in a summary of a recent state of research (MÜLLER, 2005).

1.2 Chiral symmetry breaking

The LAGRANGE density of *massless* quantum chromodynamics (QCD) in a chiral representation reads

$$\mathcal{L}_{\text{QCD}} = \bar{\psi}_L^{(i,\alpha)} (i\gamma^\mu \partial_\mu + g \gamma^\mu \mathbf{A}_\mu) \psi_L^{(i,\alpha)} + \bar{\psi}_R^{(i,\alpha)} (i\gamma^\mu \partial_\mu + g \gamma^\mu \mathbf{A}_\mu) \psi_R^{(i,\alpha)} - \frac{1}{4} F_{\mu\nu}^a F^{a,\mu\nu}. \quad (1.1)$$

A summation over the flavor index $i = 1 \dots N_f$ and the color index $\alpha = 1 \dots N_c$ is implied here. The field $\mathbf{A}^\mu = \sum_{a=1}^{N_c^2-1} T_a A_a^\mu$ is a superposition of $N_c^2 - 1$ gluon fields where T_a are the generators of $SU(N_c)$. The gluons and their interactions are represented by $F_{\mu\nu}^a$.

Massless QCD has a variety of symmetries. It is a non-ABELian $SU(N_c)$ gauge theory, *i.e.*, invariant under local $SU(N_c)$ transformations. Nature has realized

three colors ($N_c = 3$), red, green and blue. Furthermore, there is a global chiral $SU(N_f)_L \times SU(N_f)_R$ and an (axial) $U(1)_A$ symmetry. It also conserves baryon number which results in a $U(1)_V$ symmetry.

At low temperatures, a chiral quark condensate $\langle \bar{q}q \rangle$ spontaneously breaks the axial part [$SU(N_f)_A \times U(1)_A \simeq U(N_f)_A$] of the symmetry and generates N_f^2 GOLDSTONE bosons. For two flavors ($N_f = 2$) these are three pions and the η meson. Apart from that there is an explicit violation of the $U(1)_A$ symmetry by instantons ('T HOOFT, 1976a,b; PISARSKI and WILCZEK, 1984) giving mass to one of the GOLDSTONE bosons (the η meson for $N_f = 2$).

Adding mass terms like $m_q \bar{\psi}\psi = m_q (\bar{\psi}_L\psi_R + \bar{\psi}_R\psi_L)$ to QCD breaks chiral symmetry explicitly and gives all GOLDSTONE bosons a mass. As the masses of the *up* and *down* quarks are very small (compared to the other four) the so-called unflavored (*i.e.* only made of *u* and *d* quarks and antiquarks) pseudo-GOLDSTONE mesons (the pions for $N_f = 2$) are relatively light (about 140 MeV). For three flavors, the kaons turn out to be pseudo-GOLDSTONE bosons as well, though their mass is three times as large as that of the pions due to the mass of the strange quark ($m_s \sim 100$ MeV).

At high temperatures chiral symmetry is expected to be restored. For finite quark masses this happens in a crossover transition such that the symmetry is (almost) restored when the temperature (to the third power) is of the order of the condensate, *i.e.* $\langle \bar{q}q \rangle^{1/3} \approx 300$ MeV. Recently, lattice QCD has been able to determine the critical temperature of the chiral phase transition. For three flavors it has been found to be in the vicinity of 155 MeV while for two flavors it is about 170 MeV for a vanishing quark chemical potential (AOKI *et al.*, 2006; KARSCH, 2002; LAERMANN and PHILIPSEN, 2003).

Unfortunately, the deconfinement and the chiral phase transition do not coincide in QCD. Furthermore, with quark degrees of freedom there is no order parameter connected with the deconfinement transition.² Yet there is an order parameter describing the chiral symmetry of QCD: the chiral quark-antiquark condensate $\langle \bar{q}q \rangle$. With zero quark masses QCD is chirally symmetric under $SU(N_f)_L \times SU(N_f)_R$ transformations but the ground state only exhibits an (approximate) $SU(N_f)_V$ flavor symmetry (still for zero quark masses). We will make use of the order parameter of chiral symmetry to investigate the restoration of this symmetry at finite temperature.

²Pure $SU(N_c)$ gauge theory, *i.e.* $N_f = 0$, has a global $Z(N_c)$ symmetry that is spontaneously broken by POLYAKOV loops at high temperatures but the fermionic mass term breaks the $Z(N_c)$ symmetry explicitly.

1.3 Experiments

Certain regions of the QCD phase diagram are probed by colliding heavy nuclei (gold, lead) at relativistic energies. Such experiments have been performed at the *Super Proton Synchrotron* (SPS) at CERN. At the moment, collisions of gold and lead nuclei are experimentally investigated at the *Relativistic Heavy Ion Collider* (RHIC) at Brookhaven National Laboratory (BNL). Future experiments will be done with the *Large Hadron Collider* (LHC) at CERN and with the SIS-200 (*Schwerionen-Synchrotron*) at GSI in Darmstadt. At RHIC, a typical collision takes place at a center-of-mass energy of 100-200 MeV per nucleon. Temperatures of about 175 MeV and baryon chemical potentials in the vicinity of 50 MeV are achieved.

One experimental signature for a possible creation of the quark-gluon plasma is the so-called jet quenching. A highly transverse jet should be correlated with another jet in the opposite direction due to momentum conservation. This correlation is measurable in heavy ion collisions, though at energies of about 200 GeV per nucleon it disappears. Obviously, one of the jets must be absorbed by an extremely hot and dense state of matter.

An indication of a restored chiral symmetry — which can but does not need to be directly correlated with the quark-hadron (deconfinement) phase transition — is a surplus production of strangeness. With a (partially) restored chiral symmetry the strange quark becomes as light as the up and down quarks so that the production of strange hadrons becomes “cheap” and more strangeness is found in the final state than expected from a broken chiral symmetry point of view.

1.4 Effective theories

Perturbative QCD is not applicable in the vicinity of the deconfinement transition because hadrons are bound states of QCD where the coupling constant is too large for a perturbative treatment.

Lattice calculations (see *e.g.* KARSCH, 2002) may provide first-principle results, but they suffer from technical difficulties for small quark masses (FODOR and KATZ, 2004) or for a chemical potential of the order of the temperature or larger (DE FORCRAND and PHILIPSEN, 2002).

Another nonperturbative approach to QCD is the construction of low-energy effective theories of hadrons with the same chiral symmetry. The color degrees of freedom are integrated out so that the low-energy behavior of QCD is governed by the lightest hadrons. Chiral perturbation theory (LEUTWYLER, 1994) is one representative

of such effective theories. It is based on the assumption that the low-energy behavior is governed by the pseudo-GOLDSTONE mesons (pions, kaons, η) and nucleons (see SCHERER and SCHINDLER, 2005, for a nice introduction).

NAMBU-JONA-LASINIO (NJL) models approximate the gluon exchange between quarks by a direct four-point interaction. These models are able to describe meson and nucleon properties very well, though QCD features like confinement and asymptotic freedom fall victim to the approximation.

Linear sigma models (GELL-MANN and LEVY, 1960) are probably the simplest examples for effective theories of QCD. However, since these models have the same symmetry as the underlying fundamental theory and thus belong to the same universality class they can be used to study the dynamics of phase transitions at finite temperature. PISARSKI and WILCZEK (1984) found that, for $N_f = 2$, there can be a second-order phase transition in presence of an explicitly broken $U(1)_A$ symmetry, whereas without this axial $U(1)$ anomaly the transition is of first order. The $O(4)$ linear sigma model belongs to the same universality class as the $U(2)_L \times U(2)_R$ model and therefore has a second-order phase transition as well.

Linear sigma models cannot be solved analytically so one has to make use of approximations. One problem arising at finite temperature is the breakdown of perturbation theory; at a temperature T , a perturbative expansion in powers of a coupling g yields a new mass scale gT that occurs in the denominators of loop graphs and cancels powers of the coupling constant in the perturbation expansion (BRAATEN and PISARSKI, 1990a,b; DOLAN and JACKIW, 1974a; PARWANI, 1992). So, terms of all orders of the coupling must be taken into account via resummation to avoid these unwanted cancellations. To ensure that we apply the resummation scheme embedded in the *two-particle irreducible* (2PI) effective action (CORNWALL *et al.*, 1974). As long as only local quantum corrections are considered it is identical to the *two-particle point-irreducible* (2PPI) effective action formalism (VERSCHTELDE and COPPENS, 1992).

1.5 Structure and goal of this thesis

This thesis consists of two parts. In the first one we investigate the $U(2)_L \times U(2)_R$ and the $O(4)$ linear sigma model at finite temperature within the formalism of the *two-particle irreducible* (2PI) effective action. We use a $1/N_f$ expansion and go a small step beyond the leading order by taking into account the two-loop sunset graph with combinatorial factors that are appropriate to a $1/N_f$ expansion.

The second part deals with a test for different resummation schemes concerning the

non-existence of GOLDSTONE bosons in two spacetime dimensions. We calculate the next-to-leading order of a $1/N$ expansion of the effective action of the $O(N)$ linear sigma model in different formalisms and investigate whether each formalism correctly reproduces this property.

1.6 Notations and conventions

Natural units are used as it is usual in high energy physics; all quantities, like energies, masses and temperatures are measured in MeV, *i.e.*, $\hbar = c = k_B = 1$ or, equivalently,

$$1 \text{ MeV} = (197.3 \text{ fm})^{-1} = 1.160 \times 10^{10} \text{ K} .$$

We use EINSTEIN's sum convention, *i.e.*, double indices are understood to be summed over unless explicitly mentioned. Latin indices from the beginning of the alphabet (a, b, c, \dots) run from 0 to $N_f^2 - 1$ (which mostly equals three). Latin indices from the middle of the alphabet (i, j, k, ℓ, \dots) start from one.

Finite-temperature integrals are performed with the MATSUBARA formalism. Effectively, an n -dimensional MINKOWSKIAN momentum integral is WICK-rotated and the integration over the zero component p^0 of the momentum is replaced by a summation over discrete MATSUBARA frequencies $p_n^0 = \omega_n = 2n\pi k_B T$. Consequently, the integration in momentum space changes to a combination of summation and integration

$$\int \frac{d^n p}{(2\pi)^n} f(p) \longrightarrow T \sum_{n=-\infty}^{\infty} \int \frac{d^{n-1} p}{(2\pi)^{n-1}} f(\omega_n, p) \equiv \int_p f(p) .$$

Part I

Linear Sigma Models with Two Quark Flavors

Chapter 2

The $U(2)_L \times U(2)_R$ linear sigma model

2.1 Classical action and symmetry breaking

Linear sigma models with a $U(N_f) \times U(N_f)$ symmetry and two to four quark flavors are not as popular among theorists as their $O(N)$ counterparts. However, within the last 25 years, they have been studied in the HARTREE-FOCK or one-loop approximation (see *e.g.* GEDDES, 1980; LENAGHAN *et al.*, 2000; RÖDER *et al.*, 2003; SCHAFFNER-BIELICH, 2000) and beyond (MICHALSKI, 2006).

The $U(N_f)_L \times U(N_f)_R$ linear sigma model contains two $U(N_f)$ isospin multiplets — a scalar and a pseudoscalar one — each of which is decomposed into an isosinglet and an $(N_f^2 - 1)$ -dimensional isospin multiplet. For two flavors we obtain four different mesons in the model, σ [called $f_0(600)$ nowadays] with an isotriplet of a_0 bosons in the scalar sector, and η with a pion triplet in the pseudoscalar sector.

The classical action of the $U(N_f)_L \times U(N_f)_R$ linear sigma model is given by

$$\begin{aligned} \mathcal{S}[\Phi] = \int_x \mathcal{L}[\Phi] = \int_x \left\{ \text{Tr} (\partial_\mu \Phi^\dagger \partial^\mu \Phi - m^2 \Phi^\dagger \Phi) - \frac{\lambda_1}{N_f^2} [\text{Tr} (\Phi^\dagger \Phi)]^2 - \frac{\lambda_2}{N_f} \text{Tr} [(\Phi^\dagger \Phi)^2] \right. \\ \left. + c [\det \Phi + \det \Phi^\dagger] + \text{Tr} [H(\Phi + \Phi^\dagger)] \right\}. \end{aligned} \tag{2.1}$$

The field Φ is a complex $N_f \times N_f$ matrix containing the scalar and pseudoscalar mesons,

$$\Phi = T_a(\sigma_a + i\pi_a). \tag{2.2}$$

Here σ_a are the scalar fields with $J^P = 0^+$ while π_a denotes the pseudoscalar ones with $J^P = 0^-$. They can be identified with the physical bosons (see *e.g.* RÖDER *et al.*, 2003)

$$\Phi = \frac{1}{\sqrt{2}} \begin{pmatrix} \frac{1}{\sqrt{2}}(\sigma + a_0^0) & a_0^+ \\ a_0^- & \frac{1}{\sqrt{2}}(\sigma - a_0^0) \end{pmatrix} + \frac{i}{\sqrt{2}} \begin{pmatrix} \frac{1}{\sqrt{2}}(\eta + \pi^0) & \pi^+ \\ \pi^- & \frac{1}{\sqrt{2}}(\eta - \pi^0) \end{pmatrix}. \quad (2.3)$$

The first three terms of the action (2.1) are invariant under symmetry transformations of the group $U(N_f)_L \times U(N_f)_R$

$$\Phi \rightarrow U_R \Phi U_L^\dagger \quad \text{where} \quad U_{R,L} = \exp(i\omega_{R,L}^a T_a). \quad (2.4)$$

This group is isomorphic to $U(N_f)_V \times U(N_f)_A$ where V denotes a vector and A an axial vector symmetry. Furthermore, any unitary group can be decomposed into a direct product of a special unitary group and a complex phase

$$U(N_f) \simeq SU(N_f) \times U(1),$$

so that

$$U(N_f)_L \times U(N_f)_R \simeq SU(N_f)_V \times SU(N_f)_A \times U(1)_A \times U(1)_V.$$

Chiral symmetry is spontaneously broken if the vacuum expectation value of the field Φ does not vanish

$$\langle \Phi \rangle = T_a \phi_a. \quad (2.5)$$

The vacuum should be of even parity, so only $\phi_a = \langle \sigma_a \rangle$ is allowed. According to a theorem by VAFA and WITTEN (1984) global vector-like symmetries (isospin, baryon number) cannot be broken spontaneously; hence only the $U(N_f)_A$ symmetry in the $U(N_f)_L \times U(N_f)_R$ model is broken which produces N_f^2 GOLDSTONE bosons (*e.g.* η and three pions for $N_f = 2$). The remaining symmetry is $U(N_f) \simeq SU(N_f)_V \times U(1)_V$, the flavor symmetry of (massless) QCD and baryon number conservation. The determinants in the action (2.1) break the $U(1)_A$ symmetry explicitly which represents the $U(1)$ instanton axial anomaly ('T HOOFT, 1976b) whose strength is given here by the constant c . For $N_f = 2$, this anomaly makes the isosinglet GOLDSTONE boson η massive. The remaining $SU(2)_V$ isospin symmetry (of three pions) stays intact if we assume the masses of the up and down quark to be equal so that only the diagonal generator T_0 but not T_3 is broken. Consequently, the masses of all particles of one isovector are identical, *i.e.*, $m_{a_0^0} = m_{a_0^\pm}$ and $m_{\pi^0} = m_{\pi^\pm}$.

As we perform a $1/N_f$ expansion we choose the vacuum expectation value to scale with N_f

$$\langle \Phi \rangle = N_f T_0 \langle \sigma_0 \rangle = \frac{1}{\sqrt{2} N_f} N_f \langle \sigma_0 \rangle \mathbf{1}, \quad (2.6)$$

so that

$$\mathrm{Tr} [\langle\Phi\rangle]^2 = \frac{N_f}{2} \phi_0^2 \mathrm{Tr} \mathbf{1} = \frac{N_f^2}{2} \phi_0^2, \quad (2.7)$$

and the classical part of the action scales with a factor N_f^2 . Finally, the term including

$$H = N_f T_a h_a, \quad (2.8)$$

in the action (2.1) explicitly breaks chiral symmetry and makes also the pions massive. It resembles a mass terms $m_q \bar{\psi} \psi$ in QCD where H corresponds to the quark mass matrix and Φ to the quark condensate. We will only deal with the case $h_0 \neq 0$ and keep the $SU(2)$ isospin symmetry ($m_u = m_d$) conserved so that $h_3 = 0$. The terms that explicitly break the symmetry also scale with N_f^2 ,

$$\mathrm{Tr} [H (\langle\Phi\rangle + \langle\Phi^\dagger\rangle)] = N_f^2 h_0 \phi_0. \quad (2.9)$$

With rising temperature we expect the chiral $SU(2)_V \times SU(2)_A \simeq SU(2)_L \times SU(2)_R$ symmetry to be restored so that the chiral partners (σ and π , η and a_0) become degenerate in mass. A violation of the axial $U(1)$ symmetry is inherent in the linear sigma model since its strength is directly given by the model parameter c . The restoration of this symmetry can only be modelled in a phenomenological way by making c temperature-dependent, *e.g.*, go down with rising T . For $c \rightarrow 0$ we expect the η mass to become identical to the pion mass above a certain temperature so that there is a full $U(2)_A$ symmetry in the pseudoscalar sector. Together with a chiral symmetry restoration this would result in a total restoration of the (hidden) $U(2)_L \times U(2)_R$ symmetry.

2.2 Effective action

2.2.1 $1/N_f$ expansion

We compute the effective action using the 2PI formalism (CORNWALL *et al.*, 1974) and perform a $1/N_f$ expansion. All graphs of leading order (LO) and some next-to-leading-order (NLO) graphs are taken into account. Furthermore, we approximate the equations of motion so that they obey a $U(2)_L \times U(2)_R$ symmetry if there were no axial anomaly ($c = 0$).

The topology of the graphs at leading order is the same as in the HARTREE-FOCK approximation (see *e.g.* LENAGHAN *et al.*, 2000; RÖDER *et al.*, 2003) and in a two-loop approximation (MICHALSKI, 2006) but the combinatorial factors of the graphs in the equations of motion are different. The reader is referred to Appendix A for

details of the computation. In this section, we will only give the final result for the equations of motion. The effective action is a functional of the condensate ϕ_0 and the matrix of GREEN functions \mathbf{G} with elements like

$$G_{ab}^{S,P}(x, y) = \langle \sigma_a(x) \sigma_b(y) \rangle ,$$

where S and P mean scalar and pseudoscalar here. The equations of motion for \mathbf{G} and ϕ_0 follow from a stationarity condition of the effective action,

$$\delta\Gamma[\mathbf{G}, \phi] = 0 .$$

Furthermore, in the approximation to be studied here the effective action can be decomposed into a leading-order (LO) and a next-to-leading order part (NLO)

$$\Gamma[\mathbf{G}, \phi_0] = \Gamma^{\text{LO}}[\mathbf{G}, \phi_0] + \Gamma^{\text{NLO}}[\mathbf{G}, \phi_0] . \quad (2.10)$$

The effective action — as any classical action — contains a space-time integral over the effective potential

$$\Gamma = - \int_x V_{\text{eff}}$$

and a sign because the classical potential has a negative sign in the LAGRANGE density, too. We will use the two terms “effective action” and “effective potential” ambiguously.

2.2.2 Leading order

The effective action contains all *two-particle irreducible*¹ (2PI) graphs that can be constructed using the three- and four-particle vertices of the shifted action (see Appendix A for details). At leading order of a $1/N_f$ expansion we find the expression

$$\Gamma^{\text{LO}}[\mathbf{G}, \phi_0] = N_f^2 \mathcal{S}[\phi_0] + \Gamma_1^{\text{LO}}[\mathbf{G}, \phi_0] + \Gamma_{\text{db}}^{\text{LO}}[\mathbf{G}, \phi_0] \quad (2.11)$$

which scales with a factor of N_f^2 as we will see immediately. The classical potential is

$$N_f^{-2} V_{\text{cl}}(\phi_0) = \frac{1}{2}(m^2 - c) \phi_0^2 + \frac{(\lambda_1 + \lambda_2)}{4} \phi_0^4 - h_0 \phi_0 . \quad (2.12)$$

The term Γ_1 consists of one-loop graphs

$$\begin{aligned} \Gamma_1^{\text{LO}}[\mathbf{G}, \phi_0] &= \frac{i}{2} \left[\text{Tr } \mathcal{D}_\sigma^{-1} G_\sigma + \ln \det G_\sigma^{-1} + \text{Tr } \mathcal{D}_\eta^{-1} G_\eta + \ln \det G_\eta^{-1} \right] \\ &+ \frac{i}{2} (N_f^2 - 1) \left[\text{Tr } \mathcal{D}_{a_0}^{-1} G_{a_0} + \ln \det G_{a_0}^{-1} + \text{Tr } \mathcal{D}_\pi^{-1} G_\pi + \ln \det G_\pi^{-1} \right] , \end{aligned} \quad (2.13)$$

¹Graphs that do not fall apart if two lines are cut.

where \mathcal{D}_*^{-1} denotes the inverse tree-level propagators which are eigenvalues of the matrix of second derivatives of the classical action

$$i(\mathcal{D}_{ab}^S)^{-1} = \left. \frac{\delta^2 \mathcal{S}[\Phi]}{\delta \sigma_a \delta \sigma_b} \right|_{\phi_0} \quad \text{and} \quad i(\mathcal{D}_{ab}^P)^{-1} = \left. \frac{\delta^2 \mathcal{S}[\Phi]}{\delta \pi_a \delta \pi_b} \right|_{\phi_0} .$$

The leading order of the double bubble graphs reads

$$\begin{aligned} \Gamma_{\text{db}}^{\text{LO}}[\mathbf{G}] &= -\frac{(\lambda_1 + \lambda_2)}{4 N_f^2} \int_x \left[\sum_a (\Delta_{aa}^S + \Delta_{aa}^P) \right]^2 \\ &= -\frac{(\lambda_1 + \lambda_2)}{4 N_f^2} \int_x \left\{ [\Delta_\sigma + (N_f^2 - 1) \Delta_\pi]^2 + [\Delta_\eta + (N_f^2 - 1) \Delta_{a_0}]^2 \right. \\ &\quad \left. + 2 [\Delta_\sigma + (N_f^2 - 1) \Delta_\pi] [\Delta_\eta + (N_f^2 - 1) \Delta_{a_0}] \right\} . \end{aligned} \quad (2.14)$$

The bubble graphs are $\Delta_*(x) = G_*(x, x)$ or in momentum space

$$\Delta_* = \int_k G_*(k) \quad (2.15)$$

where $*$ stands for σ , a_0 , η or π . Note that Eq. (2.14) is fully $U(2)_L \times U(2)_R$ symmetric. To maintain this symmetry at leading order we do have to include terms like $\Delta_\sigma \Delta_\pi$ and even $\Delta_\sigma \Delta_\eta$ which have a prefactor of $1/N_f$ and $1/N_f^2$ in Eq. (2.14) when counting strictly. The reason for that is obvious in the symmetric phase; there, all masses — or at least those of the chiral partners — become identical so that $\Gamma_{\text{db}}^{\text{LO}} \sim N_f^2$.

2.2.3 Next-to-leading order

As we will only calculate solutions to the leading order of the DYSON-SCHWINGER equation we can omit all graphs of higher order without external fields ϕ_0 in the effective action. All two-loop graphs we take into account at next-to-leading order in the $1/N_f$ expansion are the sunsets, so

$$\Gamma^{\text{bLO}}[\mathbf{G}, \phi_0] = \Gamma_{\text{sunsets}}^{\text{NLO}}[\mathbf{G}, \phi_0]$$

which are given by (note the opposite sign)

$$\begin{aligned} \Gamma_{\text{sunsets}}^{\text{NLO}}[\mathbf{G}, \phi_0] = & +\phi_0^2 \int_x \int_y \left\{ \frac{(\lambda_1 + 3\lambda_2)^2}{N_f^2} [S_{\sigma\sigma\sigma} + (N_f^2 - 1) S_{\sigma a_0 a_0}] \right. \\ & + \frac{(\lambda_1 + \lambda_2)^2}{N_f^2} [S_{\sigma\eta\eta} + (N_f^2 - 1) S_{\sigma\pi\pi}] \\ & \left. + 2 \frac{\lambda_2^2}{N_f^2} [S_{\eta\eta\sigma} + (N_f^2 - 1) S_{\eta\pi a_0}] \right\}, \end{aligned} \quad (2.16)$$

where

$$S_{ijk}(x, y) = G_i(x, y) G_j(x, y) G_k(x, y)$$

denotes a sunset graph made of the particles i , j and k . A graphical representation of the sunsets can be found in Fig. 2.1. They arise from the possible decays of $\sigma \rightarrow \pi\pi$, $\sigma \rightarrow \eta\eta$ and $a_0 \rightarrow \eta\pi$. Note that $\Gamma_{\text{sunsets}}^{\text{NLO}}$ is of the order $\mathcal{O}(N_f^0)$ but contains terms with a prefactor proportional to $1/N_f^2$ that are needed to describe the decays of the σ meson to a pair of particles of the *complete* scalar or pseudoscalar $U(2)$ multiplets [and not only to the $SU(2)$ isovectors π and a_0]. Similarly, the η meson decays to a scalar and a pseudoscalar particle of a complete $U(2)$ multiplet. Consult Appendix A for details.

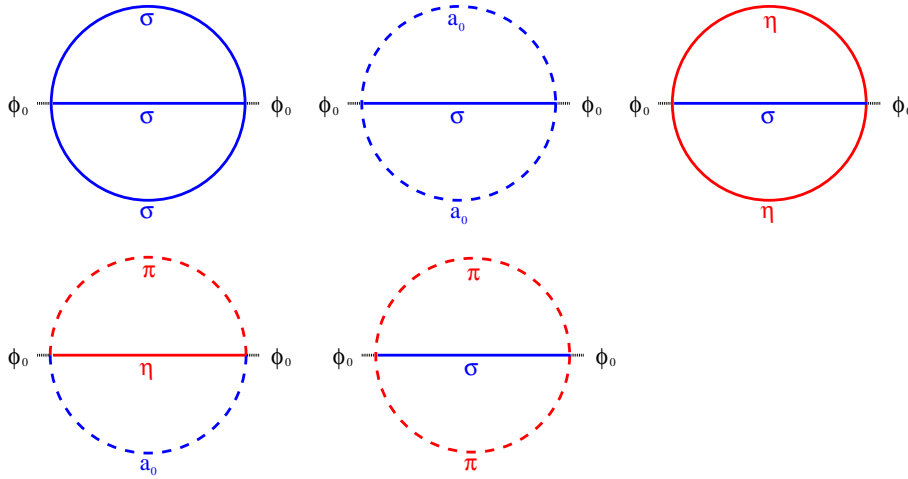


Figure 2.1: The sunset graphs as in Eq. (2.16). Scalars are drawn in blue, pseudoscalars in red. Dashed lines represent isotriplets while solid lines are used for isosinglets.

2.3 Equations of motion

To avoid contributions to any order of $1/N_f$ (cf. Appendix C for details) only leading-order contributions are resummed. The DYSON-SCHWINGER equations are derived from the leading order of the effective action

$$\frac{\delta\Gamma^{\text{LO}}[\mathbf{G}, \phi_0]}{\delta G_*} = 0 \quad \text{with} \quad * = \sigma, a_0, \eta, \pi .$$

Since the quantum corrections to the propagator are only local we can parametrize the GREEN function as

$$G_*(p) = \frac{i}{p^2 - M_*^2} \quad (2.17)$$

so that the DYSON-SCHWINGER equations explicitly read

$$M_\sigma^2 = m^2 - c + 3(\lambda_1 + \lambda_2)\phi_0^2 + \frac{(\lambda_1 + \lambda_2)}{N_f^2} \text{Tr } \Delta \quad (2.18a)$$

$$M_\pi^2 = m^2 - c + (\lambda_1 + \lambda_2)\phi_0^2 + \frac{(\lambda_1 + \lambda_2)}{N_f^2} \text{Tr } \Delta \quad (2.18b)$$

$$M_\eta^2 = m^2 + c + (\lambda_1 + \lambda_2)\phi_0^2 + \frac{(\lambda_1 + \lambda_2)}{N_f^2} \text{Tr } \Delta \quad (2.18c)$$

$$M_{a_0}^2 = m^2 + c + (\lambda_1 + 3\lambda_2)\phi_0^2 + \frac{(\lambda_1 + \lambda_2)}{N_f^2} \text{Tr } \Delta , \quad (2.18d)$$

where the trace is defined as

$$\text{Tr } \Delta = \Delta_\sigma + \Delta_\eta + (N_f^2 - 1)(\Delta_{a_0} + \Delta_\pi) .$$

The quantum corrections to all of the four masses are identical which reflects the $U(2)_L \times U(2)_R$ symmetry. Effectively the number of gap equations to be solved is only one because there are dependencies between all of the masses; for example the differences

$$M_\sigma^2 - M_\pi^2 = 2(\lambda_1 + \lambda_2)\phi_0^2$$

or

$$M_\eta^2 - M_\pi^2 = 2c$$

remain fixed for any temperature. So, without an axial anomaly ($c = 0$) the masses of the η meson and the pions are identical. This is a feature that is not realized in the HARTREE-FOCK (RÖDER *et al.*, 2003) and in the two-loop approximation (MICHALSKI, 2006) of the $U(2)_L \times U(2)_R$ linear sigma model at finite temperature. In these approximations, each gap equation contains different combinatorial

factors for each quantum correction. Effectively, this results in a violation of the $U(1)_A$ symmetry beyond tree-level that persists as long as chiral symmetry is broken (see MICHALSKI, 2006; RÖDER *et al.*, 2003, for details). However, in the approximation used here, the anomaly parameter c is the only quantity that determines the mass difference between the pions and the η meson.

Using the gap equations (2.18) the equation of motion of the condensate

$$\frac{\delta}{\delta\phi_0}\Gamma[\mathbf{G}, \phi_0] = 0$$

can be transformed to

$$\begin{aligned} h_0 = \phi_0 \left\{ M_\pi^2 + 2 \frac{\lambda_1 + \lambda_2}{N_f^2} \Delta_\sigma + 2 \frac{\lambda_2}{N_f^2} (N_f^2 - 1) \Delta_{a_0} \right. \\ \left. - \frac{(\lambda_1 + 3\lambda_2)^2}{N_f^4} [S_{\sigma\sigma\sigma} + (N_f^2 - 1) S_{\sigma a_0 a_0}] \right. \\ \left. - \frac{(\lambda_1 + \lambda_2)^2}{N_f^4} [S_{\sigma\eta\eta} + (N_f^2 - 1) S_{\sigma\pi\pi}] \right. \\ \left. - 2 \frac{\lambda_2^2}{N_f^4} [S_{\eta\eta\sigma} + (N_f^2 - 1) S_{\eta\pi a_0}] \right\}. \end{aligned} \quad (2.19)$$

Equations (2.18) and (2.19) will be numerically solved at finite temperature.

Chapter 3

The $O(N)$ linear sigma model

3.1 Classical action and symmetry breaking

The $O(N)$ linear sigma model has always served as a basic model for a quantum field theory with spontaneous symmetry breaking (BARDEEN and MOSHE, 1983; COLEMAN *et al.*, 1974; DOLAN and JACKIW, 1974b; KIRZHNITS and LINDE, 1975). It is by far more popular than its $U(N_f)_L \times U(N_f)_R$ sibling; it has been analyzed using different formalisms, where various authors used local resummations at leading order or the HARTREE-FOCK approximation (CHIKU and HATSUDA, 1998; DOLAN and JACKIW, 1974a; LENAGHAN and RISCHKE, 2000; NEMOTO *et al.*, 2000; PATKÓŠ *et al.*, 2002; PETROPOULOS, 1999; VERSCHELDE and DE PESSEMIER, 2002). The HARTREE-FOCK approximation exhibits a first-order phase transition whereas a second-order one is expected from universality class arguments (see *e.g.* LENAGHAN and RISCHKE, 2000; NEMOTO *et al.*, 2000; VERSCHELDE and DE PESSEMIER, 2002), a true artefact of the approximation. A two-loop calculation of the 2PPI effective action formalism at finite temperature reproduces the correct order of the phase transition (BAACKE and MICHALSKI, 2003a; SMET *et al.*, 2002). Recent progress was made using the two-particle irreducible effective action (ALFORD *et al.*, 2004; ANDERSEN *et al.*, 2004; BAACKE and MICHALSKI, 2004a,b; BERGES *et al.*, 2005; DE GODOY CALDAS, 2002; PARWANI, 1992; RÖDER, 2005; RÖDER *et al.*, 2005).

The linear sigma model with an $O(4)$ symmetry is closely connected to the $U(2)_L \times U(2)_R$ model discussed in the preceding chapter. In the limit of an infinite anomaly $c \rightarrow \infty$ with fixed $(m^2 - c) \rightarrow m_{O(4)}^2$ the masses of both the η and the a_0 mesons become infinite and thus these two mesons drop out of the spectrum. So, the σ meson and the three pions now share one $O(4)$ multiplet. Extending the isospin symmetry from $N_f^2 = 4$ to N dimensions we write down the well-known classical action of the

$O(N)$ linear sigma model

$$\mathcal{S}[\Phi] = \int_x \mathcal{L}[\Phi] = \int_x \left\{ \frac{1}{2} (\partial_\mu \Phi_a)^2 - \frac{1}{2} m^2 \Phi_a^2 - \frac{\lambda}{4N} (\Phi_a^2)^2 + h_a \Phi_a \right\}. \quad (3.1)$$

Here, the field $\Phi_a(x)$ is a component of an N -dimensional vector. The indices run from $a = 0$ to $N - 1$ to allow for a comparison with the $U(2)_L \times U(2)_R$ model. Through a finite expectation value

$$\langle \Phi_a \rangle = \sqrt{N} \phi_a \delta_{a0}$$

the $O(N)$ symmetry is spontaneously broken which yields $N - 1$ massless GOLDSTONE bosons (pions) and one massive σ meson. If $h_a \neq 0$ the symmetry is explicitly broken which gives the pions a finite mass.

Similar to an earlier analysis (BAACKE and MICHALSKI, 2003a,b) we will solve the equations of motion of the effective action taking into account contributions beyond HARTREE-FOCK or leading order but with combinatoric prefactors inspired by a $1/N$ expansion.

3.2 Effective action and equations of motion

As for the $U(2)_L \times U(2)_R$ model in Chapter 2 we construct the 2PI effective potential up to next-to-leading order of a $1/N$ expansion. At leading order we obtain

$$\begin{aligned} \Gamma^{\text{LO}}[G_\sigma, G_\pi; \phi_0] &= N \mathcal{S}[\phi_0] + \frac{i}{2} [\text{Tr } \mathcal{D}_\sigma^{-1} G_\sigma + \ln \det G_\sigma^{-1}] \\ &\quad + \frac{i}{2} (N - 1) [\text{Tr } \mathcal{D}_\pi^{-1} G_\pi + \ln \det G_\pi^{-1}] \\ &\quad - \frac{\lambda}{4N} [\Delta_\sigma + (N - 1) \Delta_\pi]^2. \end{aligned} \quad (3.2)$$

Restricting only to two-loop graphs with external fields, the relevant next-to-leading order contributions are given by

$$\Gamma^{\text{NLO}}[G_\sigma, G_\pi; \phi_0] = + \frac{\lambda^2}{N} \phi_0^2 \int_x \int_y [S_{\sigma\sigma\sigma} + (N - 1) S_{\sigma\pi\pi}], \quad (3.3)$$

where $S_{\sigma\sigma\sigma}$ and $S_{\sigma\pi\pi}$ denote sunset graphs depicted in Fig. 2.1.

The equations of motion are derived from the stationarity condition $\delta\Gamma = 0$. Here as well, we require that the mass gap equations are only derived from leading-order

contributions to the effective action $\delta\Gamma^{\text{LO}}/\delta G_* = 0$. So, we can also adopt the local *ansatz* (2.17) for the GREEN function which eventually leads to

$$M_\sigma^2 = m^2 + 3\lambda\phi_0^2 + \lambda[\Delta_\sigma + (N-1)\Delta_\pi] \quad (3.4a)$$

$$M_\pi^2 = m^2 + \lambda\phi_0^2 + \lambda[\Delta_\sigma + (N-1)\Delta_\pi] . \quad (3.4b)$$

Effectively, this is only one gap equation because the quantum corrections preserve the full $O(N)$ symmetry which makes the tree-level relation

$$M_\sigma^2 - M_\pi^2 = 2\lambda\phi_0^2$$

persist even at this order of a $1/N$ expansion.

The equation of motion for the condensate has the same structure as the one in the $U(2)_L \times U(2)_R$ model, Eq. (2.19),

$$h_0 = \left\{ M_\pi^2 + 2\frac{\lambda}{N}\Delta_\sigma - 2\frac{\lambda^2}{N^2}[S_{\sigma\sigma\sigma} + (N-1)S_{\sigma\pi\pi}] \right\} \phi_0 . \quad (3.5)$$

Equations (3.4) and (3.5) differ from those obtained in the HARTREE-FOCK (see *e.g.* LENAGHAN and RISCHKE, 2000; VERSCHELDE and DE PESSEMIER, 2002) and two-loop 2PPI approximation (BAACKE and MICHALSKI, 2003a,b) by combinatoric factors in front of the bubble graphs $\Delta_{\sigma,\pi}$ and the sunset $S_{\sigma\sigma\sigma}$.

Chapter 4

Loop graphs at finite temperature

4.1 Preliminaries

The effective action of the two models presented in the preceding two chapters contain FEYNMAN graphs that require regularization, *i.e.*, a prescription how to separate divergent parts of the corresponding momentum integrals from the finite ones. We will use dimensional regularization ('T HOOFT and VELTMAN, 1972) with $d = 4 - \epsilon$ and a modified minimal subtraction ($\overline{\text{MS}}$) renormalization scheme. It will turn out that the finite parts consist of a zero-temperature contribution and effects from interactions with the heat bath. Those are evaluated using the MATSUBARA formalism which makes the zero component of the momentum adopt only discrete values, the so-called MATSUBARA frequencies ω_n which are multiples of $2\pi T$.

4.2 One-loop graphs

The equations of motion contain the single bubble (or tadpole) graph Δ [Eq. (2.15)] which is given by the following expression (see *e.g.* BAACKE and MICHALSKI, 2003a).

$$\begin{aligned}\Delta_i &= \left(\frac{\bar{\mu}_R^2}{4\pi e^{-\gamma_E}} \right)^{\epsilon/2} T \sum_n \int \frac{d^{3-\epsilon}p}{(2\pi)^3} \frac{1}{(2\pi T)^2 + \mathbf{p}^2 + M_i^2} \\ &= \frac{1}{16\pi^2} M_i^2 \left[-\frac{2}{\epsilon} + \ln \frac{M_i^2}{\bar{\mu}_R^2} - 1 + \mathcal{O}(\epsilon) \right] + \frac{1}{2\pi^2} \int_0^\infty dp \frac{\mathbf{p}^2}{E_i(\mathbf{p})} n_i(\mathbf{p}) ,\end{aligned}\tag{4.1}$$

where $E_i(\mathbf{p}) = \sqrt{\mathbf{p}^2 + M_i^2}$, n_i the BOSE-EINSTEIN distribution function

$$n_i(\mathbf{p}) = \frac{1}{e^{E_i(\mathbf{p})/T} - 1}\tag{4.2}$$

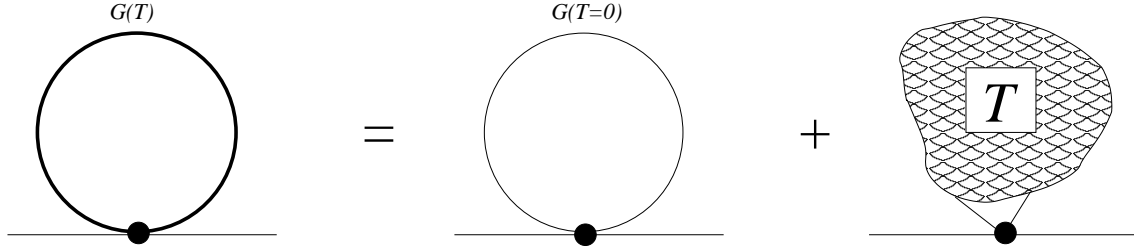


Figure 4.1: Schematic decomposition of the bubble graph that visualizes the interaction with the heat bath.

and $\bar{\mu}_R$ is the renormalization scale in the $\overline{\text{MS}}$ scheme.

We conclude from Eq. (4.1) that the bubble graph at finite temperature does not only describe an interaction with the vacuum fluctuations but also with (on-shell) particles from the heat bath (see Figure 4.1) which is mathematically represented by the BOSE-EINSTEIN distribution function. The propagation of a particle from a space-time point A to another point B in the presence of a heat bath can be split into two processes: the particle travels through the (zero-temperature) vacuum and does not care about the heat bath, or the heat bath absorbs the (on-shell) particle at A and emits another particle at B .

4.3 Sunset graph

The solution of the condensate equations of motion (2.19) and (3.5) require the evaluation of the sunset graph. Details concerning the computation of this graph can be found in Appendix B, here we will only give the relevant results.

In $4 - \epsilon$ dimensions, the vacuum part of the sunset graph with three different masses M_0 , M_1 and M_2 is given by the expression (VAN DER BIJ and VELTMAN, 1984)

$$(M_0|M_1|M_2) = \frac{1}{-1 + \epsilon} \left\{ M_0^2(M_0M_0|M_1|M_2) + M_1^2(M_1M_1|M_0|M_2) + M_2^2(M_2M_2|M_0|M_1) \right\}, \quad (4.3)$$

where, using the $\overline{\text{MS}}$ prescription,

$$\frac{1}{-1+\epsilon}(M, M|M_1|M_2) = \frac{1}{(4\pi)^4} \left[-\frac{2}{\epsilon^2} - \frac{2}{\epsilon} \left(\frac{3}{2} - \ln \frac{M^2}{\bar{\mu}_R^2} \right) - \frac{7}{2} - \frac{\pi^2}{12} - \left(\ln \frac{M^2}{\bar{\mu}_R^2} \right)^2 + \ln \frac{M^2}{\bar{\mu}_R^2} - f(a, b) \right] + \mathcal{O}(\epsilon) . \quad (4.4)$$

The function $f(a, b)$ contains dilogarithms or SPENCE integrals

$$f(a, b) = -\frac{1}{2} \ln a \ln b - \left(\frac{a+b-1}{\sqrt{\Delta}} \right) \left[\text{Sp} \left(\frac{-x_2}{y_1} \right) + \text{Sp} \left(\frac{-y_2}{x_1} \right) + \frac{1}{4} \ln^2 \frac{x_2}{y_1} + \frac{1}{4} \ln^2 \frac{y_2}{x_1} + \frac{1}{4} \ln^2 \frac{x_1}{y_1} - \frac{1}{4} \ln^2 \frac{x_2}{y_2} + \frac{\pi^2}{6} \right] , \quad (4.5)$$

with

$$\Delta = 1 - 2(a+b) + (a-b)^2, \quad x_{1,2} = \frac{1}{2} \left(1+b-a \pm \sqrt{\Delta} \right), \quad y_{1,2} = \frac{1}{2} \left(1+a-b \pm \sqrt{\Delta} \right) \quad (4.6)$$

and

$$a = \frac{M_1^2}{M^2}, \quad b = \frac{M_2^2}{M^2} .$$

At mass thresholds, *i.e.* when the sum of two of the particles in the sunset approaches the mass of the third particle from above or below, the function $f(a, b)$ must be expanded about the relevant points to be properly evaluated which is a lengthy calculation. Fortunately, there is a software library available (MARTIN and ROBERTSON, 2006) which provides the sunset graph at zero temperature.

Concerning the interaction with particles from the heat bath one can distinguish the cases in which either one or two propagators become “thermal” so that a sunset graph with three different masses M_i , M_j and M_k reads

$$S_{ijk} = (M_i|M_j|M_k) + S_{(i)jk} + S_{(j)ki} + S_{(k)ij} + S_{(ij)k} + S_{(jk)i} + S_{(ki)j} . \quad (4.7)$$

Here, $(M_i|M_j|M_k)$ is given by Eq. (4.3) and $S_{(i)jk}$ is the sunset with i being a thermal line [cf. Eqs. (B.19) and (B.20) on p. 97], and $S_{(ij)k}$ denotes a sunset graph with two thermal lines i and j [see Eq. (B.18) on p. 96]. Figure 4.2 schematically shows the different interactions with the heat bath. Explicitly for a σ - π sunset Eq.(4.7) becomes

$$S_{\sigma\pi\pi} = (M_\sigma|M_\pi|M_\pi) + S_{(\sigma)\pi\pi} + 2 S_{(\pi)\sigma\pi} + 2 S_{(\sigma\pi)\pi} + S_{(\pi\pi)\sigma} .$$

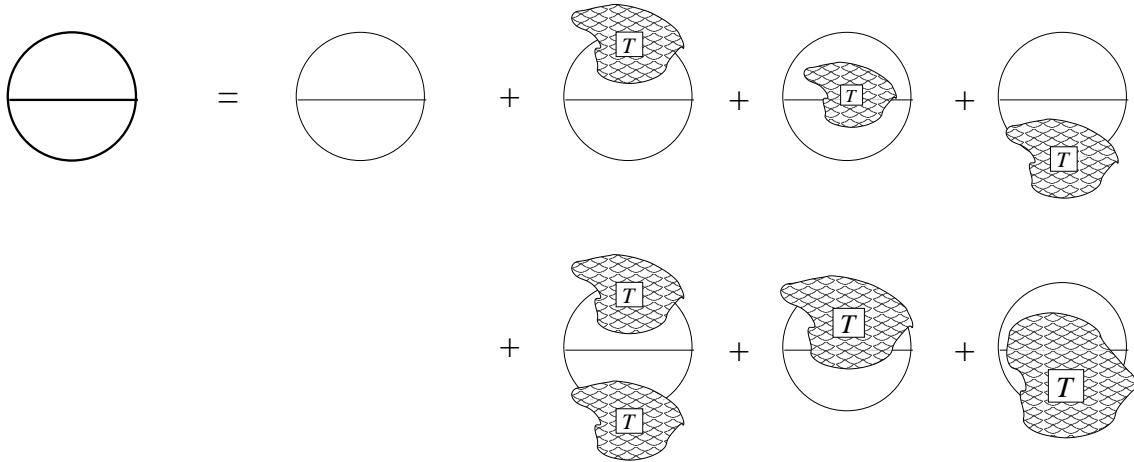


Figure 4.2: Thermal and vacuum parts of the sunset graph as in Eq. (4.7).

4.4 High-temperature approximations

At high temperatures, $T \gg M$, the thermal integrals can be approximated by a so-called high temperature expansion in powers of M/T which, *e.g.*, yields for the bubble graphs (4.1)

$$\Delta_i = \frac{T^2}{12} + \mathcal{O}(M_i T) .$$

The vacuum part of this graph is zero in the limit $M \rightarrow 0$. We expect a crossover in our models, *i.e.*, we cannot expect all masses to obey the condition for this high-temperature approximation. Only in the chiral limit we can use this to estimate the critical temperature making certain assumptions.

Another way to deal with vacuum loop divergences has been proposed by BOCHKAREV and KAPUSTA (1996). They claim that by ignoring terms from vacuum fluctuations they performed a relativistic virial expansion with the S matrix evaluated at tree level. Qualitative changes were not to be expected since the physics is dominated by long wavelengths (BOCHKAREV and KAPUSTA, 1996). This approach has been also used by RÖDER *et al.* (2003), SCHAFFNER-BIELICH (2000) and LENAGHAN *et al.* (2000) for $U(N_f)_L \times U(N_f)_R$ linear sigma models and by LENAGHAN and RISCHKE (2000) for the $O(N)$ model with results comparable with lattice data (*e.g.* KARSCH, 2002).

However, we check the validity of this approximation by comparing it to the results including finite regularization terms. As a preliminary example let us consider the simple bubble-shaped mass correction (4.1). At fixed renormalization scale it is a

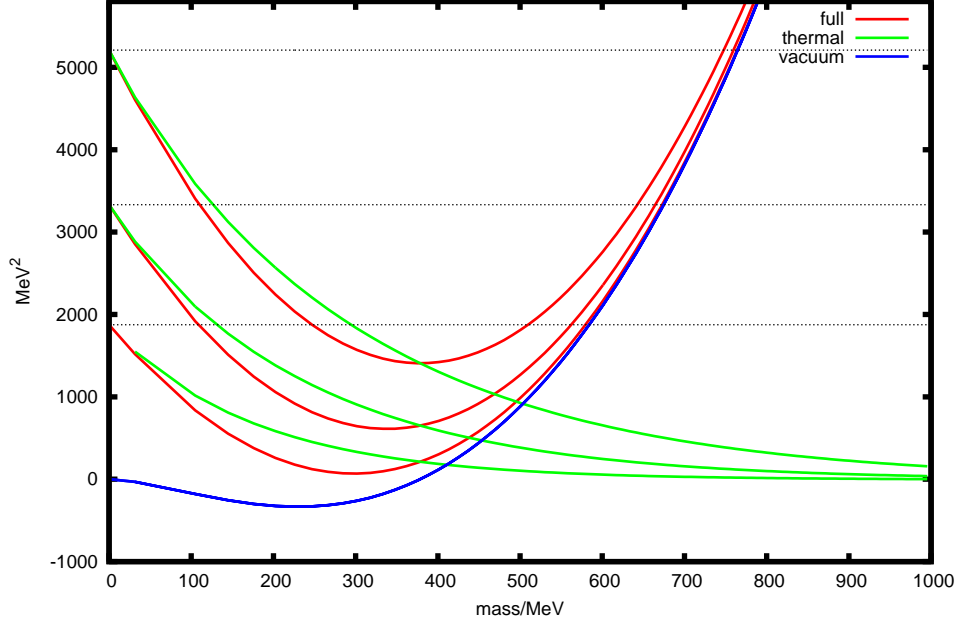


Figure 4.3: Bubble graph at temperatures of 250, 200 and 150 MeV (top to bottom) as a function of the mass. The dotted lines mark the zero-mass limit $T^2/12$ and the blue curve is the vacuum part for $\bar{\mu}_R = 230$ MeV.

function of temperature and the mass running inside the loop. For $\bar{\mu}_R = 230$ MeV we plot this function at different temperatures in Fig. 4.3. In this example, the finite renormalization terms are only negligible relative to the thermal part if $M \ll T$ or $\ln \frac{M^2}{\bar{\mu}_R^2} \approx 1$. For linear sigma models this means that all masses and the renormalization scale have to be almost the same. This can only be possible if the symmetry is (almost) restored because the difference between the masses depends on the value of the condensate. At low temperatures, the condensate takes large values and consequently the masses of the lightest and the heaviest meson differ by a factor of up to seven. So we expect to get quantitatively different results when including finite renormalization terms in a temperature region where a crossover transition takes place and all masses still differ from one another.

Comparing full thermal results with those in the unrenormalized case means, in general, comparing equations in which the parameters have different values. So, one might argue that this is an unfair comparison since, in general, the coupling constants run with the renormalization scale such that the product of coupling and the quantum corrections can remain (more or less) unchanged. But the approximation

we choose results in coupling constants which are independent of the renormalization scale so that the prefactors of the renormalized and “unrenormalized” quantum corrections are indeed well comparable.

Nevertheless, we can expect that the solutions of the mass gap equations (2.18) and (3.4) will be significantly different in both cases because the thermal part of the bubble graph $\Delta(M^2)$ is a monotonic function of the mass square M^2 whereas the vacuum part is not (Fig. 4.3). Furthermore, the latter scales with the mass squared so that the value of the full graph can even exceed the high-temperature (zero-mass) value of $T^2/12$.

To assess the difference between the renormalized and the unrenormalized case for the temperature dependence of the condensate we have to investigate the sunset graph more thoroughly. The purely thermal part is obtained by removing all zero-temperature contributions from the graph itself *and all its subgraphs*

$$S_{ijk}^{\text{HE}} = S_{ijk} - S_{ijk}|_{T=0} = S_{(ij)k} + S_{(jk)i} + S_{(ki)j} . \quad (4.8)$$

In Figure 4.4 we show the functions $S_{\sigma\pi\pi}(M_\pi)|_{M_\sigma=500 \text{ MeV}}$ and $S_{\sigma\sigma\sigma}(M_\sigma)$. The renormalization terms do make a difference; without those terms the $\sigma\sigma\sigma$ -sunset monotonically decreases with the mass but remains positive for any value of the mass [cf. Fig. 4.4(b)] whereas the vacuum terms change this behavior. For both sunsets the greatest difference between the full results and the purely thermal part is obviously made by the subprocess in which only one of the three particles comes from the heat bath. It contributes several times as much as the purely thermal part and can even have the opposite sign.

Furthermore, there is a logarithmic cusp in the purely thermal part of $S_{\sigma\pi\pi}$ at the threshold $M_\sigma \approx 2 M_\pi$. We conclude that there must be another cusp (with opposite sign) in the sunset with one thermal line because the full result is smooth again. Like the bubble graph the (vacuum part of the) sunset also scales with the mass such that it exceeds the thermal part by orders of magnitude at sufficiently high masses. By numerical computation we find $S_{\sigma\sigma\sigma}(M_\sigma = 0) = \frac{T^2}{13.375}$ at $\bar{\mu}_R = 220 \text{ MeV}$ with a relative error of 10^{-6} in a mass range from 10 MeV to 1 GeV.

In general we can conclude from these examples that, at least quantitatively, the results will depend on whether we include vacuum terms or not and what value we choose for the renormalization scale.

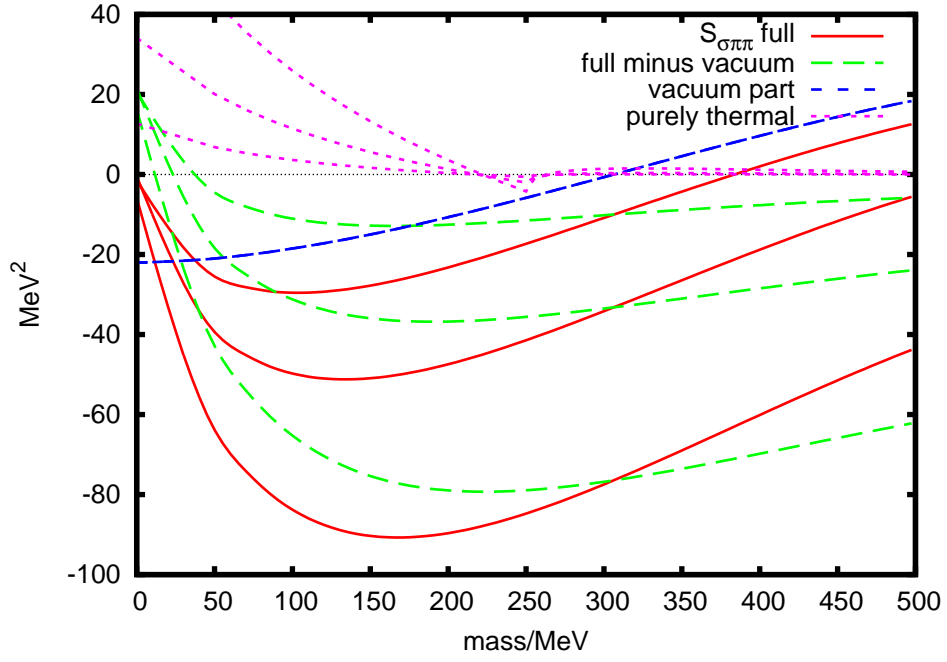
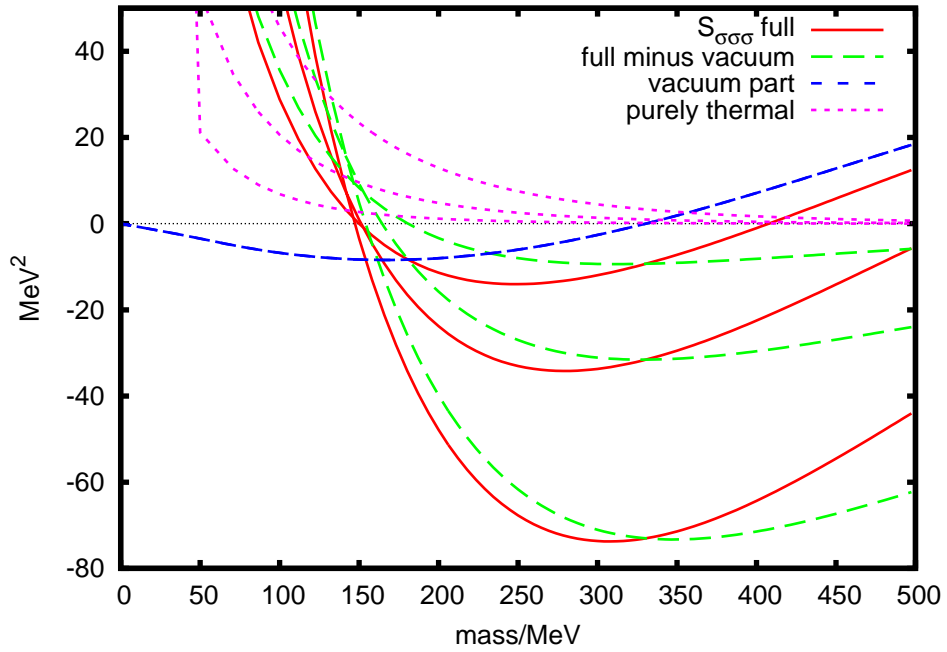

 (a) Sunset $S_{\sigma\pi\pi}$ as a function of M_π for $M_\sigma = 500$ MeV.

 (b) Sunset $S_{\sigma\sigma\sigma}$ as a function of M_σ

 Figure 4.4: Different contributions to sunset graphs at temperatures of 250, 200 and 150 MeV (bottom to top for the full results and top to bottom for the purely thermal part). The vacuum part is evaluated for $\bar{\mu}_R = 217$ MeV.

Chapter 5

Numerical Results

5.1 Parameter fixing

The parameters in both linear sigma models are fixed such that at zero temperature the values of all masses are equal to the values given by Particle Data Group (EIDELMAN *et al.*, 2004), cf. Table 5.1, where we choose the mass of the σ meson to be 600 MeV in the $U(2)_L \times U(2)_R$ model and 400 MeV in the $O(4)$ model for reasons that will be elucidated later.

The value of the condensate ϕ_0 at zero temperature is related to the pseudoscalar meson decay constants f_a and determined by the PCAC (partial conservation of axial vector current) hypothesis

$$\langle 0 | \mathcal{J}_a^\mu | \pi_a \rangle \equiv i p^\mu f_a . \quad (5.1)$$

Here, f_a is the decay constant of the axial field π_a , and the (axial-vector) NOETHER current \mathcal{J}_a^μ follows from the infinitesimal form of the $U(2)_L \times U(2)_R$ symmetry

particle	Particle masses	
	ESB	chiral limit
σ	400 to 600 MeV	400 to 600 MeV
π	139.6 MeV	0 MeV
a_0	984.7 MeV	984.7 MeV
η	547.8 MeV	547.8 MeV

Table 5.1: Meson masses for explicit symmetry breaking and in the chiral limit. Note that, of course, there is no a_0 and η meson in the $O(4)$ model.

transformation (2.4)

$$T_a(\sigma_a + i\pi_a) \rightarrow T_a(\sigma_a + i\pi_a) - i\omega_V^a [T_a, T_b](\sigma_b + i\pi_b) + i\omega_A^a \{T_a, T_b\}(\sigma_b + i\pi_b).$$

For only axial-vector transformations, $\omega_V^a = 0$, the associated current is

$$\mathcal{J}_a^\mu \equiv \frac{\delta \mathcal{L}}{\delta(\partial_\mu \phi_c)} i d_{abc} \phi_b + \text{h.c.} = d_{abc} (\sigma_b \partial^\mu \pi_c - \pi_b \partial^\mu \sigma_c). \quad (5.2)$$

Inserting this current into the PCAC relation (5.1) we obtain

$$f_a = d_{aab} \langle \sigma_b \rangle \equiv \phi_b$$

without summation over a . For $N_f = 2$, this fixes the condensate to $\langle \sigma_0 \rangle = f_\pi$. And as we scaled the field by a factor of N_f , we set

$$N_f \phi_0 \equiv f_\pi = 92.4 \text{ MeV} \quad (\text{or } 90 \text{ MeV in the chiral limit}).$$

In both models at tree-level, the parameter fixing can be done in a unique way because there are as many equations of motion as parameters. In the chiral limit (h_0 fixed to zero) the equation for the condensate coincides with the one for the pion mass. Difficulties occur if one wants to include quantum corrections because such terms contain a renormalization scale $\bar{\mu}_R$ which, normally, every parameter of the theory depends on. This becomes most obvious in the chiral limit: as soon as the equation for the condensate is no longer equivalent to the pion mass gap equation there are five different equations of motion in the $U(2)_L \times U(2)_R$ linear sigma model but only four parameters (two couplings, m^2 and the anomaly strength c). The renormalization scale $\bar{\mu}_R$ serves as the fifth parameter which implies that there is a limited number of discrete values of the renormalization scale $\bar{\mu}_R$ for which the parameters can be fixed.

The gap equations (2.18) differ from their tree-level counterparts through quantum corrections but, nevertheless, three of the five parameters are independent of the renormalization scale; differences of two mass squares depend on the anomaly strength c and the two couplings λ_1 and λ_2 which all take the tree-level values.

$$c = \frac{M_\eta^2 - M_\pi^2}{2} \quad (5.3a)$$

$$\lambda_1 = \frac{M_\sigma^2 + M_\eta^2 - M_{a_0}^2 - M_\pi^2}{2\phi_0^2} \quad (5.3b)$$

$$\lambda_2 = \frac{M_{a_0}^2 - M_\eta^2}{2\phi_0^2}. \quad (5.3c)$$

Only m^2 varies with the renormalization scale $\bar{\mu}_R$ such that the sum of m^2 and the quantum corrections remains $\bar{\mu}_R$ -independent

$$m^2 = \frac{2 M_\pi^2 + M_\eta^2 - M_\sigma^2}{2} - \frac{M_\sigma^2 - M_\pi^2}{2 \phi_0^2 N_f^2} [\Delta_\sigma + \Delta_\eta + (N_f^2 - 1) (\Delta_{a_0} + \Delta_\pi)] . \quad (5.4)$$

These considerations can also be applied to the $O(N)$ model where the parameters are given by

$$\lambda = \frac{M_\sigma^2 - M_\pi^2}{2 \phi_0^2} \quad (5.5a)$$

$$m^2 = -\frac{M_\sigma^2 - 3 M_\pi^2}{2} - \frac{M_\sigma^2 - M_\pi^2}{2 \phi_0^2 N} [\Delta_\sigma + (N - 1) \Delta_\pi] . \quad (5.5b)$$

We notice that $\lambda_1 + \lambda_2 = \lambda$.

The symmetry-breaking parameter h_0 in the condensate's equation of motion (2.19) is determined by the sunset terms and scales with $\bar{\mu}_R$ as shown by Fig. 5.1. Assuming that the effective potential does not differ qualitatively from the classical one, we shall require $h_0 > 0$ to ensure that for zero temperature the slope of the potential at ϕ_0 is negative. Otherwise the first extremum in the effective potential (the one at lowest possible positive ϕ_0) is a maximum instead of a minimum.

In the $U(2)_L \times U(2)_R$ model with $M_\sigma = 600$ MeV we observe another difficulty. At renormalization scales beyond about 400 MeV the extremum at $\phi_0 = 92.4$ MeV is a *maximum* instead of a minimum: the right hand side of the condensate Eq. (2.19) exhibits a sign change from negative to positive values. With increasing temperature the position of this extremum moves towards higher values (“to the right”) over 100 MeV before it vanishes completely.

Furthermore, for $\bar{\mu}_R \gtrsim 500$ MeV a COLEMAN-WEINBERG phenomenon (COLEMAN and WEINBERG, 1973) can be observed because the mass parameter m^2 achieves positive values, *i.e.*, spontaneous symmetry breaking does no longer occur at tree-level but through radiative corrections in the effective potential.

Fixing parameters in the chiral limit requires $h_0 = 0$. In the $U(2)_L \times U(2)_R$ model this is possible only for $\bar{\mu}_R = 358.4$ MeV and $\bar{\mu}_R = 327.9$ MeV (see Table 5.2 for parameters for the latter choice). However, for the $O(N)$ model there is no renormalization scale for which $h_0 = 0$ if $M_\sigma \gtrsim 450$ MeV. Therefore, we set the σ mass to 400 MeV in the $O(4)$ model (see Table 5.1). At $\bar{\mu}_R = \mu_\chi = 424.07$ MeV all equations of motion are solved at zero temperature by the parameters given in Table 5.3.

LENAGHAN and RISCHKE (2000) have shown that in the case of explicit symmetry breaking in the HARTREE-FOCK approximation of the $O(4)$ linear sigma model,

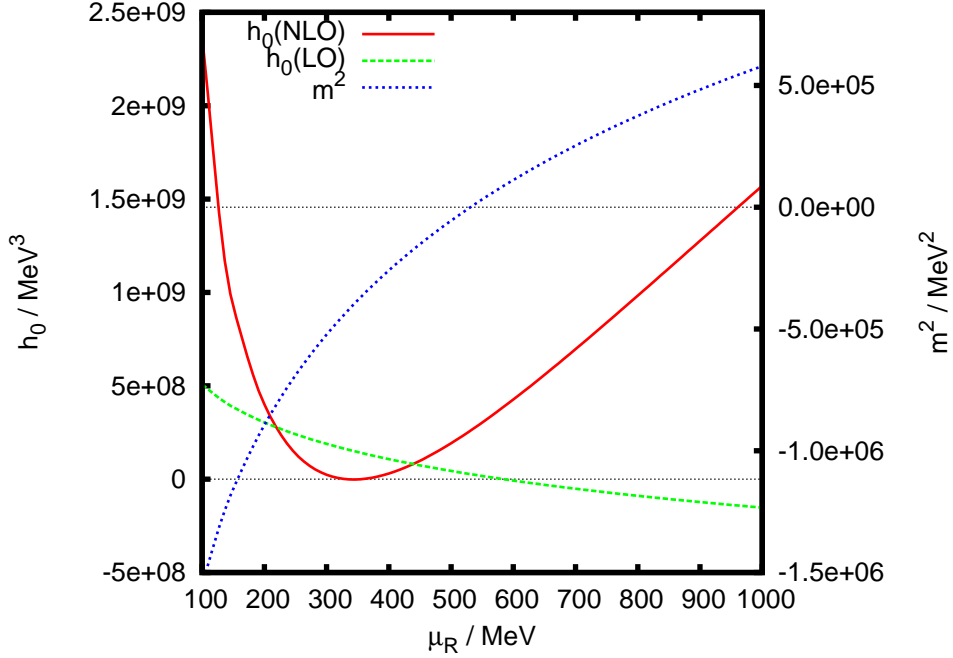


Figure 5.1: Renormalization scale dependence of the parameters h_0 and m^2 in the $U(2)_L \times U(2)_R$ linear sigma model with explicit symmetry breaking (cf. Table 5.1) at LO and at the two-loop level of NLO in a $1/N_f$ expansion.

parameter	explicit symmetry breaking		chiral limit	
	200 MeV	no renorm.	327.9 MeV	no renorm.
m^2	$-(943.37 \text{ MeV})^2$	$-(103.78 \text{ MeV})^2$	$-(729.85 \text{ MeV})^2$	$-(173.56 \text{ MeV})^2$
c	$(374.56 \text{ MeV})^2$	$(374.56 \text{ MeV})^2$	$(387.14 \text{ MeV})^2$	$(387.14 \text{ MeV})^2$
$N_f h_0$	$(733.32 \text{ MeV})^3$	$(121.60 \text{ MeV})^3$	0 MeV^3	0 MeV^3
$\frac{\lambda_1}{N_f^2}$	-19.30	-19.30	-19.13	-19.13
$\frac{\lambda_2}{N_f^2}$	78.49	78.49	82.70	82.70
$N_f \phi_0$	92.4 MeV	92.4 MeV	90 MeV	90 MeV

Table 5.2: Parameters in the $U(2)_L \times U(2)_R$ model for masses as in Table 5.1, $M_\sigma = 600 \text{ MeV}$ and $N_f = 2$.

parameter	explicit symmetry breaking		chiral limit	
$\bar{\mu}_R$	200 MeV	no renorm.	424.07 MeV	no renorm.
m^2	$-(220.54 \text{ MeV})^2$	$-(225.32 \text{ MeV})^2$	$-(262.34 \text{ MeV})^2$	$-(282.84 \text{ MeV})^2$
$\sqrt{N} h_0$	$(138.47 \text{ MeV})^3$	$(121.60 \text{ MeV})^3$	0	0
$\frac{\lambda}{N}$	8.23	8.23	9.88	9.88
$\sqrt{N} \phi_0$	92.4 MeV	92.4 MeV	90 MeV	90 MeV

Table 5.3: Parameters in the $O(4)$ model for masses as in Table 5.1, $M_\sigma = 400$ MeV and $N = 4$.

the temperature-dependence of the condensate and the masses is varying with the renormalization scale. So, this scale is nothing but an extra parameter which all quantities can (poly)logarithmically depend on. LENAGHAN and RISCHKE have also demonstrated that with an appropriate choice of $\bar{\mu}_R$ the results are almost identical to those obtained when neglecting finite renormalization terms entirely.

Furthermore, terms originating from renormalization can render the gap equations unsolvable above a certain temperature (BARDEEN and MOSHE, 1986; BAYM and GRINSTEIN, 1977; CHIKU and HATSUDA, 1998) because their right hand side is no monotonic function of the mass square.

5.2 $O(4)$ model

At a fixed temperature T and renormalization scale $\bar{\mu}_R$ we solve the condensate equation of motion (3.5). It contains the masses M_σ and M_π whose ϕ_0 -dependence is determined by the gap equations (3.4). So, for each iterative step in the solution of the condensate equation the mass gap equations (3.4) have to be solved in order to obtain the masses as functions of the condensate.

5.2.1 Chiral limit

In the chiral limit the explicitly symmetry-breaking parameter h_0 is zero and the pions are massless GOLDSTONE bosons. We choose $M_\sigma = 400$ MeV for reasons mentioned before in Section 5.1 and set all parameters to the appropriate values given in Table 5.3.

Figure 5.2(a) displays the condensate as a function of temperature. We can clearly observe a second-order phase transition: the function $\phi_0(T)$ reaches zero with infinite slope. The critical temperature is about 300 MeV for $\mu_R = \mu_\chi$. If we neglect all finite renormalization terms in the calculations (and set the respective parameters,

cf. Table 5.3) the critical temperature reduces to about 170 MeV which coincides with predictions from two-flavor lattice QCD (see *e.g.* AOKI *et al.*, 2006; KARSCH, 2002).

The temperature dependence of the masses is plotted in Fig. 5.2(b). For $\mu_R = \mu_\chi$, the σ mass slightly rises with increasing temperature before it drops down to about 250 MeV at the critical point. The pion mass grows from zero to 250 MeV at the critical temperature where it becomes identical to the σ mass. Without finite renormalization terms, the σ mass drops and the pion mass increases to approximately 30 MeV at the critical point where both masses become degenerate and then increase with rising temperature.

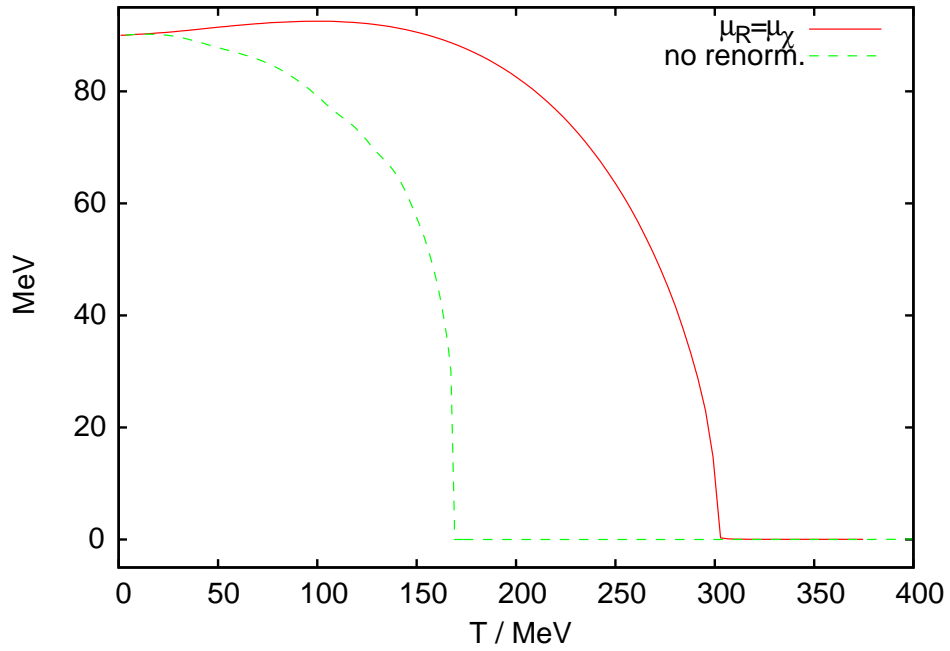
Looking at the temperature dependence of the masses [Fig.5.2(b)] one is tempted to say that GOLDSTONE's theorem is violated because in the broken phase ($\phi_0 \neq 0$) the pion has a finite mass at finite temperature. The reason for that is the fact that resummation schemes usually violate global symmetries (VAN HEES and KNOLL, 2002a). The so-called physical masses, obtained as second derivatives of a one-particle irreducible effective potential, are not identical to the variational mass parameters. The usual geometric argument that proves the physical GOLDSTONE masses to be zero is the following. Consider the second derivative of a 1PI effective potential depending on the $O(N)$ invariant $\vec{\phi}^2 = \phi_a \phi_a$

$$\left. \frac{\partial^2}{\partial \phi_a \partial \phi_b} V(\vec{\phi}^2) \right|_{\vec{\phi}=\langle \vec{\phi} \rangle} = 2 V'(\vec{\phi}^2) \delta_{ab} \Big|_{\vec{\phi}=\langle \vec{\phi} \rangle} + 4 V''(\vec{\phi}^2) \phi_a \phi_b \Big|_{\vec{\phi}=\langle \vec{\phi} \rangle}. \quad (5.6)$$

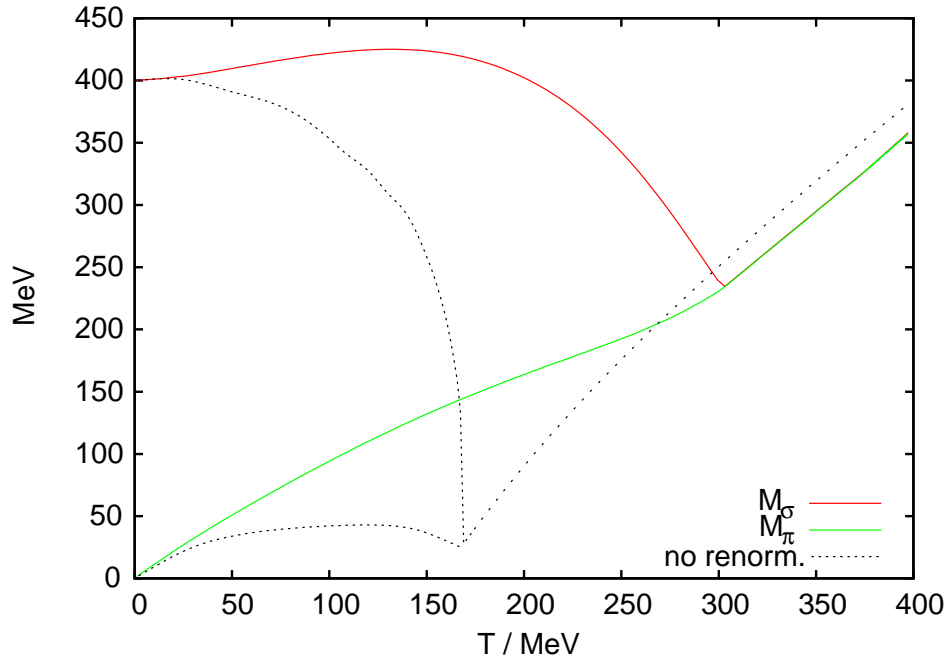
With the expectation value pointing only in the 0-direction, $\langle \vec{\phi} \rangle = (\phi_0, 0, \dots, 0)$, the GOLDSTONE masses are given by the derivatives perpendicular to that direction and thus are proportional to $V'(\vec{\phi}^2)$ which is zero for a non-trivial vacuum. So, whenever there is a minimum off zero in the potential there are GOLDSTONE bosons.

The reader is also referred to a publication (BAACKE and MICHALSKI, 2003a) in which the $O(N)$ model at finite temperature is studied in a fully self-consistent two-loop approximation. A second-order phase transition is found there as well and a similar result for the (variational) pion mass. However, it turns out that the physical σ mass, the second derivative of the effective potential, vanishes at the critical temperature.

To get another estimate for the critical temperature one can assume that due to a second-order phase transition all mass scales vanish: $M_\sigma = M_\pi = 0$. This is used in the condensate equation (3.5) with $h_0 = 0$. But we have to change this equation by resubstituting the gap equation (3.4) for M_π^2 because we do not assume the latter one



(a) Temperature dependence of the condensate.



(b) Temperature dependence of the masses. The dotted lines show the results for a calculation in which finite renormalization terms are neglected.

Figure 5.2: Chiral limit of the condensate and masses in the $O(4)$ model as functions of temperature. The renormalization scale is $\mu_R = \mu_\chi = 424.07$ MeV.

to be fulfilled for $M_\pi = 0$ at finite temperature. The condensate equation becomes

$$m^2 + \frac{N+2}{N} \lambda \Delta_\pi - 2 \frac{\lambda^2}{N} S_{\pi\pi\pi} = 0. \quad (5.7)$$

For zero mass, $M_\pi = 0$, the bubble and the sunset are

$$\Delta_0(T) = \frac{T^2}{12} \quad \text{and} \quad S_{000}(T) \simeq \frac{T^2}{13\frac{3}{8}}.$$

We determine m^2 as a function of the renormalization scale by solving the the gap equations (3.4) at zero temperature with the appropriate masses in the chiral limit (see Table 5.1). We neglect the sunsets for the moment and obtain the critical temperature as a function of the renormalization scale

$$T_c^2(\bar{\mu}_R) = -12 m^2(\bar{\mu}_R) \frac{N}{(N+2)\lambda} \Big|_{N=4} \quad (5.8)$$

as displayed in Figure 5.3 for two values of the σ mass. The tree-level values are $T_c \simeq 170$ MeV for $M_\sigma = 400$ MeV and $T_c \simeq 255$ MeV for $M_\sigma = 600$ MeV.

Including the sunsets for $M_\sigma = 600$ MeV the critical temperature is imaginary for $\bar{\mu}_R \lesssim 2.3$ GeV, at $\bar{\mu}_R \simeq 3.7$ GeV it is about 175 MeV. For a smaller σ mass of 400 MeV, it reduces to approximately 450 MeV for $\bar{\mu}_R \simeq \mu_\chi$. Only for a renormalization scale of 8 GeV the critical temperature lowers to 175 MeV. The corresponding tree-level results are 619 and 320 MeV, respectively.

5.2.2 Explicit symmetry breaking

In the case of explicit symmetry breaking there are three model parameters and three equations of motion [Eqs. (3.4) and (3.5)] so that the renormalization scale represents a degree of freedom in the solution. The results should depend on the choice of this scale. Figure 5.4(a) shows the temperature dependence of the condensate for different choices of $\bar{\mu}_R$. Qualitatively, the condensate behaves similar for any chosen renormalization scale: at low temperatures it stays well above 85 MeV, then it decreases almost linearly before it slowly approaches zero at a temperature beyond 400 MeV. Though, there is a quantitative difference depending on the value of the renormalization scale. The lower the renormalization scale (within the here chosen interval) the lower is the temperature at which the function $\phi_0(T)$ starts to drop. For $\bar{\mu}_R = 600$ MeV it is at about 200 MeV whereas for smaller renormalization scales this temperature decreases to about 100 MeV. Though for each choice

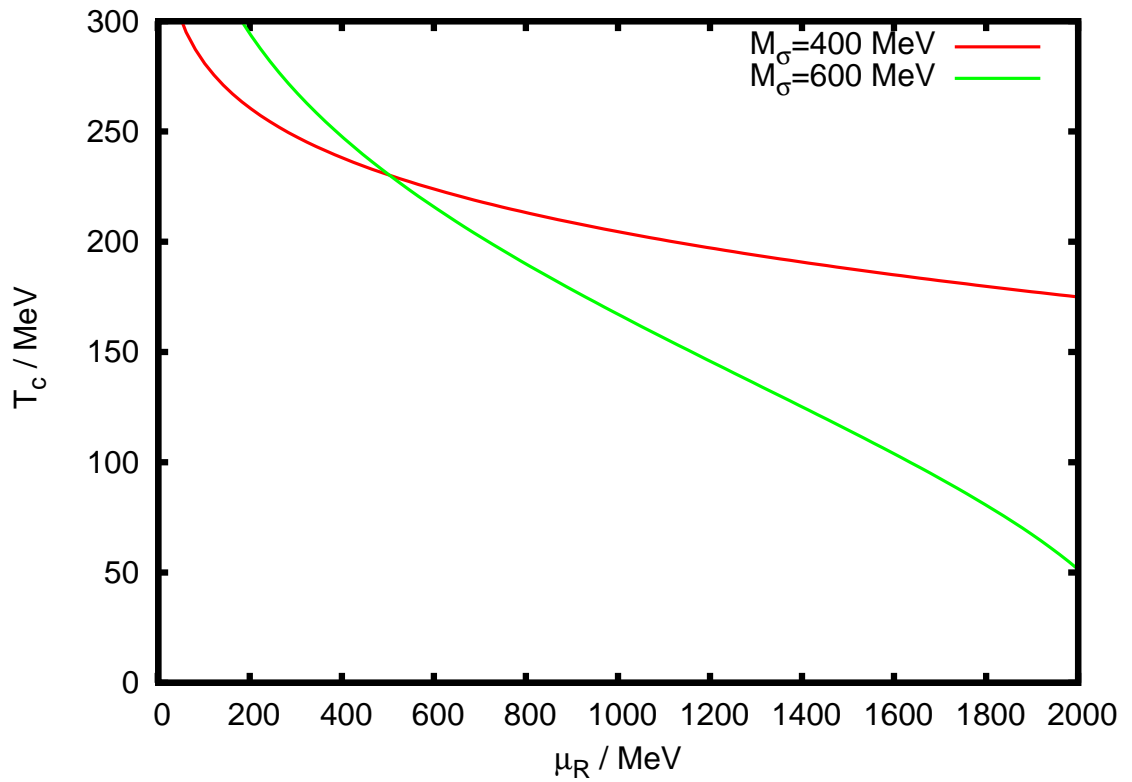


Figure 5.3: Estimated critical temperatures at leading order for $M_\sigma = 400$ and 600 MeV. At tree-level one obtains $T_c = 170$ and $T_c = 255$ MeV.

of the renormalization scale the system clearly exhibits a crossover transition; full symmetry is only reached at infinite temperature.

The *pseudocritical temperature* can be defined as the temperature where the susceptibility

$$\chi(T) = -\frac{\partial\phi_0(T)}{\partial T} \quad (5.9)$$

achieves its maximal value or, in other words, the temperature at which the function ϕ_0 exhibits an inflection point. Figure 5.4(a) clearly shows that the lower the renormalization scale the lower is the pseudocritical temperature, being at about 215 MeV for $\bar{\mu}_R = 100$ MeV. Without finite renormalization terms the temperature is even lower (about 195 MeV) than for any choice of $\bar{\mu}_R$. Thus, finite renormalization terms increase the transition temperature. They also influence the temperature dependence of the masses [Fig. 5.4(b)]; for $\bar{\mu}_R = 100$ MeV both the σ and the pion masses behave very similar to the case without renormalization at temperatures below 300 MeV. For a choice that would be sufficient in the chiral limit ($\mu_R = \mu_\chi$) both masses change more gradually with rising temperature. Though, the qualitative behavior of a decreasing σ and an increasing pion mass persists.

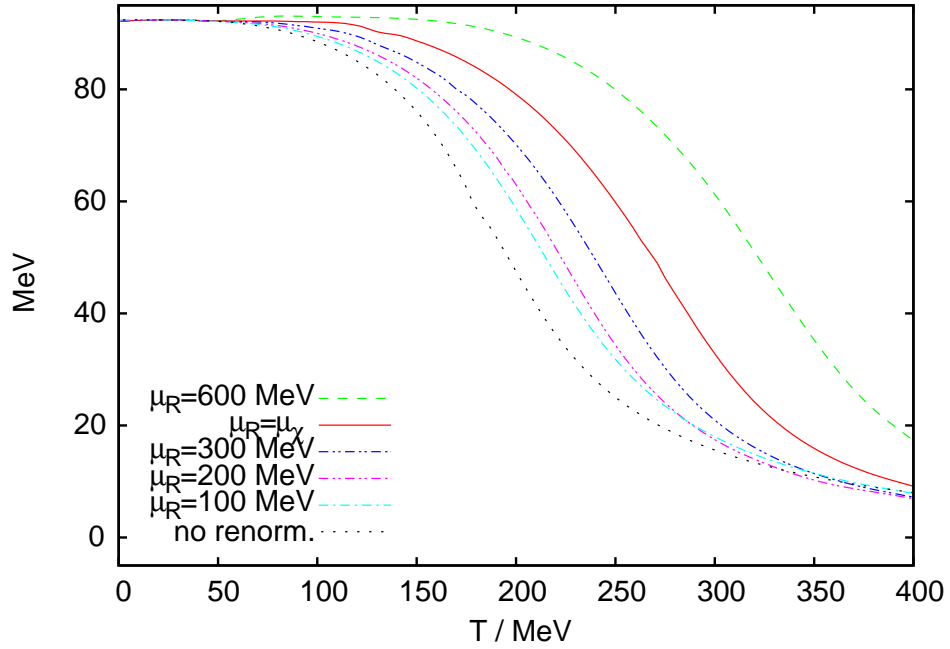
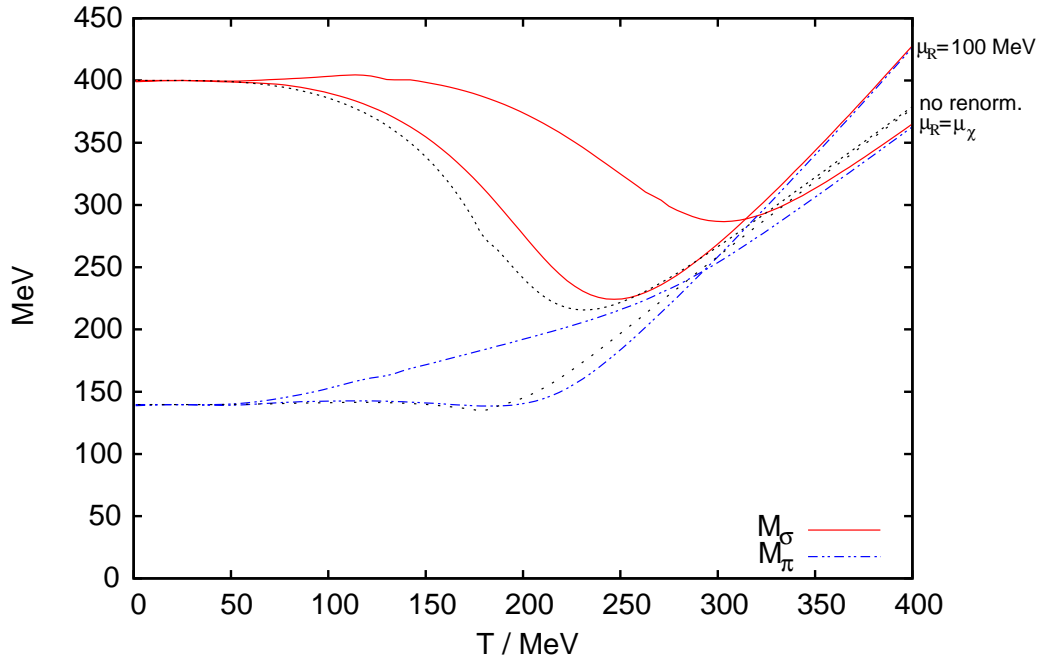
5.3 $U(2)_L \times U(2)_R$ model

The numerical procedure for the $U(2)_L \times U(2)_R$ linear sigma model is the same as for the $O(N)$ model described in Section 5.2. Though, it turns out that only inside a very narrow band in the vicinity of $\bar{\mu}_R \approx 200$ MeV one can find solutions to the equations of motion in a temperature range from zero to 300-400 MeV; outside this band the procedure of numerical solution is plagued by severe instabilities, *e.g.* there is no solution to the gap equation for which each of the four mass squares is positive, or the right hand side of the condensate equation has no zero for positive values of ϕ_0 .

In the following we will discuss results obtained for a fixed anomaly parameter as in Table 5.2 and for a temperature-dependent anomaly. Results for the chiral limit will only be discussed for neglected renormalization terms.

5.3.1 Explicit symmetry breaking with a fixed axial anomaly

Figure 5.5(a) displays the temperature dependence of the condensate in the $U(2)_L \times U(2)_R$ model with an axial anomaly for a renormalization scale between 180 and


 (a) The condensate ϕ_0 as a function of temperature.


(b) Temperature dependence of the masses. The dotted lines show the results for a calculation where finite renormalization terms are neglected.

 Figure 5.4: Condensate and masses in $O(4)$ model with explicit symmetry breaking for different choices of the renormalization scale ($\mu_\chi = 424.07$ MeV.)

220 MeV. From zero temperature up to a value of $T \simeq 200$ MeV the order parameter stays above 80 MeV before it drops with decreasing slope to about 20 MeV at $T \simeq 400$ MeV. The pseudocritical temperature is about 290 MeV for $\bar{\mu}_R = 200$ MeV. It increases by some MeV when lowering the renormalization scale and *vice versa*; within the region $190 \text{ MeV} < \bar{\mu}_R < 220 \text{ MeV}$, the higher the renormalization scale the faster the order parameter tends to zero at larger temperatures (above 300 MeV). Without renormalization terms one finds a qualitatively similar temperature behavior of the condensate, though already between 175 and 200 MeV it decreases from 75 down to 20 MeV with a pseudocritical temperature at about 190 MeV. The small “bump” in the condensate stems from the crossing of mass thresholds in the sunset terms [see Fig. 4.4(a) and discussion in Section 4.4].

At comparable renormalization scales the condensate in the $U(2)_L \times U(2)_R$ linear sigma model decreases with a smaller slope than the one in the $O(N)$ model [Figs. 5.4(a) and 5.5(a)]. However, when neglecting renormalization terms, it is the other way round; in this case, the phenomenon can be explained by comparing the terms in curly brackets in the condensate equations (2.19) and (3.5). At the same temperature the relevant term in the condensate equation of the $U(2)_L \times U(2)_R$ model is obviously larger than that in the $O(N)$ model; although the (negative) value of $(m^2 - c)$ in the $U(2)_L \times U(2)_R$ model is about three times as large as the value of m^2 in the $O(4)$ model (Tables 5.2 and 5.3), the pure number of terms in the condensate equation of the $U(2)_L \times U(2)_R$ model and also their numerical size (compare the coupling constants of both models, Tables 5.2 and 5.3) exceed those in the $O(4)$ model.¹ To match with h_0 on the left hand side of the equation (which has comparable values in both models) one needs lower values for the condensate if the value of the term in curly brackets is larger. Therefore, the condensate drops faster in the $U(2)_L \times U(2)_R$ model when neglecting renormalization terms. With renormalization terms the argumentation is not that straightforward because both bubble and sunset graphs are not monotonic (not even positive) functions of temperature and masses which can lead to opposite results.

The temperature-dependent masses in the $U(2)_L \times U(2)_R$ model for $\bar{\mu}_R = 210$ MeV are displayed in Fig. 5.5(b). All four masses rise more or less strongly until, at temperatures above 350 MeV, the masses of the chiral partners are (almost) identical, *i.e.*, chiral symmetry is (almost) restored. The $U(1)_A$ symmetry remains broken since the parameter c is not a function of temperature. The gap between the mass squares of the isospin partners η and π (or σ and a_0) remains equal to $2c$ according to Eqs. (2.18). Without renormalization terms the masses behave differently with

¹A σ mass of 600 MeV would imply a coupling of $\lambda \simeq 20$ in the $O(4)$ model. So, this argument holds even if the M_σ is the same in both models.

rising temperature. M_σ and M_{a_0} drop by almost 400 MeV before they meet with their chiral partners at about 275 MeV. One striking aspect is the fact that the masses decrease with rising temperature for $T \gtrsim 300$ MeV and $\bar{\mu}_R = 210$ MeV. The reason for that can be found in the gap equations (2.18). At a fixed temperature the masses correlate with the value of the condensate; the higher the condensate the higher are the values for the masses. With rising temperature the condensate is decreasing which makes the masses drop, but simultaneously thermal corrections for each mass increase. These changes have to be compensated by a suitable change of M^2 in the gap equations. Since the right hand side of each of these equations is not a monotonic function of the mass square (*e.g.* there is a logarithm), a lowering value of M^2 being a solution of the gap equation can be caused by rising temperature depending on the values of the other terms in this equation.

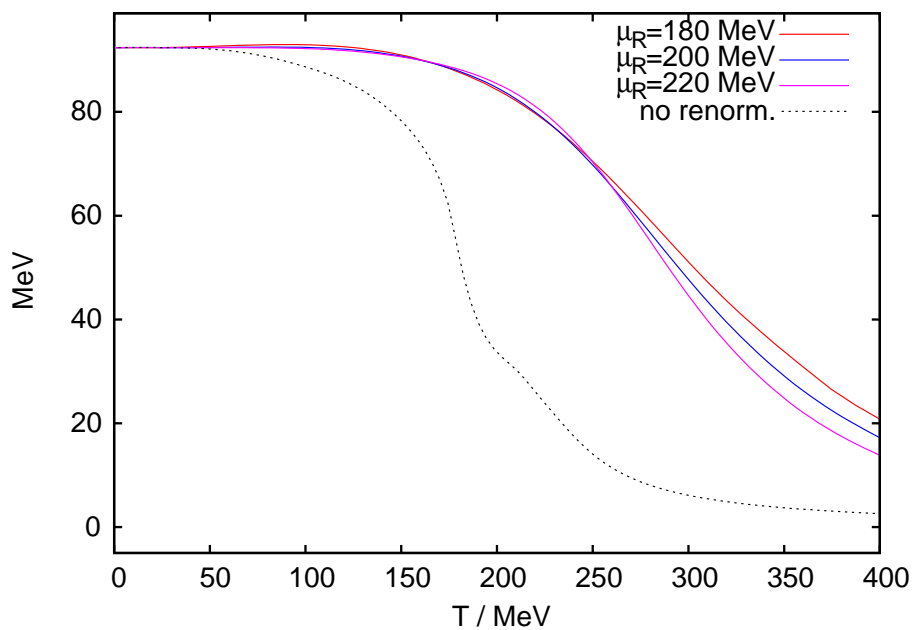
5.3.2 Temperature-dependent $U(1)_A$ anomaly

There are indications from QCD lattice calculations that at high temperatures, effects arising from the $U(1)_A$ breaking are strongly suppressed (ALLÉS *et al.*, 1997, 1999; BERNARD *et al.*, 1997; CHANDRASEKHARAN *et al.*, 1999; CHEN *et al.*, 1998; CHU and SCHRAMM, 1995; CHU *et al.*, 2000; GOTTLIEB *et al.*, 1997; KOGUT *et al.*, 1998). This suggests an effective restoration of the $U(1)_A$ symmetry close to the critical temperature. We model this by fixing the parameters at zero temperature to the physical masses but considering the anomaly parameter c as a function of temperature. As an example we describe a suddenly dropping strength of the axial anomaly at 200 MeV using the FERMI function

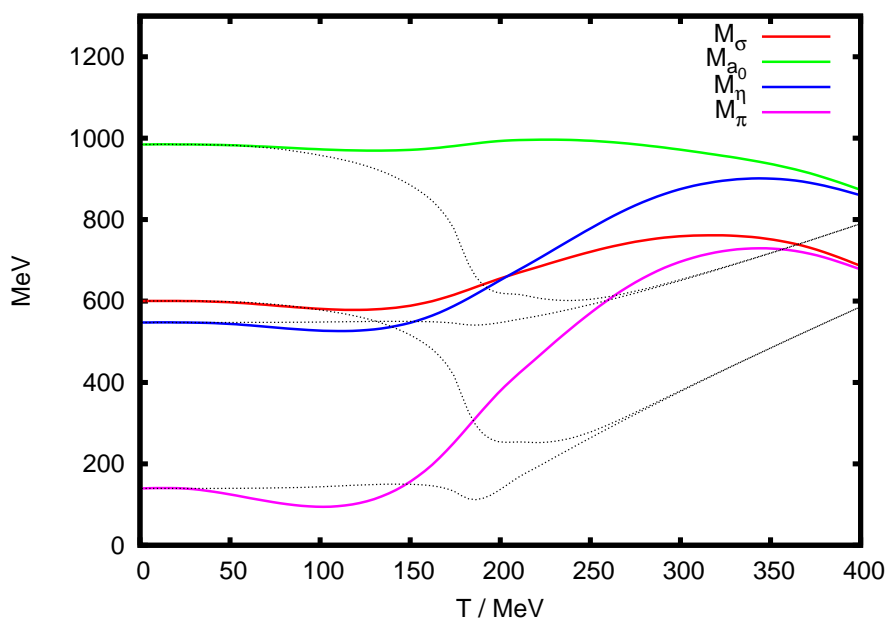
$$c(T) = \frac{c_0}{1 + \exp[(T - T_A)/\Delta T]} \quad (5.10)$$

with $T_A = 200$ MeV and $\Delta T = 10$ MeV, see Fig. 5.6. The values are chosen such that at $T \approx 225$ MeV the strength of the anomaly has dropped by one order of magnitude.

The function $\phi_0(T)$ is shown in Fig. 5.7(a). From zero temperature to about 200 MeV the condensate even slightly increases, *i.e.* chiral symmetry breaking is enhanced. Above this temperature the condensate decreases to about 20 MeV at $T \simeq 400$ MeV with a larger slope than for a fixed axial anomaly. Also for a varying anomaly the system exhibits a crossover but with a larger pseudocritical temperature (about 320 MeV) than for a constant anomaly strength. Obviously, the restoration of the axial anomaly, *i.e.* the parameter c approaching zero, makes the condensate increase at a fixed temperature. We find an exactly opposite situation when we neglect finite renormalization terms. Comparing the condensate as a function of temperature for



(a) Temperature-dependent condensate for different choices of the renormalization scale $\bar{\mu}_R$.



(b) Masses as a function of temperature at $\bar{\mu}_R = 210$ MeV. Dotted lines show the results obtained without renormalization terms.

Figure 5.5: Condensate and masses at two-loop NLO-1/ N_f in the $U(2)_L \times U(2)_R$ model with a fixed axial anomaly.

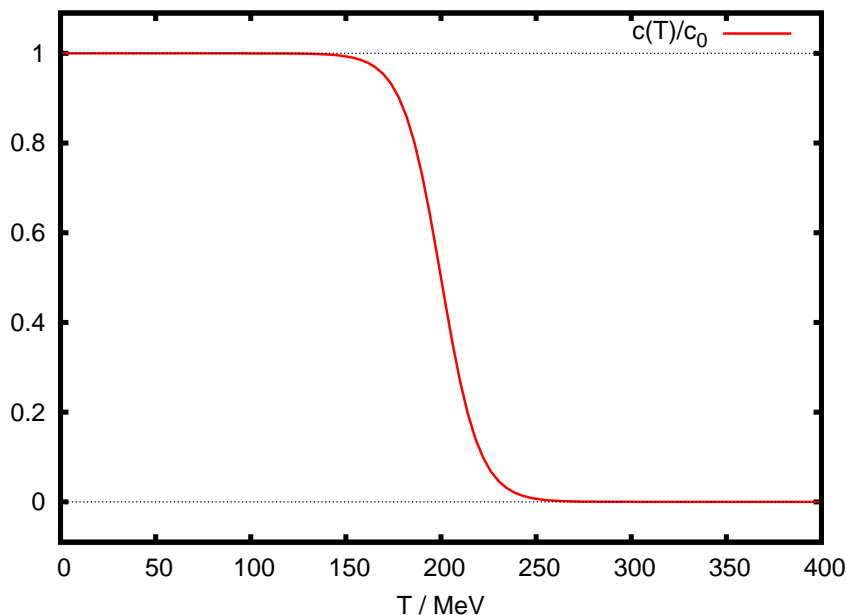


Figure 5.6: Modelled temperature dependence of the anomaly parameter c . The behavior is like the function in Eq. (5.10) with $T_A = 200$ MeV and $\Delta T = 10$ MeV.

a fixed and a varying anomaly we observe that the pseudocritical temperatures are approximately equal but a decreasing anomaly strength drives the condensate faster to zero. A possible explanation for that is the following: at fixed ϕ_0 , a dropping anomaly increases the right hand side of the condensate equation (2.19) — the term $(m^2 - c)$ grows with smaller values of c — so that a smaller value of the condensate is needed to match with the left hand side. Including finite renormalization terms this argument is spoiled by the behavior of the mass squares entering the bubble and sunset graphs in the condensate equation (2.18).

For $\bar{\mu}_R = 200$ MeV, the pion mass [Fig. 5.7(b)] grows from 140 MeV to about 550 MeV at $T \simeq 250$ MeV where it becomes identical to the mass of its isospin partner η as it is expected because the anomaly strength is almost zero at this temperature. The σ mass grows from 600 MeV above 800 MeV (at $T \gtrsim 300$ MeV) before it matches with the a_0 and the other two masses at about $T = 375$ MeV. All four masses tend to decrease with rising temperature beyond 350 MeV like for a fixed anomaly.

Neglecting finite renormalization terms the masses, again, behave differently with rising temperature. But there is not much deviation from the results for a fixed anomaly in the same approximation. Chiral symmetry is (almost) restored at tem-

peratures of about at about 210 MeV where the masses of the chiral partners degenerate. The restoration of the $U(1)_A$ symmetry is complete as soon as all four masses are identical which happens for temperatures above 240 MeV. Thus, the $U(1)_A$ is restored at higher temperatures than chiral symmetry as expected from the choice of parameters for Eq. (5.10). Without renormalization terms, the temperature behavior of the condensate and the masses is quite similar to that found in the framework of a NAMBU–JONA-LASINIO (NJL) model with three quark flavors (COSTA *et al.*, 2004, 2005).

In the HARTREE-FOCK approximation of a linear sigma model with three quark flavors (without renormalization terms), SCHAFFNER-BIELICH (2000) observed that a suddenly dropping anomaly parameter triggers the restoration of chiral symmetry, *i.e.*, the masses of the chiral partners degenerate at lower temperatures than for a fixed anomaly. In a two-loop approximation (without $1/N_f$ combinatorics) one finds the same effect in the $U(2)_L \times U(2)_R$ linear sigma model (MICHALSKI, 2006). It is caused by combinatorial factors in the mass gap equations [cf. Eqs. (2.18)] which differ from those used in our two-loop- $1/N_f$ approximation. In those approximations, the masses of the pseudo-GOLDSTONE bosons η and π even differ from one another if the anomaly parameter c is zero. They only become identical when chiral symmetry is restored, hence a violation of the $U(1)_A$ symmetry beyond tree-level is a property of those approximations (MICHALSKI, 2006; RÖDER *et al.*, 2003) but not of the one we chose here.

5.3.3 Chiral limit

In the chiral limit of the $U(2)_L \times U(2)_R$ model, a renormalization scale $\bar{\mu}_R = 327.9$ MeV is needed to obtain $h_0 = 0$ (cf. Table 5.2). With such a high scale compared to the choices for explicit symmetry breaking, it turns out that the gap equations (2.18) or even the condensate equation (2.19) do not have a solution as soon as the temperature exceeds about 100–140 MeV. There is always the trivial solution $\phi_0 = 0$ for the condensate but a non-trivial solution could not be found in the intermediate temperature region between about 100 and 300 MeV. So, the quest for a phase transition cannot be successful.

However, if finite renormalization terms are neglected there is a solution of the equations of motion. The results in this approximation are shown in Fig. 5.8. We plot both the results for a fixed axial anomaly and for a temperature-dependent one [cf. Eq. (5.10)]. In both cases, the condensate monotonically decreases from 90 MeV at zero temperature to zero at the critical temperature. At about $T = 190$ MeV its temperature behavior is affected by the decreasing anomaly and drops down faster

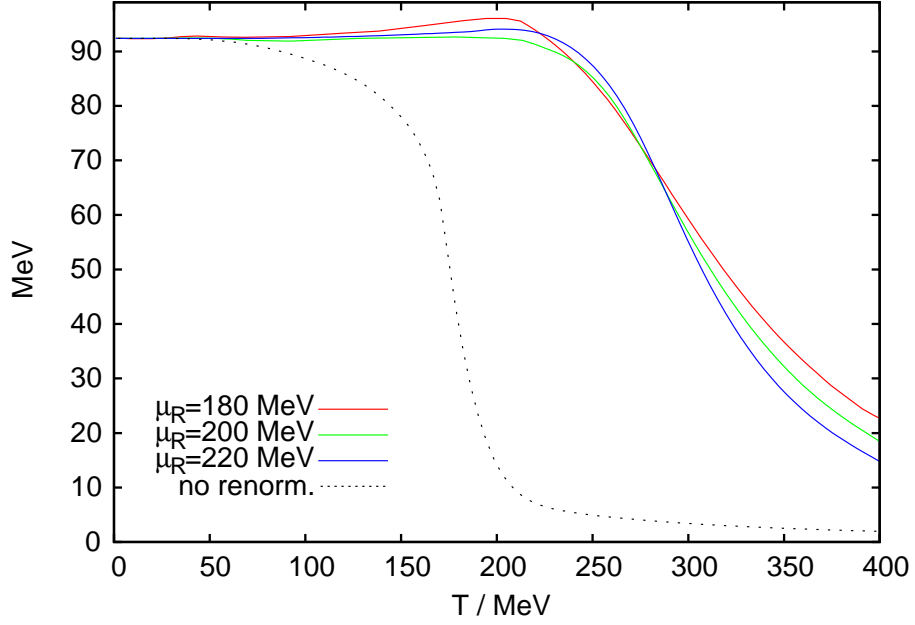
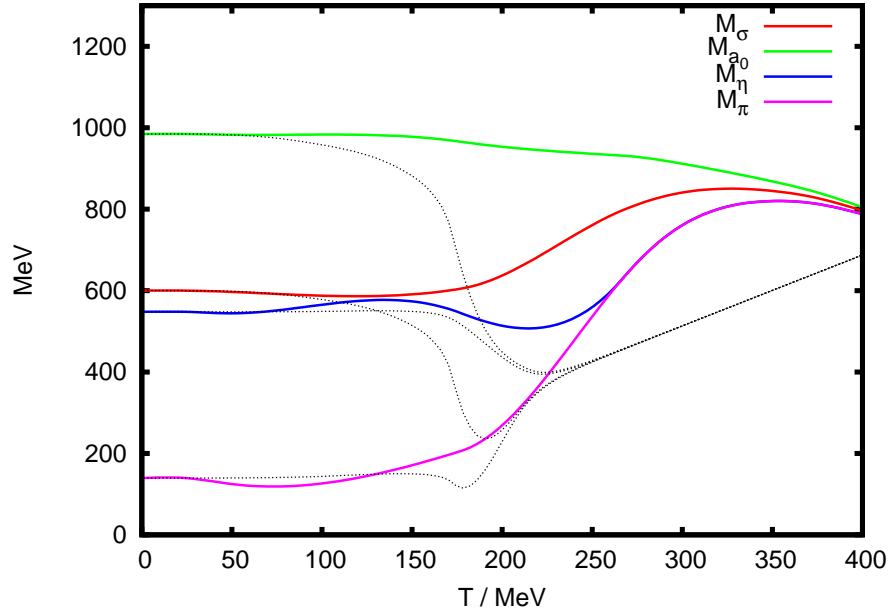
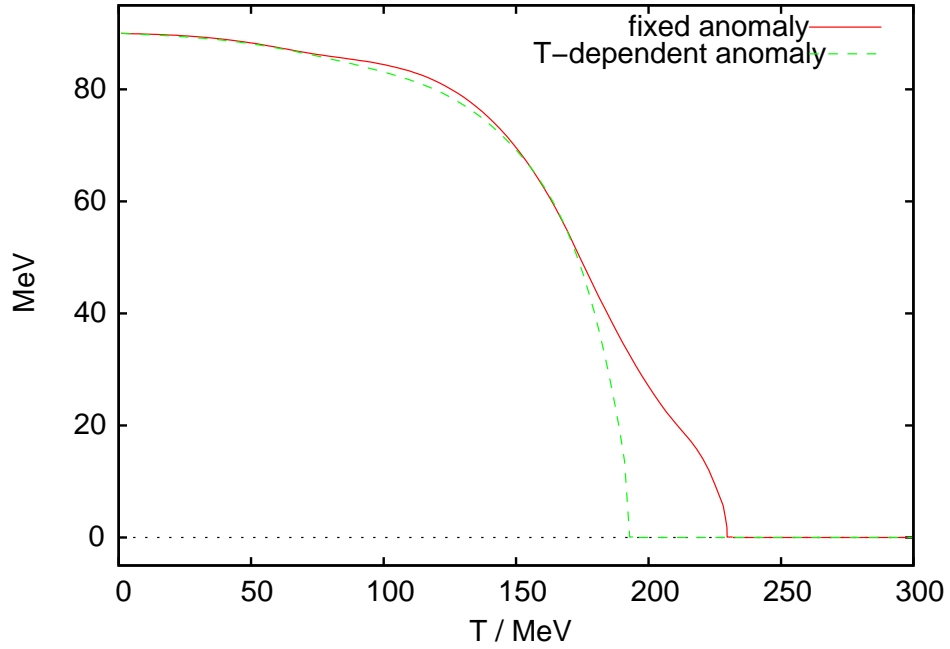

 (a) Condensate for different values of the renormalization scale $\bar{\mu}_R$.

 (b) Temperature-dependent masses for $\bar{\mu}_R = 200$ MeV. The dotted lines show the result when neglecting renormalization terms.

 Figure 5.7: Results for the two-loop NLO-1/ N_f approximation of the $U(2)_L \times U(2)_R$ model with a temperature-dependent axial anomaly [cf. Eq. (5.10)]

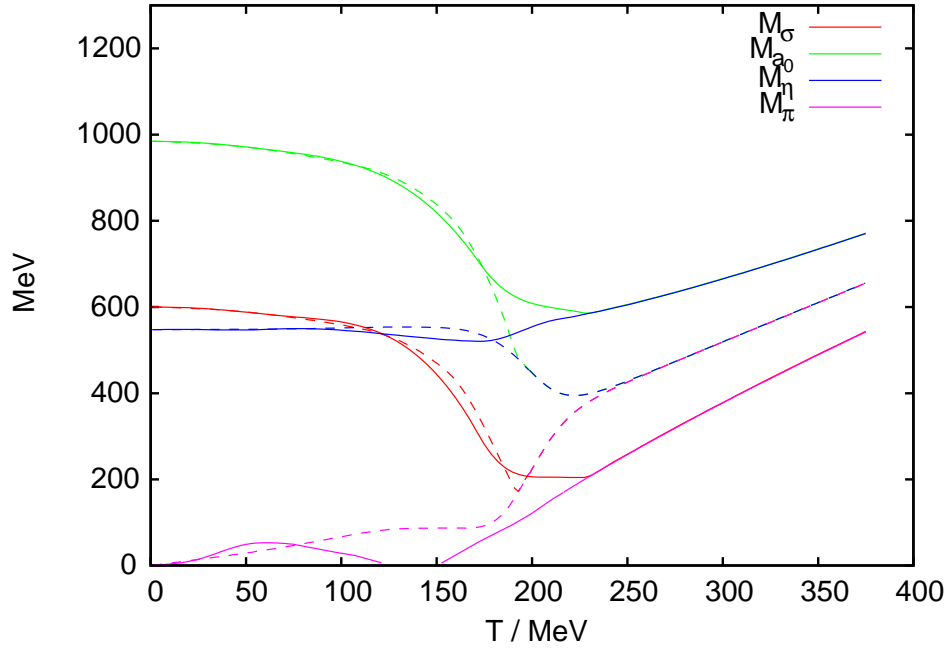
than for a fixed anomaly parameter. The critical temperatures are 193 MeV and 229 MeV, respectively. The condensate approaches zero with infinite slope which indicates a second-order phase transition. The anomaly is still present (about 50%) at a temperature of 200 MeV so the system still belongs to the universality class of the $O(4)$ HEISENBERG magnet and should have a phase transition of second order. Reducing the temperature T_A at which the $U(1)_A$ is restored [cf. Eq. (5.10)] significantly below the critical temperature (for the chiral transition) finally makes the transition first-order as expected.

The masses of the chiral partners degenerate at the critical temperature and for a vanishing anomaly (at $T \simeq 230$ MeV) all four masses become identical, too. Beyond the critical temperature all masses grow (almost) linearly with temperature. For a fixed axial anomaly, the square of the pion mass drops below zero for $120 \text{ MeV} \lesssim T \lesssim 150 \text{ MeV}$. In that region, the zero-temperature part of the bubble [cf. Eq. (4.1)] is computed by taking the real part of the logarithm but a negative prefactor. The thermal part can only be calculated for the absolute value, otherwise the integral would not converge for imaginary values of the energy.

Here as well, the pion mass is finite in a region where the condensate is non-vanishing. The geometrical argument given in Section 5.2.1 which “saves” GOLDSTONE’s theorem is applicable to the $U(2)_L \times U(2)_R$ model as well: the variational masses are not the “physical” ones due to symmetry breaking through resummation (VAN HEES and KNOLL, 2002a).



(a) Condensate as a function of temperature.



(b) Temperature-dependent masses for a fixed axial anomaly (solid lines) and a varying one (dashed lines).

 Figure 5.8: Results in the chiral limit of the $U(2)_L \times U(2)_R$ model in the two-loop NLO- $1/N_f$ approximation for a fixed and a temperature-dependent anomaly [Eq. (5.10)]. Finite renormalization terms are neglected.

Chapter 6

Conclusions and outlook

In the first part of this thesis we have investigated the restoration of chiral symmetry in the $U(2)_L \times U(2)_R$ linear sigma model and in the $O(N)$ linear sigma model at finite temperature. For a fixed axial $U(1)$ anomaly the masses of the chiral partners become identical at a temperature of about 400 MeV where a mass gap of $2c$ between the isospin partners remains. For renormalization scales in the vicinity of 200 MeV the effect of finite renormalization terms is significant; neglecting those terms makes the condensate drop faster with rising temperature. The pseudo-critical temperature is about 190 MeV without those terms but beyond 250 MeV if they are considered.

We have also investigated the effect of a temperature-dependent anomaly parameter $c(T)$ as in Eq. (5.10). A steep decrease at about 200 MeV, such that the strength is reduced to 10% at temperatures of about 230 MeV, even causes the condensate to rise by some MeV before it decreases. As expected from the function $c(T)$, the $U(1)_A$ symmetry can be restored, *i.e.* $M_\pi \simeq M_\eta$, when chiral symmetry is still broken because the mass gap equations (2.18) are totally $U(2)_L \times U(2)_R$ -symmetric. This result is different to that obtained in a 2PPI two-loop approximation (MICHALSKI, 2006) or in HARTREE-FOCK (SCHAFFNER-BIELICH, 2000) where the mass gap equations violate the $U(1)_A$ symmetry through radiative corrections.

In the chiral limit the $O(N)$ model exhibits a second-order phase transition at a critical temperature of about 300 MeV for $\bar{\mu}_R = 424.07$ MeV. Omitting finite renormalization terms reduces the critical temperature to 170 MeV which is comparable with results from QCD lattice calculations (AOKI *et al.*, 2006; KARSCH, 2002). In the chiral limit of $U(2)_L \times U(2)_R$ model without renormalization terms a second-order phase transition was found as well. The critical temperatures for a fixed anomaly parameter c is at about 230 MeV which is higher than in the $O(4)$ model in the same approximation. A decreasing anomaly (50% at 200 MeV, 10% at 225 MeV)

could significantly reduce this critical temperature down to 190 MeV.

Estimates of the critical temperature in the $O(4)$ linear sigma model based on universality class arguments yield values between 250 and 300 MeV at leading order. Including the sunset graphs from NLO this estimate of the critical temperature becomes less reliable due to the high values of the coupling constant. The critical temperature increases by 150 MeV for $M_\sigma = 400$ MeV whereas it becomes imaginary for $M_\sigma = 600$ MeV.

There is a significant difference between the results with and without finite renormalization terms. In the $O(4)$ model with explicit symmetry breaking and for $\bar{\mu}_R \simeq 100$ MeV, renormalization terms only slightly change the results but for the $U(2)_L \times U(2)_R$ model their influence is not negligible. In the present approximation these terms drive the results out of the region proposed by QCD lattice calculations. One may question whether to include finite renormalization terms at all because linear sigma models only serve as effective theories of QCD. Especially, the compositeness of mesons — a feature not accessible in linear sigma models — may influence the phase transition in QCD. Therefore, the agreement with QCD predictions (that appears in the unrenormalized case) is rather surprising than expected. Nevertheless, linear sigma models are relativistic quantum field theories in which renormalization terms naturally arise.

The fact that in the chiral limit the pion mass is finite below the critical temperature indicates symmetry breaking within the resummation formalism rather than a violation of GOLDSTONE's theorem. From symmetry arguments one can conclude that the “physical” GOLDSTONE bosons are massless as long as there is spontaneous symmetry breaking through a nontrivial minimum of the effective potential.

Without renormalization terms we have obtained similar results as in a pure two-loop approximation (MICHALSKI, 2006) and in HARTREE-FOCK (RÖDER *et al.*, 2003) whereas our approximation does *not* contain a $U(1)_A$ violation beyond tree-level which results in different values for the η and pion masses even without an axial anomaly.

Comparing this work with recent publications (RÖDER, 2005; RÖDER *et al.*, 2005) one can state that the effect of non-local corrections to the propagators seems to be more successful in reproducing the critical temperature to a desired value of about 175 MeV (KARSCH, 2002; LAERMANN and PHILIPSEN, 2003) than considering only local corrections (even without renormalization). The approximation described in this thesis yields (pseudo-)critical temperatures far above the lattice data unless renormalization terms are neglected.

Including strange mesons ($N_f = 3$) can possibly lead to interesting non-linear effects since the $U(1)_A$ anomaly term is trilinear for three flavors and thus generates addi-

tional sunset graphs with different signs. Adding fermions (nucleons or constituent quarks) to the model using a YUKAWA coupling is also an attractive extension of this work. For the $O(N)$ model this has been done by several authors before (CALDAS *et al.*, 2001; MÓCSY *et al.*, 2004; ROH and MATSUI, 1998).

Part II

Testing and Comparing Resummation Schemes

Chapter 7

Introduction

In the second part of this thesis the $O(N)$ linear sigma model as introduced in Chapter 3 is used as a test bench for different resummation schemes. For that purpose we restrict ourselves to two spacetime dimensions and investigate whether different resummation schemes, at NLO of a $1/N$ expansion, yield an effective potential with spontaneous symmetry breaking. According to COLEMAN (1973), there are no GOLDSTONE bosons in two dimensions because the propagator of a massless boson in two dimensions is ill-defined,

$$\langle \Phi(0) \Phi(x) \rangle = \int \frac{d^2k}{(2\pi)^2} e^{ik \cdot x} \delta(k^2) \theta(k^0) = \int \frac{dk_1}{2\pi |k_1|} \cos(k_1 x_1) e^{-i|k_1|x_0}, \quad (7.1)$$

it diverges at the origin. Therefore spontaneous symmetry breaking does not occur in two dimensions.

Early investigations of the $O(N)$ model beyond the classical level have been based on including one-loop quantum and thermal corrections. These studies have been centered around the discussion of the one-loop effective potential $V_{\text{eff}}(\phi)$ where ϕ is the mean value of the quantum field Φ , in a sense being defined more precisely by the effective action formalism, summing up *one-particle irreducible* (1PI) graphs (JACKIW, 1974). Resummation formalisms — usually obtained from the 1PI formalism by introducing an auxiliary field — made it possible to include a full class of FEYNMAN graphs, so that the effective potential could be computed to leading (COLEMAN *et al.*, 1974; DOLAN and JACKIW, 1974b; SCHNITZER, 1974) and next-to-leading order (NLO) of a $1/N$ expansion (ROOT, 1974).

And indeed, at leading order in a $1/N$ expansion one does not find spontaneous symmetry breaking in $1 + 1$ dimensions (COLEMAN *et al.*, 1974), while in $3 + 1$

dimensions the effective potential is flat for $|\vec{\phi}| < v$ (BARDEEN and MOSHE, 1983).¹ An approximation including some nonleading terms of a $1/N$ expansion is the so-called HARTREE-FOCK approximation. It is usually motivated by a self-consistency of one-loop quantum corrections. It has been studied in $3 + 1$ dimensions by various authors in thermal equilibrium (AMELINO-CAMELIA, 1997; AMELINO-CAMELIA and PI, 1993; LENAGHAN and RISCHKE, 2000; NEMOTO *et al.*, 2000; VERSCHELDE and DE PESSEMIER, 2002). Even in $1 + 1$ dimensions the HARTREE-FOCK approximation exhibits spontaneous symmetry breaking and symmetry restoration as in $3 + 1$ dimensions, an obviously unphysical feature and a shortcoming of the HARTREE-FOCK approximation.

If one wants to go beyond the large- N and HARTREE-FOCK approximations there is a variety of choices. One of those is the formalism of the *two-particle irreducible* (2PI) effective action by CORNWALL *et al.* (1974) within which one may include higher loop corrections, higher orders in $1/N$ *etc.* This formalism requires the solution of DYSON-SCHWINGER equations for the propagators in order to sum up certain classes of FEYNMAN graphs. Apart from the fact that this may be technically demanding, there still is the obstacle that in $3 + 1$ dimensions renormalization has to be carried out for the whole of the resummed graphs which is a challenging task (BERGES *et al.*, 2005; BLAIZOT *et al.*, 2004; VAN HEES and KNOLL, 2002a,b,c); as this obstructs the discussion of spontaneous symmetry breaking, which here is our main interest, we discuss the model in $1 + 1$ dimensions, where the problem of renormalization does not arise and explicit numerical computations can be performed.

A technically less demanding approach is the so-called *two-particle point-irreducible* (2PPI) resummation introduced by VERSCHELDE and COPPENS (1992, 1993). This approach is identical to the HARTREE-FOCK approximation if only one-loop 2PPI graphs are included. For this formalism renormalization has been fully discussed by VERSCHELDE (2001); symmetry restoration at finite temperature has been investigated in $3 + 1$ dimensions in a two-loop approximation including the sunset diagram, for the case $N = 1$ (SMET *et al.*, 2002) and for the $O(N)$ model with arbitrary N (BAACKE and MICHALSKI, 2003a).

The 2PI formalism has the advantage that at a given order of the loop expansion it resums a larger class of FEYNMAN diagrams than the 2PPI or 1PI auxiliary field scheme (ROOT, 1974). From a variational point of view it allows for a more “flexible” propagator whose self-energy insertions are nonlocal in spacetime and thereby become momentum dependent.

In two spacetime dimensions, we will evaluate the effective potential at finite temperature at next-to-leading order (NLO) of a $1/N$ expansion in all three resummation

¹The latter follows from an end point extremum of the effective action $\Gamma(\phi, M^2)$ at $M^2 = 0$.

schemes by solving the **DYSON-SCHWINGER** equations in order to check whether a scheme correctly reproduces the non-existence of spontaneous symmetry breaking. For comparison we will also show results obtained at leading order (LO) of the $1/N$ expansion and in the **HARTREE-FOCK** approximation. A summary of this part of the thesis has been published (BAACKE and MICHALSKI, 2003a,b).

Chapter 8

Effective action in different resummation schemes

As an example for the application of resummation schemes we take the $O(N)$ linear sigma model as introduced in Chapter 3. Here, we consider the model in two spacetime dimensions, so the classical action is given by

$$\mathcal{S}[\vec{\Phi}] = \int d^2x \mathcal{L}[\vec{\Phi}] = \int d^2x \left\{ \frac{1}{2} \partial_\mu \vec{\Phi} \cdot \partial^\mu \vec{\Phi} - \frac{\lambda}{4N} \left(\vec{\Phi}^2 - Nv^2 \right)^2 \right\}, \quad (8.1)$$

where $\vec{\Phi} = (\Phi_1, \Phi_2, \dots, \Phi_N)$ is an $O(N)$ multiplet of real scalar fields.

In this chapter we compute the *two-particle irreducible* (2PI) and the *two-particle point-irreducible* (2PPI) effective action as well as a *one-particle irreducible* (1PI) effective action with *auxiliary fields*.

8.1 2PI effective action at NLO

The 2PI effective action formalism (CORNWALL *et al.*, 1974) introduces two variational functions: an external field $\phi(x)$ and a GREEN function $G(x, x')$, which arise as LEGENDRE conjugate variables related to a local source term $J(x) \Phi(x)$ and a bilocal source term $K(x, x') \Phi(x) \Phi(x')$. Assuming that the expectation value of $\vec{\Phi}^2$ will scale as N we introduce the external field ϕ with a scale factor \sqrt{N} and rotate it so that it points in the 1-direction, *i.e.*,

$$\langle \Phi_i \rangle = \sqrt{N} \phi \delta_{i1}.$$

We then obtain the classical potential

$$V_{\text{class}}(\phi) = \frac{\lambda}{4N} (N\phi^2 - Nv^2)^2 = N\frac{\lambda}{4} (\phi^2 - v^2)^2 . \quad (8.2)$$

The one-loop part of the effective action is given by

$$\Gamma_1[\phi, \mathbf{G}] = \frac{i}{2} \text{Tr} \ln \mathbf{G}^{-1} \mathbf{G}_0 + \frac{1}{2} \text{Tr} [i\mathcal{D}^{-1} \mathbf{G} - 1] . \quad (8.3)$$

Here \mathbf{G} , \mathbf{G}_0 and \mathcal{D} are matrices. Since the fields are separated in a basis parallel and orthogonal to the direction \hat{n} of the classical field $\langle \vec{\Phi} \rangle = \sqrt{N} \hat{n} \phi$, these matrices become diagonal with one entry for the parallel component and $(N - 1)$ identical entries for the orthogonal ones. We denote them as σ and π so that we obtain

$$i\mathcal{D}_\sigma^{-1} = -\partial_\mu \partial^\mu - \lambda(3\phi^2 - v^2) \quad (8.4a)$$

$$i\mathcal{D}_\pi^{-1} = -\partial_\mu \partial^\mu - \lambda(\phi^2 - v^2) . \quad (8.4b)$$

For technical reasons we have normalized the matrix of GREEN functions \mathbf{G} with respect to a matrix of free GREEN functions \mathbf{G}_0 whose diagonal entries are given by

$$G_{*,0}^{-1} = -\partial_\mu \partial^\mu - m_{*,0}^2 \quad \text{where } * = \sigma, \pi . \quad (8.5)$$

The remaining terms of the effective action are all two-particle irreducible vacuum FEYNMAN graphs with external lines $\sqrt{N} \phi(x) \delta i1$ and with GREEN functions \mathbf{G} as internal lines.

In the following we will consider the effective potential (instead of the effective action) at finite temperature using the MATSUBARA formalism. Then the one-loop term takes the form

$$\begin{aligned} V_{1\text{-loop}} = \frac{1}{2} \int_q \left\{ \ln [G_\sigma^{-1}(q) G_{\sigma,0}(q)] + (N-1) \ln [G_\pi^{-1}(q) G_{\pi,0}(q)] \right. \\ \left. - [m_{\sigma,0}^2 + \Sigma_\sigma(q) - \lambda(3\phi^2 - v^2)] G_\sigma(q) \right. \\ \left. - (N-1) [m_{\pi,0}^2 + \Sigma_\pi(q) - \lambda(\phi^2 - v^2)] G_\pi(q) \right\} . \end{aligned} \quad (8.6)$$

Here, the denominators in the logarithm are the reference GREEN functions

$$G_{*,0}^{-1}(\omega_n, p) = p^2 + \omega_n^2 + m_{*,0}^2 \quad (8.7)$$

and the self-energy $\Sigma_*(\omega_n, p)$ is defined as

$$\Sigma_*(\omega_n, p) = G_*^{-1}(\omega_n, p) - G_{*,0}^{-1}(\omega_n, p) . \quad (8.8)$$

Introducing the constants $m_{\sigma,0}$ and $m_{\pi,0}$ is equivalent to adding a (temperature-dependent) constant to the effective potential. An obvious choice would be to use the bare physical masses, but this would imply $m_{\pi,0}^2 = 0$, leading immediately to infrared singularities. As we anticipate that the symmetry may not be broken at NLO of a $1/N$ expansion, we prefer a symmetric choice: $m_{*,0}^2 = \lambda v^2$ for both $* = \sigma$ and $* = \pi$, so that the GREEN functions become

$$G_*^{-1}(\omega, p) = \omega^2 + p^2 + m_0^2 + \Sigma_*(\omega, p) . \quad (8.9)$$

The one-loop potential (8.6) is divergent. Assuming that the self-energy decreases sufficiently fast at high momenta the logarithms will do so as well. Asymptotically, the integrand in Eq.(8.6) behaves like

$$\{\dots\} \simeq -\frac{m_0^2 - \lambda(3\phi^2 - v^2)}{q^2 + \omega_n^2 + m_0^2} - (N-1) \frac{m_0^2 - \lambda(\phi^2 - v^2)}{q^2 + \omega_n^2 + m_0^2} . \quad (8.10)$$

The integral of the one-loop effective action can be regulated by subtracting this term and by adding it in regularized form. We have

$$\begin{aligned} V_{1\text{-loop}}^{\text{ren.}} &= V_{1\text{-loop}} - [m_0^2 - \lambda(3\phi^2 - v^2)] \mathcal{B}_{\sigma,0} - (N-1) [m_0^2 - \lambda(\phi^2 - v^2)] \mathcal{B}_{\pi,0} \\ &+ \frac{1}{2} T \sum_{m=-\infty}^{\infty} \int_{-\infty}^{\infty} \frac{dq}{2\pi} \left\{ \frac{m_0^2 - \lambda(3\phi^2 - v^2)}{q^2 + \omega_n^2 + m_0^2} + (N-1) \frac{m_0^2 - \lambda(\phi^2 - v^2)}{q^2 + \omega_n^2 + m_0^2} \right\} \end{aligned} \quad (8.11)$$

where $\mathcal{B}_{*,0}$ are the bubble diagrams [cf. Eq. (4.1)] which we regularize dimensionally as

$$\begin{aligned} \mathcal{B}_{*,0} &= T \sum_{m=-\infty}^{\infty} \left(\frac{\bar{\mu}_R^2}{4\pi e^{-\gamma_E}} \right)^{\epsilon/2} \int \frac{dq^{(1-\epsilon)}}{(2\pi)^{(1-\epsilon)}} G_{*,0}(\omega_m, q) \\ &= \frac{1}{4\pi} \left[\frac{2}{\epsilon} - \ln \frac{m_0^2}{\bar{\mu}_R^2} + \mathcal{O}(\epsilon) \right] + \int \frac{dq}{2\pi E_0} \frac{1}{e^{E_0/T} - 1} , \end{aligned} \quad (8.12)$$

where $E_0 = \sqrt{q^2 + m_0^2}$. We define their finite part $\mathcal{B}_{*,0,\text{fin}}$ using the $\overline{\text{MS}}$ prescription, leaving out the terms proportional to $2/\epsilon$ and taking the limit $\epsilon \rightarrow 0$. Then the renormalized bubble diagrams become

$$\mathcal{B}_* = \oint_p [G_*(p) - G_{*,0}(p)] + \mathcal{B}_{*,0,\text{fin}} \quad (8.13)$$

with

$$\mathcal{B}_{j,0,\text{fin}} = -\frac{1}{4\pi} \ln \frac{m_0^2}{\bar{\mu}_R^2} + \int \frac{dq}{2\pi E_0} \frac{1}{e^{E_0/T} - 1} . \quad (8.14)$$

For the renormalization scale we choose $\bar{\mu}_R^2 = m_0^2 = \lambda v^2$. In $1 + 1$ dimensions the theory is renormalized if the HAMILTONIAN is normal-ordered. This is not a unique prescription as normal-ordering may be done with respect to different masses of the bare quanta (CHANG, 1976; COLEMAN, 1975). A shift in these masses introduces a redefinition of the vacuum expectation value v , or of the mass parameter in the symmetric theory, as the change in normal ordering of the quartic term introduces a term quadratic in the fields. Our convention corresponds to normal-ordering with respect to bare quanta of mass λv^2 .

The first nontrivial term is the double-bubble diagram. As we consider here leading order and next-to-leading order contributions we have to calculate this diagram with the exact combinatorial factors for $O(N)$. It takes the form

$$\begin{aligned} V_{\text{db}} &= \frac{\lambda}{4N} \{ [\mathcal{B}_\sigma + (N-1)\mathcal{B}_\pi]^2 + 2[\mathcal{B}_\sigma^2 + (N-1)\mathcal{B}_\pi^2] \} \\ &= \frac{\lambda}{4N} [(N^2-1)\mathcal{B}_\pi^2 + 2(N-1)\mathcal{B}_\sigma\mathcal{B}_\pi + 3\mathcal{B}_\sigma^2] . \end{aligned} \quad (8.15)$$

If only these two contributions are considered, we obtain the HARTREE-FOCK approximation including daisy and super-daisy resummation. In writing down this contribution we have replaced the divergent bubble subdiagrams by the finite ones. This requires mass and vacuum energy counterterms which are fixed by the minimal subtraction prescription which eventually may be replaced by a precise renormalization condition.

From

$$V_{\text{HF}} = V_{1\text{-loop}} + V_{\text{db}} \quad (8.16)$$

we obtain the gap equations in the HARTREE-FOCK approximation from the stationarity condition $\delta V_{\text{HF}}/\delta G_* = 0$:

$$\Sigma_\sigma^{\text{HF}}(\omega_n, p) = -m_0^2 + \lambda(3\phi^2 - v^2) + \frac{\lambda}{N} [3\mathcal{B}_\sigma + (N-1)\mathcal{B}_\pi] \quad (8.17a)$$

$$\Sigma_\pi^{\text{HF}}(\omega_n, p) = -m_0^2 + \lambda(\phi^2 - v^2) + \frac{\lambda}{N} [\mathcal{B}_\sigma + (N+1)\mathcal{B}_\pi] . \quad (8.17b)$$

The large- N limit is obtained as a strict limit $N \rightarrow \infty$, *i.e.* by omitting the σ contribution entirely. Then the two DYSON-SCHWINGER equations become identical and only contain the pion bubble with $(N-1)/N$ replaced by unity.

The condition for a nontrivial extremum with respect to ϕ becomes

$$\mathcal{R}(\phi) = \frac{1}{N\phi} \frac{\partial V_{\text{HF}}}{\partial \phi} = \lambda(\phi^2 - v^2) + \frac{\lambda}{N} [3\mathcal{B}_\sigma + (N-1)\mathcal{B}_\pi] = 0 . \quad (8.18)$$

Again in the large- N limit the σ contribution is neglected and the prefactor $N/(N-1)$ of the pion bubble is replaced by unity.

At next-to-leading order in a $1/N$ expansion one has, in the absence of external fields, to sum over all diagrams which are traces of powers of the fish diagram, the so-called necklace diagrams, shown in Fig. 8.1 (see also Appendix C for details on counting orders of $1/N$). In order to go beyond the leading order we define several diagrams: We define the fish diagrams as

$$\mathcal{F}_{\sigma,\pi}(\omega_n, p) = T \sum_{m=-\infty}^{\infty} \int \frac{dq}{2\pi} G_{\sigma,\pi}(\omega_m, q) G_{\sigma,\pi}(\omega_n - \omega_m, p - q) \quad (8.19)$$

and denote by $\text{Tr } \mathcal{F}(\omega_n, p)$ the sum

$$\text{Tr } \mathcal{F}(\omega_n, p) = \mathcal{F}_{\sigma}(\omega_n, p) + (N-1) \mathcal{F}_{\pi}(\omega_n, p) . \quad (8.20)$$

The sum over the necklace without external fields, see Fig. 8.1, is then given by

$$\mathcal{N} = \frac{1}{2} \oint_q \left\{ \ln \left[1 + \frac{\lambda}{N} \text{Tr } \mathcal{F}(q) \right] - \frac{\lambda}{N} \text{Tr } \mathcal{F}(q) \right\} . \quad (8.21)$$

The subtraction of $\text{Tr } \mathcal{F}(q)$ accounts for the fact that we have already included the double-bubble diagrams. In the symmetric theory where the σ and π contributions are equal, the factor of N cancels, so this expression is of order N^0 which is NLO.

The same order in $1/N$ is achieved by replacing one of the σ lines of the necklace by $N\phi^2$. We will call this class of graphs “generalized sunsets”, see Fig. 8.2 for a graphical illustration. We introduce the derivative

$$\frac{\delta \mathcal{N}}{\delta \mathcal{G}_{\sigma}}(\omega_n, p) = \frac{\lambda}{N} T \sum_m \int \frac{dq}{2\pi} \frac{-\frac{\lambda}{N} \text{Tr } \mathcal{F}(\omega_m, q)}{1 + \frac{\lambda}{N} \text{Tr } \mathcal{F}(\omega_m, q)} G_{\sigma}(\omega_n - \omega_m, p - q) . \quad (8.22)$$

Note that the overall factor λ/N arises from the derivative of the expression $\frac{\lambda}{N} \text{Tr } \mathcal{F}(\omega_n, p)$ with respect to G_{σ} . We obtain for the generalized sunset diagram, or sum over necklace diagrams with two external lines,

$$\mathcal{S} = N\phi^2 \frac{\delta \mathcal{N}}{\delta \mathcal{G}_{\sigma}}(0, 0) = \lambda\phi^2 \oint_q \frac{-\frac{\lambda}{N} \text{Tr } \mathcal{F}(q)}{1 + \frac{\lambda}{N} \text{Tr } \mathcal{F}(q)} G_{\sigma}(q) . \quad (8.23)$$

The functional derivative contains a factor $1/N$ so that this expression is of order N^0 . Expanding the denominator in Eq. (8.23) one finds all graphs shown in Fig. 8.2.

With these definitions the 2PI effective potential up to NLO becomes

$$V_{\text{eff}}[\mathbf{G}, \phi] = V_{\text{class}}[\phi] + V_{1\text{-loop}}[\mathbf{G}, \phi] + V_{\text{db}}[\mathbf{G}] + \mathcal{S}[\mathbf{G}, \phi] + \mathcal{N}[\mathbf{G}] . \quad (8.24)$$

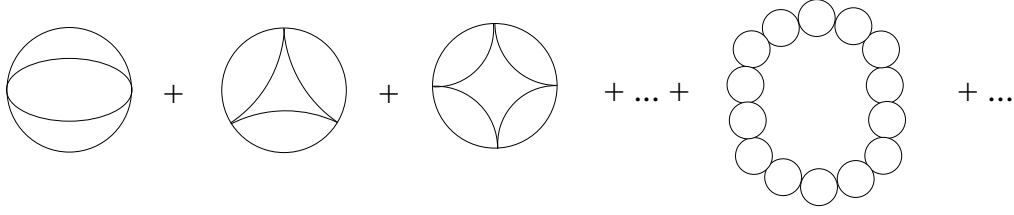


Figure 8.1: Resummation of necklace graphs.

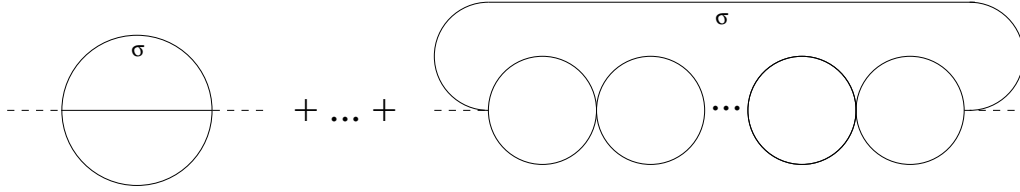


Figure 8.2: Generalized sunset graphs.

In order to write down the gap equations we need to introduce a further functional derivative

$$\frac{\delta \mathcal{S}}{\delta G_*}(\omega_n, p) = N\phi^2 \frac{\delta}{\delta G_*(\omega_n, p)} \left[\frac{\delta \mathcal{N}}{\delta \mathcal{G}_\sigma}(0, 0) \right]. \quad (8.25)$$

Explicitly it is given by

$$\frac{\delta \mathcal{S}}{\delta \mathcal{G}_*}(p) = \frac{\lambda^2}{N} \phi^2 \int_q \frac{G_\sigma(q) G_*(p-q)}{-[1 + \frac{\lambda}{N} \text{Tr } \mathcal{F}(q)]^2} + \lambda \phi^2 \delta_{*,\sigma} \frac{-\frac{\lambda}{N} \text{Tr } \mathcal{F}(p)}{1 + \frac{\lambda}{N} \mathcal{F}(p)}. \quad (8.26)$$

With these definitions the DYSON-SCHWINGER equations become

$$\begin{aligned} \Sigma_\sigma(\omega_n, p) &= -m_0^2 + \lambda(3\phi^2 - v^2) + \frac{\lambda}{N} [(N-1) \mathcal{B}_\pi + 3\mathcal{B}_\sigma] \\ &\quad + \frac{\delta \mathcal{N}}{\delta G_\sigma}(\omega_n, p) + \frac{\delta \mathcal{S}}{\delta G_\sigma}(\omega_n, p) \end{aligned} \quad (8.27a)$$

$$\begin{aligned} \Sigma_\pi(\omega_n, p) &= -m_0^2 + \lambda(\phi^2 - v^2) + \frac{\lambda}{N} [(N+1) \mathcal{B}_\pi + \mathcal{B}_\sigma] \\ &\quad + \frac{\delta \mathcal{N}}{\delta G_\pi}(\omega_n, p) + \frac{\delta \mathcal{S}}{\delta G_\pi}(\omega_n, p) \end{aligned} \quad (8.27b)$$

All expressions in these equations have been given explicitly above. Finally for the partial derivative of V_{eff} with respect to ϕ we find

$$\mathcal{R}(\phi) = \frac{1}{N\phi} \frac{\partial V_{\text{eff}}}{\partial \phi} = \lambda(\phi^2 - v^2) + \frac{\lambda}{N} [3\mathcal{B}_\sigma + (N-1) \mathcal{B}_\pi] + 2 \frac{\lambda}{N} \frac{\delta \mathcal{N}}{\delta G_\sigma}(0, 0). \quad (8.28)$$

The solution $\bar{\mathbf{G}}$ of the DYSON-SCHWINGER equations (8.27) yield the propagators as functions of the condensate ϕ . Substituting these solutions into the 2PI effective potential at NLO, Eq. (8.24), we find the one-particle irreducible (1PI) effective potential which is only a function of ϕ

$$V_{\text{eff}}^{\text{1PI}}(\phi) = V_{\text{eff}}^{\text{2PI}}[\bar{\mathbf{G}}(\phi), \phi] .$$

Analyzing the (1PI) graphs which $V_{\text{eff}}^{\text{1PI}}$ consists of, one finds *all* graphs of LO and NLO in $1/N$ plus an infinite number of graphs of any higher order of $1/N$ but not *all* of them (cf. Appendix C.4 for more details). We conclude that the 2PI effective potential at NLO has an error of NNLO.

8.2 2PPI effective action at NLO

The derivation of the *two-particle point-irreducible* effective action (VERSCHELDE and COPPENS, 1992, 1993) is similar to that of the 2PI one. One introduces a quadratic source term $K_{ij}(x) \Phi_i(x) \Phi_j(x)$ which, in contrast to the 2PI formalism, is local. The LEGENDRE transformed variables are then $\phi(x)$ and $\Delta_{ij}(x)$. For a detailed comparison between the 2PI and 2PPI formalism the reader is referred to Appendix C of this thesis or an earlier publication (BAACKE and MICHALSKI, 2003a, Appendix A).

For a translational invariant system ϕ and Δ_{ij} are constants. The effective action then becomes an ordinary function of these variables. In the $O(N)$ model, the classical field is a vector $\langle \vec{\Phi} \rangle = \hat{n} \phi$. As for the 2PI formalism we use a basis where the σ field is in the direction \hat{n} and the $N - 1$ pion fields span the orthogonal directions. Then Δ_{ij} is a $N \times N$ matrix which becomes diagonal in this basis, with one entry Δ_σ and $N - 1$ entries Δ_π . In contrast to the 2PI formalism, the GREEN functions take the simple form

$$G_*(p, \omega_n) = \frac{1}{p^2 + \omega_n^2 + M_*^2} \quad (8.29)$$

with the effective masses (BAACKE and MICHALSKI, 2003a; VERSCHELDE and DE PESSEMIER, 2002)

$$M_\sigma^2 = \lambda [3\phi^2 - v^2 + 3\Delta_\sigma + (N - 1)\Delta_\pi] \quad (8.30a)$$

$$M_\pi^2 = \lambda [\phi^2 - v^2 + \Delta_\sigma + (N + 1)\Delta_\pi] . \quad (8.30b)$$

Here the local mass insertions Δ_* are given by

$$\Delta_\sigma = 2 \frac{\partial \Gamma_{\text{q}}^{\text{2PPI}}}{\partial M_\sigma^2} \quad \text{and} \quad \Delta_\pi = \frac{2}{N - 1} \frac{\partial \Gamma_{\text{q}}^{\text{2PPI}}}{\partial M_\pi^2} , \quad (8.31)$$

where $\Gamma_q^{2\text{PPI}}$ is the sum of all two particle point irreducible graphs. These are all graphs that do not fall apart if two internal lines meeting at one point are cut (VERSHELDE and COPPENS, 1992). They are computed with the propagators defined in Eq. (8.29).

It is simpler to express the potential in terms of the effective masses M_σ^2 and M_π^2 instead of the parameters Δ_σ and Δ_π . Then these gap equations can be derived from the effective potential

$$U_{\text{eff}}(\phi; M_\sigma^2, M_\pi^2) = N U_{\text{cl}}(\phi, M_\sigma^2, M_\pi^2) + U_q(\phi, M_\sigma^2, M_\pi^2) . \quad (8.32)$$

Here U_{cl} is the “classical” potential (BAACKE and MICHALSKI, 2003a; NEMOTO *et al.*, 2000)

$$U_{\text{cl}} = \frac{1}{2} M_\sigma^2 \phi^2 - \frac{\lambda}{2} \phi^4 - \frac{v^2}{2\lambda(N+2)} \{M_\sigma^2 + (N-1)M_\pi^2\} \\ - \frac{1}{8\lambda(N+2)} [(N+1)M_\sigma^4 + 3(N-1)M_\pi^4 - 2(N-1)M_\sigma^2 M_\pi^2 + 2N\lambda^2 v^4] , \quad (8.33)$$

which in this formulation already includes quantum parts through the effective masses. In this sense the separation between U_{cl} and the quantum part U_q is superficial. The basic contribution to U_q is the one-loop contribution

$$U_{1\text{-loop}} = \frac{1}{2} \text{Tr} \ln[G_\sigma^{-1} G_{\sigma,0}] + \frac{N-1}{2} \text{Tr} \ln[G_\pi^{-1} G_{\pi,0}] , \quad (8.34)$$

which explicitly reads

$$U_{1\text{-loop}} = \frac{1}{2} T \sum_n \int \frac{dp}{2\pi} \left\{ \ln \frac{p^2 + \omega_n^2 + M_\sigma^2}{p^2 + \omega_n^2 + m_0^2} + (N-1) \ln \frac{p^2 + \omega_n^2 + M_\pi^2}{p^2 + \omega_n^2 + m_0^2} \right\} . \quad (8.35)$$

In regularized and renormalized form it becomes

$$U_{1\text{-loop}} = \frac{1}{2} T \sum_n \int \frac{dp}{2\pi} \left\{ \ln \frac{p^2 + \omega_n^2 + M_\sigma^2}{p^2 + \omega_n^2 + m_0^2} + (N-1) \ln \frac{p^2 + \omega_n^2 + M_\pi^2}{p^2 + \omega_n^2 + m_0^2} \right. \\ \left. - \frac{M_\sigma^2 - m_0^2}{p^2 + \omega_n^2 + m_0^2} - (N-1) \frac{M_\pi^2 - m_0^2}{p^2 + \omega_n^2 + m_0^2} \right\} \\ + \frac{1}{2} (M_\sigma^2 - m_0^2) \mathcal{B}_\sigma + \frac{N-1}{2} (M_\pi^2 - m_0^2) \mathcal{B}_\pi . \quad (8.36)$$

The regularized bubble integrals have been defined in Eq. (8.12). If we include just $U_{1\text{-loop}}$ we again obtain the HARTREE-FOCK approximation with $\Delta = \mathcal{B}$. The double-bubble diagrams are included here in U_{cl} via the effective masses.

Going beyond the HARTREE-FOCK approximation in the 2PPI formalism in a strict $1/N$ expansion we only have to take into account necklaces and generalized sunsets and a two-particle *point*-irreducible but two-particle *reducible* combination of them. The necklace \mathcal{N} takes the same form as for the 2PI formalism, see Eq. (8.21) and Fig. 8.1, where of course the fish diagram, Eq. (8.20), is computed with the propagators of Eq. (8.29). The generalized sunset contribution is replaced by a more complex set of graphs. As discussed by ROOT (1974), at next-to-leading order of a $1/N$ expansion the graphs with external lines have the form presented in Fig. 8.3, with alternating sigma propagators and necklaces (see also discussion in Appendix C.1.2). As the resemblance to a sunset becomes now very remote we refer to them as *chain diagrams*. These are summed up in the form

$$\mathcal{C} = \frac{1}{2} \not\int_q \ln [1 - 2 \lambda \phi^2 \mathbf{S}(q)] \quad (8.37)$$

where \mathbf{S} is the kernel of the generalized sunset diagram (8.23),

$$\mathbf{S}(\omega_m, q) = \frac{\frac{\lambda}{N} \text{Tr } \mathcal{F}(\omega_m, q)}{1 + \frac{\lambda}{N} \mathcal{F}(\omega_m, q)} G_\sigma(\omega_m, q). \quad (8.38)$$

In the 2PI formalism the higher powers of insertions \mathbf{S} are included automatically, here the summation has to be done explicitly, *i.e.*, the sum of generalized sunsets (Fig. 8.2) is a subset of the sum of chain graphs (Fig. 8.3).

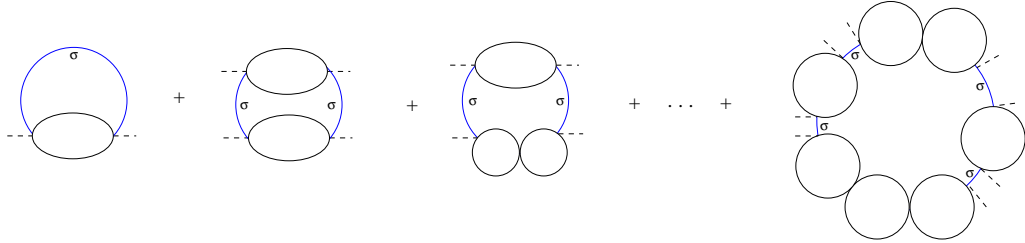


Figure 8.3: 2PPI or 1PI "chain" contributions to the effective action.

With the graphs defined in the previous paragraph the quantum part of the effective potential takes the form

$$U_q = U_{1\text{-loop}} + \mathcal{N} + \mathcal{C} \quad (8.39)$$

and the insertions $\Delta_{\sigma,\pi}$ in the gap equations are given by

$$\Delta_\sigma(M_\sigma^2, M_\pi^2) = \mathcal{B}_\sigma + 2 \frac{\partial \mathcal{N}}{\partial M_\sigma^2} + 2 \frac{\partial \mathcal{C}}{\partial M_\sigma^2} \quad (8.40a)$$

$$\Delta_\pi(M_\sigma^2, M_\pi^2) = \mathcal{B}_\pi + \frac{2}{N-1} \frac{\partial \mathcal{N}}{\partial M_\pi^2} + \frac{2}{N-1} \frac{\partial \mathcal{C}}{\partial M_\pi^2}. \quad (8.40b)$$

Explicitly the contributions beyond HARTREE-FOCK are given by

$$\frac{\partial \mathcal{N}}{\partial M_*^2} = \frac{\lambda}{2N} \not\int_q \frac{-\frac{\lambda}{N} \text{Tr } \mathcal{F}(q)}{1 + \frac{\lambda}{N} \text{Tr } \mathcal{F}(q)} \frac{\partial \text{Tr } \mathcal{F}(q)}{\partial M_*^2} \quad (8.41)$$

and

$$\frac{\partial \mathcal{C}}{\partial M_*^2} = -\lambda \phi^2 \not\int_q \frac{1}{1 - 2\lambda \phi^2 \mathbf{S}(q)} \left\{ \frac{\lambda}{N} \frac{G_\sigma(q)}{[1 + \frac{\lambda}{N} \mathcal{F}(q)]^2} \frac{\partial \text{Tr } \mathcal{F}(q)}{\partial M_j^2} - \delta_{*,\sigma} \frac{\frac{\lambda}{N} \text{Tr } \mathcal{F}(q)}{1 + \frac{\lambda}{N} \text{Tr } \mathcal{F}(q)} G_\sigma^2(q) \right\}. \quad (8.42)$$

Finally the derivatives of the trace of fish graphs read

$$\frac{\partial \text{Tr } \mathcal{F}(p, \omega_n)}{\partial M_\sigma^2} = -2 \not\int_q \frac{1}{(q^2 + M_\sigma^2) [(p-q)^2 + M_\sigma^2]^2} \quad (8.43)$$

$$\frac{\partial \text{Tr } \mathcal{F}(p, \omega_n)}{\partial M_\pi^2} = -2(N-1) \not\int_q \frac{1}{(q^2 + M_\pi^2) [(p-q)^2 + M_\pi^2]^2}. \quad (8.44)$$

The partial derivative of V_{eff} with respect to ϕ , divided by $N\phi$, in analogy to Eq. (8.28) is given by

$$\mathcal{R}(\phi) = M_\sigma^2 - 2\lambda \phi^2 + \frac{1}{N\phi} \frac{\partial \mathcal{C}}{\partial \phi} \quad (8.45)$$

with

$$\frac{1}{N\phi} \frac{\partial \mathcal{C}}{\partial \phi} = -\frac{2}{N} \not\int_q \frac{\mathbf{S}(q)}{1 - 2\lambda \phi^2 \mathbf{S}(q)}. \quad (8.46)$$

Here as well, we find the 1PI effective potential by substituting the solutions of the gap equations (8.40) and (8.30) back into the 2PPI effective potential. An analysis in terms of 1PI graphs shows that, like the 2PI effective potential, the 2PPI potential at NLO also contains graphs of any higher order of $1/N$. Though in the 2PPI formalism those graphs emerge from the resummation of NLO bubble corrections (see Appendix C.2.3 for details). Nevertheless, the error remains of NNLO.

8.3 1PI effective action with auxiliary fields at NLO

In a seminal article, ROOT (1974) has discussed a $1/N$ expansion up to next-to-leading using a 1PI effective potential with an auxiliary field. In the language of this

chapter, this field can be identified with a self-consistent pion mass M_π^2 . For further details we refer to Section C.3 of Appendix C. In the auxiliary field formalism the classical potential takes the form

$$U_{\text{cl}}(\phi, M_\pi^2) = N \left[\frac{1}{2} M_\pi^2 (\phi^2 - v^2) - \frac{M_\pi^4}{4\lambda} \right], \quad (8.47)$$

which can be obtained by taking the strict limit $N \rightarrow \infty$ of the analogous potential of the 2PPI formalism, Eq. (8.33), when the mass of the σ propagator is given by

$$M_\sigma^2 = M_\pi^2 + 2\lambda\phi^2. \quad (8.48)$$

To leading order in $1/N$ this would follow in the 2PPI formalism when taking only the pions into account in the one-loop terms. In ROOT's work this relation is kept fixed for all orders of $1/N$. In a strict $1/N$ counting one may indeed neglect corrections of NLO to the propagator, as actually suggested in ROOT's article by using the only the leading order gap equation. As in the 2PPI formalism the propagators take the tree level form of Eq. (8.29).

In the following we will rewrite the various terms included by ROOT (1974) in a way that makes the correspondence to the other formalisms more transparent. Including the next-to-leading order corrections the one-loop term takes the form of Eqs. (8.34) to (8.36), with M_σ^2 given by Eq. (8.48). As in the 2PPI formalism the following terms in the $1/N$ expansion are the necklace and the chain diagrams. In the necklace part only the pion fish diagram is taken into account. The definition of the necklace contribution is then identical to the one in the 2PI formalism, Eq. (8.21), with the modification that $\text{Tr } \mathcal{F} \equiv N \mathcal{F}_\pi$ and that the propagators in the fish graph, Eq. (8.20) are given by Eq. (8.29).

The chain diagram \mathcal{C} takes the same form as in the 2PPI formalism, see Eqs. (8.37) and (8.38), of course now with $\text{Tr } \mathcal{F} = N \mathcal{F}_\pi$. When taking the derivatives the σ propagator must be considered as a function of M_π^2 and ϕ according to Eq. (8.48). Its derivatives are

$$\frac{\partial G_\sigma}{\partial \phi} = -4\lambda\phi G_\sigma^2 \quad \text{and} \quad \frac{\partial G_\sigma}{\partial M_\pi^2} = -G_\sigma^2.$$

The quantum corrections to the gap equations are derivatives with respect to the pion mass

$$\frac{\partial \mathcal{C}}{\partial M_\pi^2} = \int_q \frac{-\lambda\phi^2}{1 - 2\lambda\phi^2 \mathbf{S}(q)} \left\{ \frac{\lambda}{[1 + \lambda \mathcal{F}_\pi(q)]^2} \frac{\partial \mathcal{F}_\pi(q)}{\partial M_\pi^2} G_\sigma(q) - \mathbf{S}(q) G_\sigma(q) \right\}. \quad (8.49)$$

Finally the gap equation is

$$M_\pi^2 = \lambda \left(\phi^2 - v^2 + \frac{2}{N} \frac{\partial \mathcal{N}}{\partial M_\pi^2} + \frac{2}{N} \frac{\partial \mathcal{C}}{\partial M_\pi^2} \right) \quad (8.50)$$

where $\partial\mathcal{N}/\partial M_\pi^2$ is given by Eq. (8.41). The derivative of all chain graphs with respect to the condensate is

$$\frac{1}{N_\phi} \frac{\partial\mathcal{C}}{\partial\phi} = -2 \frac{\lambda}{N} \int_q \frac{\mathbf{S}(\mathbf{q})}{1 + \mathbf{S}(q)} [1 - 2\lambda\phi^2 G_\sigma(q)] , \quad (8.51)$$

so that the quantity \mathcal{R} is given by

$$\mathcal{R}(\phi) = M_\sigma^2 - 2\lambda\phi^2 + \frac{1}{N_\phi} \frac{\delta\mathcal{C}}{\delta\phi} . \quad (8.52)$$

In contrast to the 2PI and the 2PPI effective potential, the NLO-1PI potential in the auxiliary-field formalism does not contain any contributions from higher orders. So it is well-suited for comparisons with the other two potentials.

Chapter 9

Numerical results

The equations of the previous section are easily incorporated into a computer code; we solve the gap equations by iteration, calculate the effective potential and look for nontrivial minima which is a sign of spontaneous symmetry breaking that is unexpected according to COLEMAN (1973). Note, that it does not suffice to look at the variational pion mass, *i.e.* the value of the inverse pion propagator at zero momentum because global symmetries may be violated by resummation schemes (VAN HEES and KNOLL, 2002a). But a nontrivial minimum in the effective potential is equivalent to the existence of GOLSTONE bosons (cf. Section 5.2.1).

The range of momenta and MATSUBARA frequencies was restricted to values smaller than $15 - 20v$, far above the relevant mass scales. All numerical integrals and summations are ultraviolet finite by the regularization presented in the previous section.

At fixed N, v, λ, T and ϕ we start the iteration with a GREEN function $G_* = G_0$. The convergence is monitored by the values of the trace of bubble diagrams

$$\text{Tr } \mathcal{B} = (N - 1)\mathcal{B}_\pi + \mathcal{B}_\sigma . \quad (9.1)$$

Since integrals of functions are less sensitive to changes than the functions themselves, we considered the iteration to have reached the solution if the relative change of this global quantity has become smaller than 10^{-8} .

For temperatures of the order of v this procedure converges well (BAACKE and MICHALSKI, 2004a). Problems arise if the temperature is low, typically less than $v/5$ and for ϕ typically less than $v/2$. In these regions the pion propagator becomes large at small (ω_n, p) obviously due to a pion pole approaching $p^2 = 0$ from negative (MINKOWSKIAN) p^2 . This situation is close to an infrared divergence, and small changes of the pion GREEN function result in large changes of the various integrals.

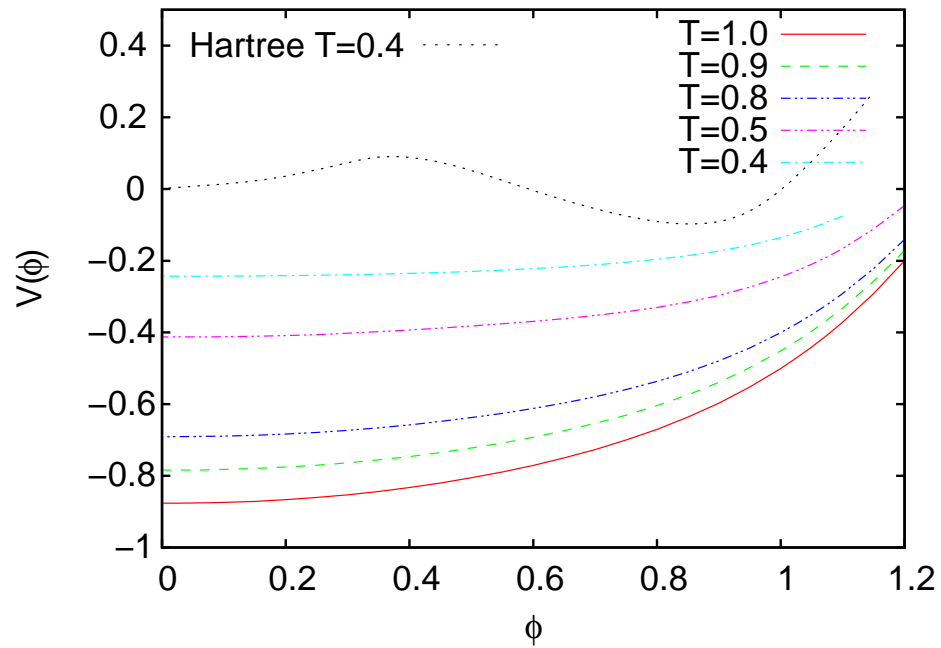
One can extend the domain of convergence by using an underrelaxation, defining the n th step of the iteration of Eqs. (8.27) by taking the result $\Sigma^{(n-1)}$ of the previous step multiplied by a factor of α plus the right hand sides of these equations multiplied by $(1 - \alpha)$. We have chosen α typically between 0.5 and 0.95.

To ensure the consistency of our search for extrema, both in the analytic formulas and in the numerical computations we have not only computed the results for $\partial V_{\text{eff}}[\phi, \bar{\mathbf{G}}]/\partial\phi$ but also the 1PI effective potential $V_{\text{eff}}[\phi, \bar{\mathbf{G}}]$ itself. Here in both cases $\bar{\mathbf{G}}$ represents the solutions of the gap equations; so both V_{eff} and $\partial V_{\text{eff}}/\partial\phi$ are evaluated at $\delta V_{\text{eff}}/\delta G = 0$ and the extrema of the potential $V_{\text{eff}}[\phi, \bar{\mathbf{G}}]$ should coincide with the zeros of $\partial V_{\text{eff}}[\phi, \bar{\mathbf{G}}]/\partial\phi$. For the computations in the 2PI scheme we do not find any nontrivial minima, so all we check here is that $\mathcal{R}(\phi)$ has no zeros. For the HARTREE-FOCK approximation and for the 2PPI scheme, the extrema of the potential and the zeros of $\mathcal{R}(\phi)$ agree within the available accuracy.

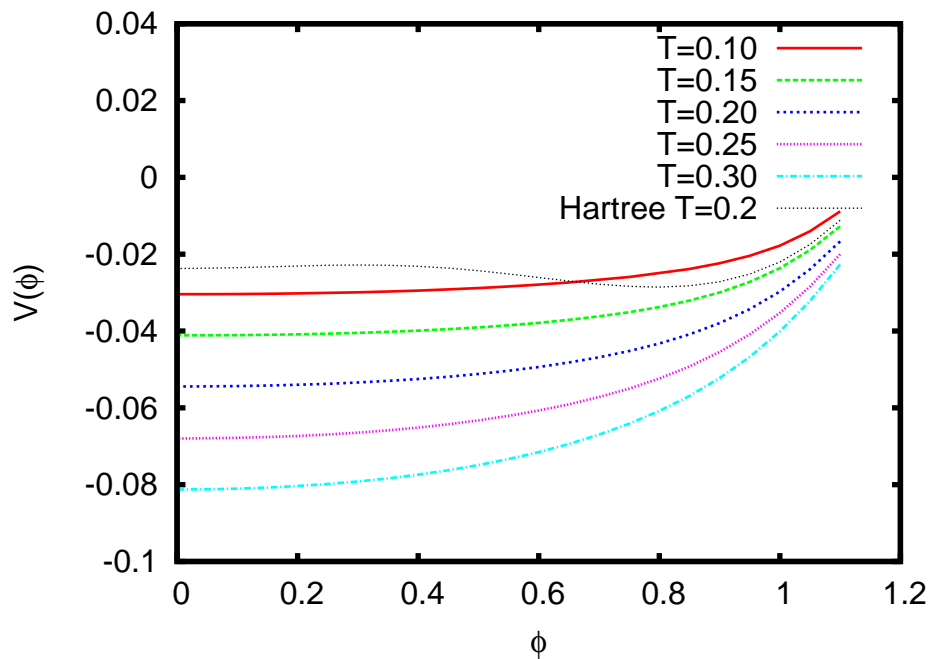
In the following we will discuss results of various calculations of the effective potential shown in Figs. 9.1 and 9.2. The 2PI effective potential for $N = 4$ and two different values of the coupling λ (Fig. 9.1) is totally convex and exhibits no inflection points. This is a clear sign for a symmetric phase. For comparison we also plot the potential in the HARTREE-FOCK approximation for one of the temperatures. It has a nontrivial minimum that changes to an inflection point at higher temperatures. This is a clear sign of a first-order phase transition. We conclude that the HARTREE-FOCK approximation does not obey COLEMAN's theorem.

In Fig. 9.2 we show the comparison between the HARTREE-FOCK, the 2PPI-NLO and 1PI NLO approximation and the convergence towards the leading order large- N results. These results are for $v = 1$, $\lambda = 0.5$ and $T = 0.5v$. The effective potential in the 2PPI approximation is always in between those of the HARTREE-FOCK and 2PI-NLO approximation. The 1PI-NLO effective potential is close to the 2PI results. The latter two approximations differ only by terms of next-to-next-to-leading order (NNLO); it is surprising, nevertheless, that these terms are small already at moderate values of N . As N is finite one expects differences to the large- N result, the deviations of the various approximations from this limit do not *a priori* establish any "ranking"; however, the spontaneous symmetry breaking displayed by the HARTREE-FOCK and 2PPI-NLO approximations is certainly unphysical.

In Fig. 9.3 we display the spectral behavior of the effective momentum-dependent masses $m_0^2 + \Sigma(\omega_n, p)$, see Eqs. (8.27), at the equilibrium point $\phi = 0$, for various temperatures, $N = 4$ and $\lambda = 0.5$. We plot these quantities versus the "EUCLIDEAN momentum" $p_E = \sqrt{\omega_n^2 + p^2}$. The curves for various MATSUBARA frequencies ω_n are close together, implying an approximate rotational symmetry in the EUCLIDEAN (ω, p) plane. Whereas the large-momentum behavior is determined by a constant



(a) $\lambda = 0.5$. The HARTREE-FOCK result is multiplied by a factor of 10.



(b) $\lambda = 0.1$

Figure 9.1: HARTREE-FOCK and 2PI effective potential at NLO of a $1/N$ expansion for $N = 4$.

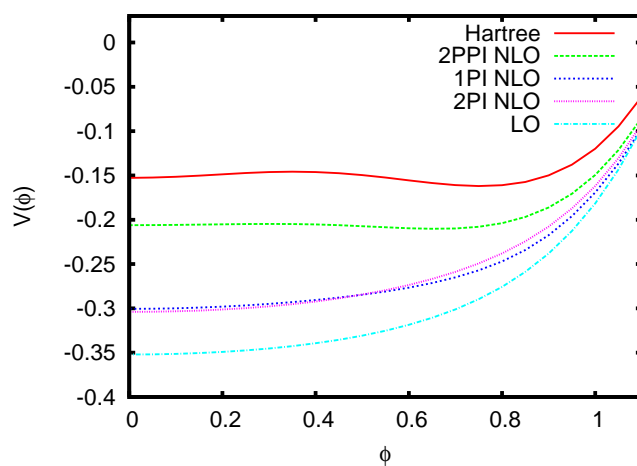
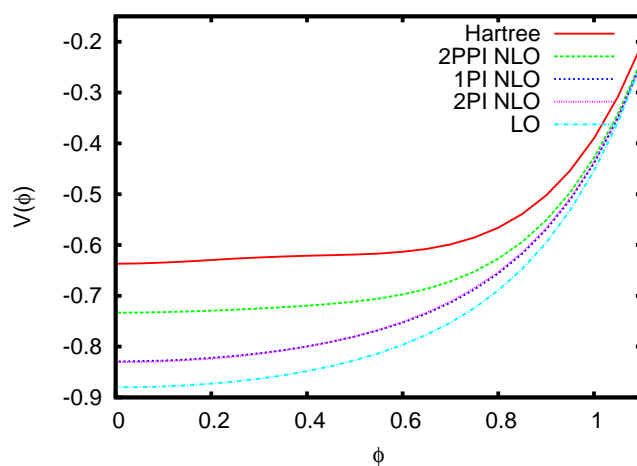
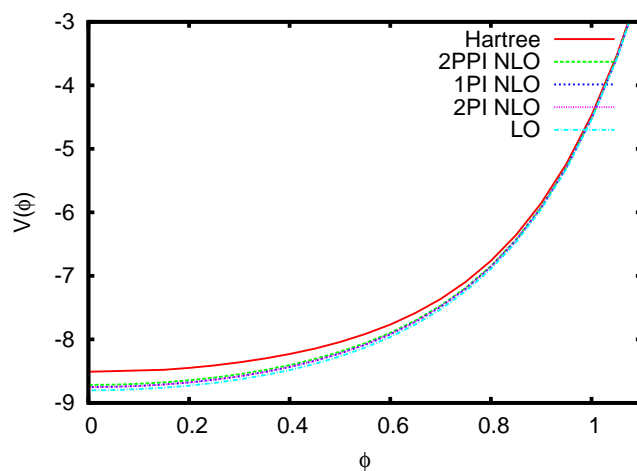
(a) $N = 4$ (b) $N = 10$ (c) $N = 100$

Figure 9.2: Comparison of the effective potentials for different values of N obtained in the HARTREE-FOCK, 2PPI-NLO, 1PI-NLO, 2PI-NLO and LO- $1/N$ approximations for $\lambda = 0.5$ and $T = 0.5$.

effective mass given by the tree-level and bubble contributions, the effective masses at low momenta are considerably smaller, so that the various loop integrals are infrared-enhanced. The infrared enhancement can also be seen in Fig. 9.4 where

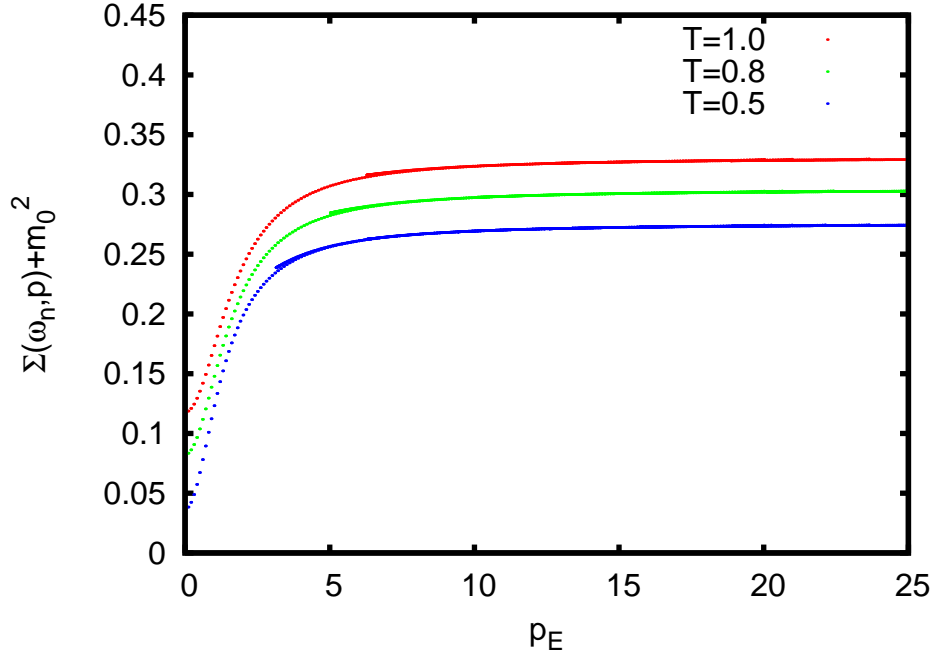


Figure 9.3: Momentum-dependent masses, cf. Eqs. (8.27), for different temperatures. $N = 4$, $\lambda = 0.5$. Here $p_E = \sqrt{\omega_n^2 + p^2}$.

we plot, for $\lambda = 0.1$, the values of the effective masses at the equilibrium point $\phi = 0$. We display $m_0^2 + \Sigma(0, 0)$ and $m_0^2 + \Sigma(0, p_{\max})$, where p_{\max} is our pragmatic momentum cutoff. The values near $p = 0$ are much smaller than those at p_{\max} .

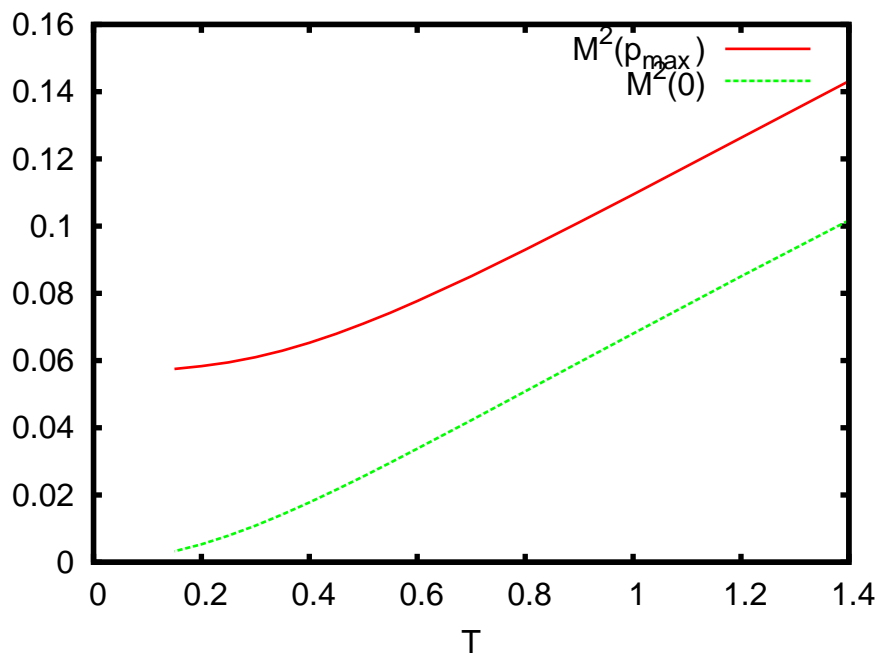


Figure 9.4: Temperature dependence of the effective masses $M^2(p) = m_0^2 + \Sigma(\omega = 0, p)|_{\phi=0}$ at zero momentum ($p = 0$) and in the asymptotic region ($p = p_{\max}$) for $\lambda = 0.1$ and $N = 4$.

Chapter 10

Conclusions and outlook

In Part II of this thesis, we have analyzed the effective potential of the $O(N)$ linear sigma model at next-to-leading order of a $1/N$ expansion in three different resummation formalisms. We have worked in two spacetime dimensions to check whether the effective potentials are convex which is expected from the non-existence of GOLDSTONE bosons in two dimensions (COLEMAN, 1973). In order to do so, we have solved the coupled system of EUCLIDEAN DYSON-SCHWINGER equations for the σ and pion propagators.

We have found that within our range of parameters the 2PI and the 1PI-auxiliary-field effective potential do not exhibit spontaneous symmetry breaking as expected in a two-dimensional model. Furthermore, we find that the thermal propagators are enhanced in the infrared region. Due to momentum-dependent self-energy insertions the effective masses at low EUCLIDEAN momenta are smaller than those at large momenta.

We have compared the effective potentials in all three formalisms with each other. As expected from a strict limit $N \rightarrow \infty$, with rising N all three NLO-potentials converge to the leading-order results. A theoretical analysis shows that the potential in all three schemes is exact up to errors of NNLO (cf. Appendix C for further details). Both the 2PPI and the 2PI potential have an infinite number of contributions from *any* order of $1/N$ beyond NLO whereas the 1PI auxiliary-field potential does only consist of LO and NLO contributions. The numerical results show that, at NLO, the 1PI effective potential is close to the NLO-2PI potential even for small N , whereas the potential obtained in the 2PPI-NLO approximation lies between that obtained in the HARTREE-FOCK and those in the 2PI and 1PI formalisms. The HARTREE-FOCK and 2PPI-NLO approximations display spontaneous symmetry breaking, unphysical in $1 + 1$ dimensions. This is clearly an artefact of

these approximations emerging from higher-order contributions; HARTREE-FOCK is a mixture of LO- $1/N$ and all super-daisy graphs which contribute to any order of $1/N$. The 2PPI-NLO approximation is exact up to NLO but comprises a resummation of bubble-shaped propagator corrections. These graphs are of NNLO (and higher) but, however, they induce a HARTREE-FOCK-like correction to the NLO- $1/N$ potential that decreases with larger values of N but causes a first-order phase transition. The 1PI graphs beyond NLO inherent in the 2PI effective potential are obviously better “chosen” than those in the 2PPI formalism; even at small values of N there is only a slight difference between the effective potentials of the 2PI and the 1PI formalism. So, the contributions from higher orders do not spoil any symmetries. In fact, in an analysis of critical phenomena of the $O(N)$ linear sigma model ALFORD *et al.* (2004) have found that for small N the 2PI formalism at NLO converges faster to the exact results than the 1PI one.

In this work we were concerned with the phase structure of the model in different resummation schemes at next-to-leading order of a $1/N$ expansion. It would be useful to extend this analysis to $3+1$ dimensions using recently developed renormalizations techniques for 2PI-resummed perturbation theory BLAIZOT *et al.* (2004); COOPER *et al.* (2004); VAN HEES and KNOLL (2002a,b,c).

Appendix A

Effective action of the $U(2)_L \times U(2)_R$ linear sigma model

This Appendix contains details for the computation of the equations of motion in the $1/N_f$ expansion of the 2PI effective action of the $U(2)_L \times U(2)_R$ model and especially the chosen approximation as sketched in Chapter 2.

We recall the classical action in EUCLIDEAN spacetime ¹

$$\mathcal{S}[\Phi] = \int_x \mathcal{L}[\Phi] = \int_x \left\{ \text{Tr} (\partial_\mu \Phi^\dagger \partial^\mu \Phi + m^2 \Phi^\dagger \Phi) + \frac{\lambda_1}{N_f^2} [\text{Tr} (\Phi^\dagger \Phi)]^2 + \frac{\lambda_2}{N_f} \text{Tr} [(\Phi^\dagger \Phi)^2] - c [\det \Phi + \det \Phi^\dagger] - \text{Tr} [H(\Phi + \Phi^\dagger)] \right\}. \quad (\text{A.1})$$

The field Φ is a complex 2×2 matrix containing the scalar and pseudoscalar mesons,

$$\Phi = T_a (\sigma_a + i\pi_a), \quad (\text{A.2})$$

where the $N_f \times N_f$ matrices T_a are the generators of the group $U(2)$ such that $\text{Tr} (T_a T_b) = \delta_{ab}/2$. They fulfill the $U(N_f)$ algebra with the relations

$$[T_a, T_b] = if_{abc} T_c \quad (\text{A.3a})$$

$$\{T_a, T_b\} = d_{abc} T_c \quad (\text{A.3b})$$

¹The transition from MINKOWSKI to EUCLIDEAN spacetime is done via a WICK rotation $x^0 \rightarrow ix^4$ which yields an overall factor of i . The kinetic term of the field acquires a negative sign $\partial^0 \sigma_a \partial_0 \sigma_a \rightarrow -(\partial_4 \sigma_a)^2$ which matches with that of the potential. For brevity we omit the overall factor of $(-i)$.

where f_{abc} and d_{abc} are the antisymmetric and symmetric structure constants of $U(N_f)$. The indices are running from 0 to $N_f^2 - 1$. The generators and structure constants are identical to those of the group $SU(N_f)$ (in which all indices start from one), however for $U(N_f)$ there is in addition

$$T_0 = \frac{1}{\sqrt{2N_f}} \mathbf{1}, \quad f_{ab0} = 0, \quad d_{ab0} = \sqrt{\frac{2}{N_f}} \delta_{ab}. \quad (\text{A.3c})$$

In case of only two flavors (see Chapter 2) the structure constants reduce to

$$f_{ijk} = \varepsilon_{ijk} \quad \text{and} \quad d_{ijk} = 0 \quad \text{for} \quad i, j, k \in \{1, 2, 3\}, \quad (\text{A.4})$$

where ε_{ijk} is the totally antisymmetric LEVI-CIVITA symbol.

The two couplings λ_1 and λ_2 scale differently with the number of flavors N_f . To understand this we have a look at the classical action (A.1). The kinetic term $\text{Tr} \partial^\mu \Phi^\dagger \partial_\mu \Phi$ contains the trace $\text{Tr} T_a T_b = \delta_{ab}/2$ and two sums from 0 to $N_f^2 - 1$ which yields an overall factor of N_f^2 . So, all leading-order terms should scale with that factor; that is why the coupling λ_1 is divided by N_f^2 . The trace of all sums of four generators can be expressed by products of two of the symmetric structure constants (d -symbols) which results in a factor of $1/N_f$ and two KRONECKER symbols.

According to our considerations in Section 2 we define the vacuum expectation value

$$\langle \Phi \rangle = T_a \phi_a$$

with a real-valued condensate ϕ_a [cf. Eq. (2.6)] and shift the (complex) $U(2)_L \times U(2)_R$ fields to

$$\Phi(x) = T_a \phi_a + T_a [\sigma_a(x) + i\pi_a(x)],$$

where σ_a and π_a are real and symbolize the scalar and pseudoscalar meson fields. The shifted LAGRANGEAN (in EUCLIDEAN spacetime) is a sum of four parts

$$\mathcal{L}[\Phi] = V_{\text{class}}(\phi_0) + \mathcal{L}_2[\Phi] + \mathcal{L}_3[\Phi] + \mathcal{L}_4[\Phi]. \quad (\text{A.5})$$

The term linear in the fields is left out because the vacuum expectation value is considered to fulfill the classical EULER-LAGRANGE equation of motion

$$\delta \mathcal{S}[\Phi] \Big|_{\Phi = \langle \Phi \rangle} = 0.$$

Following CORNWALL *et al.* (1974) the 2PI effective action is a functional of the single-field expectation value ϕ and the *bilocal* composite operators (GREEN functions)

$$G_{ab}^S(x, y) = \langle \sigma_a(x) \sigma_b(y) \rangle \quad \text{and} \quad G_{ab}^P(x, y) = \langle \pi_a(x) \pi_b(y) \rangle. \quad (\text{A.6})$$

It is defined by a double LEGENDRE transform of SCHWINGER's generating functional in the path integral formalism

$$\mathcal{W}[J, K] = -\ln \int \mathcal{D}\Phi \mathcal{D}\Phi^\dagger \exp \left\{ - \left[\mathcal{S}[\Phi] + J \cdot \Phi + \frac{1}{2} \Phi^\dagger \cdot \mathbf{K} \cdot \Phi \right] \right\}, \quad (\text{A.7})$$

where J and \mathbf{K} symbolize local and bilocal source terms that are appropriately convolved with the quantum fields. The derivatives with respect to the sources generate the expectation values

$$\left. \frac{\delta \mathcal{W}[J, \mathbf{K}]}{\delta J_a} \right|_{J, \mathbf{K}=0} = \phi_a \quad (\text{A.8a})$$

$$\left. \frac{\delta \mathcal{W}[J, \mathbf{K}]}{\delta K_{ab}(x, y)} \right|_{J, \mathbf{K}=0} = \frac{1}{2} \phi_a(x) \phi_b(y) + \frac{1}{2} G_{ab}(x, y). \quad (\text{A.8b})$$

The LEGENDRE transform

$$\Gamma[\mathbf{G}, \phi] = \mathcal{W}[J, \mathbf{K}] - J \cdot \Phi - \frac{1}{2} \Phi \cdot \mathbf{K} \cdot \Phi - \frac{1}{2} \mathbf{K} \cdot \mathbf{G} \quad (\text{A.9})$$

defines the effective action. Setting the sources to zero it fulfills the stationarity conditions

$$\delta \Gamma[\phi, \mathbf{G}] = 0 \quad \Rightarrow \quad \frac{\delta \Gamma[\phi, \mathbf{G}]}{\delta G_{ab}^{S,P}} = 0 \quad (\text{A.10a})$$

$$\text{and} \quad \frac{\delta \Gamma[\phi, \mathbf{G}]}{\delta \phi_a} = 0. \quad (\text{A.10b})$$

The effective action is the sum of the classical action evaluated for the condensate field and loop corrections

$$\Gamma[\mathbf{G}, \phi] = \mathcal{S}[\phi] + \Gamma_1[\mathbf{G}, \phi_0] + \Gamma_2[\mathbf{G}, \phi_0]. \quad (\text{A.11})$$

The classical part is equal to the tree-level potential

$$V_{\text{class}}(\phi) = \frac{1}{2} m^2 \phi_a^2 - 3 \mathcal{C}_{ab} \phi_a \phi_b + \frac{1}{3} \mathcal{F}_{abcd} \phi_a \phi_b \phi_c \phi_d - h_a \phi_a \quad (\text{A.12})$$

multiplied by an overall volume factor: $\mathcal{S}[\phi] = \int_x V_{\text{class}}(\phi)$. We take the structure of the mass matrix and interaction coefficients from RÖDER *et al.* (2003) and adapt

them to our $1/N_f$ counting

$$\mathcal{C}_{ab} = \frac{c}{6} (\delta_{a0}\delta_{b0} - \delta_{a1}\delta_{b1} - \delta_{a2}\delta_{b2} - \delta_{a3}\delta_{b3}) \quad (\text{A.13a})$$

$$\begin{aligned} \mathcal{F}_{abcd} &= \frac{\lambda_1}{4 N_f^2} (\delta_{ab}\delta_{cd} + \delta_{ad}\delta_{bc} + \delta_{ac}\delta_{bd}) \\ &+ \frac{\lambda_2}{8 N_f} (d_{abn}d_{ncd} + d_{adn}d_{nbc} + d_{acn}d_{nbd}) \end{aligned} \quad (\text{A.13b})$$

$$\mathcal{H}_{abcd} = \frac{\lambda_1}{4 N_f^2} \delta_{ab}\delta_{cd} + \frac{\lambda_2}{8 N_f} (d_{abn}d_{ncd} + f_{acn}f_{nbd} + f_{bcn}f_{nad}) . \quad (\text{A.13c})$$

With the expectation value pointing only in the 0-direction,

$$\langle \Phi \rangle = T_a \phi_a = N_f T_0 \phi_0 \delta_{a0} = N_f T_0 \langle \sigma_0 \rangle = \sqrt{\frac{N_f}{2}} \mathbf{1} \phi_0 , \quad (\text{A.14})$$

the classical potential reduces to the expression [cf. (2.12)]

$$V_{\text{cl}}(\phi_0) = \frac{N_f^2}{2} (m^2 - c) \phi_0^2 + N_f^2 \frac{\lambda_1 + \lambda_2}{4} \phi_0^4 - N_f^2 h_0 \phi_0 . \quad (\text{A.15})$$

The second part of the shifted LAGRANGEan (A.5) consists of all terms bilinear in the fields

$$\begin{aligned} \mathcal{L}_2[\phi_a; \sigma_a, \pi_a] &= \frac{1}{2} (\partial_\mu \sigma_a)^2 - \frac{1}{2} [m^2 \delta_{ab} - 6 \mathcal{G}_{ab} + 4 \mathcal{F}_{abcd} \phi_c \phi_d] \sigma_a \sigma_b \\ &+ \frac{1}{2} (\partial_\mu \pi_a)^2 - \frac{1}{2} [m^2 \delta_{ab} + 6 \mathcal{G}_{ab} + 4 \mathcal{H}_{abcd} \phi_c \phi_d] \pi_a \pi_b . \end{aligned} \quad (\text{A.16})$$

In order to write down the 2PI effective action we need eigenvalues of the matrix of tree-level propagators which are the second derivatives of the LAGRANGEan density with respect to all fields

$$(\mathcal{D}_{ab}^S)^{-1} = \frac{\delta^2 \mathcal{L}}{\delta \sigma_a \delta \sigma_b} \Big|_{\Phi=\langle \Phi \rangle} \quad \text{and} \quad (\mathcal{D}_{ab}^P)^{-1} = \frac{\delta^2 \mathcal{L}}{\delta \pi_a \delta \pi_b} \Big|_{\Phi=\langle \Phi \rangle} .$$

These derivatives can be directly read off from Eq. (A.16). With the specific choice (A.14) of the expectation value the masses of all particles of the same isospin triplet are identical because only the generator T_0 is broken but not T_3 . Applying this to the usual identification of physical bosons ² for $N_f = 2$ (see *e.g.* RÖDER

²They are obtained by a superposition of right- and left-handed fields: scalar = right + left and pseudoscalar = right – left.

et al., 2003)

$$\Phi = \frac{1}{\sqrt{2}} \begin{pmatrix} \frac{1}{\sqrt{2}}(\sigma + a_0^0) & a_0^+ \\ a_0^- & \frac{1}{\sqrt{2}}(\sigma - a_0^0) \end{pmatrix} + \frac{i}{\sqrt{2}} \begin{pmatrix} \frac{1}{\sqrt{2}}(\eta + \pi^0) & \pi^+ \\ \pi^- & \frac{1}{\sqrt{2}}(\eta - \pi^0) \end{pmatrix}, \quad (\text{A.17})$$

we conclude

$$\sigma \equiv \sigma_0 \quad a_0 = \sigma_1 = \sigma_2 = \sigma_3 \quad (\text{A.18})$$

$$\eta \equiv \pi_0 \quad \pi = \pi_1 = \pi_2 = \pi_3. \quad (\text{A.19})$$

Furthermore, the matrix of classical propagators is diagonal with the eigenvalues

$$\mathcal{D}_\sigma^{-1}(\phi_0) = \partial^2 + m^2 - c - 3(\lambda_1 + \lambda_2)\phi_0^2 \quad (\text{A.20a})$$

$$\mathcal{D}_\pi^{-1}(\phi_0) = \partial^2 + m^2 - c - (\lambda_1 + \lambda_2)\phi_0^2 \quad (\text{A.20b})$$

$$\mathcal{D}_\eta^{-1}(\phi_0) = \partial^2 + m^2 + c - (\lambda_1 + \lambda_2)\phi_0^2 \quad (\text{A.20c})$$

$$\mathcal{D}_{a_0}^{-1}(\phi_0) = \partial^2 + m^2 + c - (\lambda_1 + 3\lambda_2)\phi_0^2. \quad (\text{A.20d})$$

We can diagonalize the matrix of GREEN functions (A.6) as well which allows for a straightforward $1/N_f$ counting. Using the physical identification of the meson fields as given in Eq. (A.17) we declare

$$G_\sigma \equiv G_{00}^S \quad G_\eta \equiv G_{00}^P \quad (\text{A.21a})$$

$$G_{a_0} \equiv G_{11}^S = G_{22}^S = G_{33}^S \quad G_\pi \equiv G_{11}^P = G_{22}^P = G_{33}^P. \quad (\text{A.21b})$$

With that knowledge we turn to the one-loop part of the 2PI effective action and obtain

$$\begin{aligned} \Gamma_1[G, \phi_0] &= \frac{1}{2} \text{Tr} \mathcal{D}^{-1} \mathbf{G} + \frac{1}{2} \ln \det \mathbf{G}^{-1} \\ &= \frac{1}{2} [\mathcal{D}_\sigma^{-1} G_\sigma + \mathcal{D}_\eta^{-1} G_\eta] + \frac{N_f^2 - 1}{2} [\mathcal{D}_{a_0}^{-1} G_{a_0} + \mathcal{D}_\pi^{-1} G_\pi] \\ &\quad + \frac{1}{2} [\ln \det G_\sigma^{-1} + \ln \det G_\eta^{-1}] + \frac{N_f^2 - 1}{2} [\ln \det G_{a_0}^{-1} + \ln \det G_\pi^{-1}]. \end{aligned} \quad (\text{A.22})$$

The expectation value of the four-vertex part of the shifted LAGRANGIAN

$$\mathcal{L}_4[\sigma_a, \pi_a] = -2 \mathcal{H}_{abcd} \sigma_a \sigma_b \pi_c \pi_d - \frac{1}{3} \mathcal{F}_{abcd} (\sigma_a \sigma_b \sigma_c \sigma_d + \pi_a \pi_b \pi_c \pi_d) \quad (\text{A.23})$$

yields all double-bubble terms

$$\Gamma_2^{\text{db}}(\mathbf{G}) = \left\langle \int_x \mathcal{L}_4(x) \right\rangle_{2\text{PI}} = \int_x 2 \mathcal{H}_{abcd} \Delta_{ab}^S \Delta_{cd}^P + \mathcal{F}_{abcd} (\Delta_{ab}^S \Delta_{cd}^S + \Delta_{ab}^P \Delta_{cd}^P),$$

where $\Delta_{ab} = \int_p G_{ab}(p)$ denotes single bubble graphs. Contracting all indices and disentangling orders of $1/N_f$ we find

$$\begin{aligned} \Gamma_{\text{db}}^{\text{LO}}(\mathbf{G}) = & \frac{(\lambda_1 + \lambda_2)}{4 N_f^2} \int_x \left\{ [\Delta_\sigma + (N_f^2 - 1) \Delta_\pi]^2 + [\Delta_\eta + (N_f^2 - 1) \Delta_{a_0}]^2 \right. \\ & \left. + 2 [\Delta_\sigma + (N_f^2 - 1) \Delta_\pi] [\Delta_\eta + (N_f^2 - 1) \Delta_{a_0}] \right\} \end{aligned} \quad (\text{A.24a})$$

$$\begin{aligned} \Gamma_{\text{db}}^{\text{NLO}}(\mathbf{G}) = & \frac{\lambda_1 + \lambda_2}{2 N_f^2} \int_x [(\Delta_\sigma^2 + \Delta_\eta^2) + (N_f^2 - 1) (\Delta_\pi^2 + \Delta_{a_0}^2)] \\ & + \frac{3}{2} \frac{\lambda_2}{N_f^2} \int_x [\Delta_\sigma^2 + \Delta_\eta^2 + (N_f^2 - 1) (\Delta_\sigma \Delta_{a_0} + \Delta_\eta \Delta_\pi)] \\ & + 3 \frac{\lambda_2}{N_f^2} \int_x [\Delta_\sigma \Delta_\eta + (N_f^2 - 1) \Delta_\sigma \Delta_\pi] \\ & + \frac{1}{2} \frac{\lambda_2}{N_f^2} \int_x (N_f^2 - 1) \Delta_{a_0} \Delta_\pi \end{aligned} \quad (\text{A.24b})$$

$$\Gamma_{\text{db}}^{\text{NNLO}}(\mathbf{G}) = 3 \frac{\lambda}{N_f^2} \int_x [\Delta_\sigma + \Delta_\eta]^2 \quad (\text{A.24c})$$

The leading-order part remarkably preserves a $U(2)_V \times U(2)_A$ symmetry. The first line of $\Gamma_{\text{db}}^{\text{NLO}}$ contains the “usual” term from a “flavor-exchanging” vertex (see Appendix C for more details) while the other terms arise from the group structure of $U(2) \times U(2)$ and cannot be “elaborately guessed” by looking at the $O(N)$ model.

The equations of motions are given by the stationarity conditions

$$\delta\Gamma[\phi_0, \mathbf{G}] = 0 \quad \Rightarrow \quad \frac{\delta\Gamma[\phi_0, \mathbf{G}]}{\delta G_{ab}^{S,P}} = 0, \quad \frac{\delta\Gamma[\phi_0, \mathbf{G}]}{\delta\phi_0} = 0. \quad (\text{A.25})$$

If Γ_2 only consists of double-bubble terms we can use a local *ansatz* for the GREEN functions

$$G_*(p) = \frac{1}{p^2 + M_*^2}. \quad (\text{A.26})$$

At leading order the effective action is only the sum $\Gamma = \Gamma_1 + \Gamma_{\text{db}}^{\text{LO}}$ so that the stationarity condition for the GREEN functions finally leads to the mass gap equations

$$M_\sigma^2 = m^2 - c + 3(\lambda_1 + \lambda_2)\phi_0^2 + \frac{(\lambda_1 + \lambda_2)}{N_f^2} \text{Tr } \Delta \quad (\text{A.27a})$$

$$M_\pi^2 = m^2 - c + (\lambda_1 + \lambda_2)\phi_0^2 + \frac{(\lambda_1 + \lambda_2)}{N_f^2} \text{Tr } \Delta \quad (\text{A.27b})$$

$$M_\eta^2 = m^2 + c + (\lambda_1 + \lambda_2)\phi_0^2 + \frac{(\lambda_1 + \lambda_2)}{N_f^2} \text{Tr } \Delta \quad (\text{A.27c})$$

$$M_{a_0}^2 = m^2 + c + (\lambda_1 + 3\lambda_2)\phi_0^2 + \frac{(\lambda_1 + \lambda_2)}{N_f^2} \text{Tr } \Delta . \quad (\text{A.27d})$$

The trace is defined as

$$\text{Tr } \Delta = \sum_a (\Delta_{aa}^S + \Delta_{aa}^P) = \Delta_\sigma + \Delta_\eta + (N_f^2 - 1)(\Delta_{a_0} + \Delta_\pi) .$$

All four masses only differ by constants or ϕ_0^2 -terms so that, effectively, only one gap equation must be solved

$$M_\sigma^2 = m^2 - c + 3(\lambda_1 + \lambda_2)\phi_0^2 + \frac{(\lambda_1 + \lambda_2)}{N_f^2} \text{Tr } \Delta \quad (\text{A.28a})$$

$$M_\pi^2 = M_\sigma^2 - 2(\lambda_1 + \lambda_2)\phi_0^2 \quad (\text{A.28b})$$

$$M_\eta^2 = M_\sigma^2 + 2c - 2(\lambda_1 + \lambda_2)\phi_0^2 \quad (\text{A.28c})$$

$$M_{a_0}^2 = M_\sigma^2 + 2c - 2\lambda_1\phi_0^2 . \quad (\text{A.28d})$$

We continue to work with the local GREEN functions and will compute all higher graphs with the leading-order masses.³ We restrain from deriving DYSON-SCHWINGER equations from NLO graphs since this would result in 1PI graphs of arbitrarily high order of $1/N_f$ (see Section C.4.3 of Appendix C for more details). The first iteration of the NLO DYSON-SCHWINGER equations may produce 1PI graphs of NLO that are not taken into account otherwise, but it would also violate the $U(1)_A$ symmetry in the DYSON-SCHWINGER equations, so that at finite temperature $M_\pi \neq M_\eta$ even for $c = 0$ (see MICHALSKI, 2006; RÖDER *et al.*, 2003, for such a phenomenon).

The third part of Eq. (A.5) contains trilinear terms describing the three-particle vertex (RÖDER *et al.*, 2003)

$$\mathcal{L}_3[\phi_a; \sigma_a, \pi_a] = -\frac{4}{3} \mathcal{F}_{abcd} \phi_d \sigma_a \sigma_b \sigma_c - 4 \mathcal{H}_{abcd} \phi_d \pi_a \pi_b \sigma_c . \quad (\text{A.29})$$

³To that extent, we would not have had to calculate double bubble graphs beyond leading order.

The sunset contributions to the effective potential are constructed by computing the expectation value

$$V_{\text{sunset}}(M^2, \phi_0) = -\frac{1}{2!} \left\langle \int_x \int_y \mathcal{L}_3(x) \mathcal{L}_3(y) \right\rangle_{2\text{PI}} \quad (\text{A.30})$$

where we chose to work in EUCLIDEAN spacetime and neglected an overall volume factor on the left hand side. The subscript 2PI means that only two-particle irreducible graphs may be constructed from this expectation value resulting in sunset graphs with three propagators from the vertex at x to the vertex at y as required by WICK's theorem. Note that since there is no tree-level mixing of masses, valid contractions are only of the type

$$\langle \sigma_a(x) \sigma_a(y) \rangle \longrightarrow G_{\sigma_a} \quad \text{or} \quad \langle \pi_a(x) \pi_a(y) \rangle \longrightarrow G_{\pi_a} , \quad (\text{A.31})$$

where $\sigma_0 = \sigma$, $\sigma_{1,2,3} = a_0$ and $\pi_0 = \eta$, $\pi_{1,2,3} = \pi$. For each contraction we have to consider its order in a $1/N_f$ expansion. At NLO we find the following sunset contribution to the effective potential

$$\begin{aligned} V_{\text{sunset}}^{\text{NLO}}(M^2, \phi_0) = -\phi_0^2 \left\{ \frac{(\lambda_1 + 3\lambda_2)^2}{N_f^2} [S_{\sigma\sigma\sigma} + (N_f^2 - 1) S_{\sigma a_0 a_0}] \right. \\ + \frac{(\lambda_1 + \lambda_2)^2}{N_f^2} [S_{\sigma\eta\eta} + (N_f^2 - 1) S_{\sigma\pi\pi}] \\ \left. + \frac{\lambda_2^2}{N_f^2} [S_{\eta\eta\sigma} + (N_f^2 - 1) S_{\eta\pi a_0}] \right\} , \end{aligned} \quad (\text{A.32})$$

where S_{ijk} denotes a sunset graph with propagators of the particles i , j and k . Note, that a “naïve” contraction of

$$\frac{1}{2} \left\langle (\mathcal{F}_{0bcd} \phi_0 \sigma_b \sigma_c \sigma_d)^2 \right\rangle_{2\text{PI}}$$

yields a prefactor of 3 for the $S_{\sigma\sigma\sigma}$ term, because if $b = c = d = 0$ there are six possible contractions to form a sunset graph. But in a $1/N_f$ expansion one of the three indices is zero due to flavor conservation at the vertex, so that the remaining contraction is given by

$$\frac{1}{2} \left\langle \mathcal{F}_{00cd} \phi_0 \sigma_0 \sigma_c \sigma_d \mathcal{F}_{00c'd'} \phi_0 \sigma_0 \sigma_{c'} \sigma_{d'} \right\rangle .$$

The only choice we have here is to contract c with c' and d with d' or *vice versa* to produce terms of an overall order N_f^0 . These contractions do include a term where all indices are zero but with a combinatoric factor of one.

From the stationarity conditions we find the equation of motion for the condensate

$$h_0 = \left[M_\pi^2 + 2 \frac{\lambda_1 + \lambda_2}{N_f^2} \Delta_\sigma + 2 \frac{\lambda_2}{N_f^2} (N_f^2 - 1) \Delta_{a_0} \right] \phi_0 + \frac{\partial}{\partial \phi_0} V_{\text{sunsets}}^{\text{NLO}}(\phi_0, M_{\text{LO}}^2), \quad (\text{A.33})$$

where we have used the leading-order solution M_π^2 from Eqs. (A.27). Note that in the chosen approximation the masses are determined at leading order while the condensate gets corrections from NLO.

Appendix B

Computation of the sunset graph

B.1 Sunset graph at zero temperature

The typical sunset graph in the effective action is given by the integral

$$\Gamma_{\text{sunset}} = i\phi_0^2\lambda^2 \int \frac{d^4p}{(2\pi)^4} \int \frac{d^4q}{(2\pi)^4} \frac{i}{p^2 - M_i^2} \frac{i}{q^2 - M_j^2} \frac{i}{(p+q)^2 - M_k^2}.$$

A WICK rotation yields a factor of $i^2(-1)^3$ so that eventually we obtain

$$\phi_0^2\lambda^2 \int \frac{d^4p}{(2\pi)^4} \int \frac{d^4q}{(2\pi)^4} \frac{1}{p^2 + M_i^2} \frac{1}{q^2 + M_j^2} \frac{1}{(p+q)^2 + M_k^2}, \quad (\text{B.1})$$

We use dimensional regularization and introduce the required mass scale μ_R according to the $\overline{\text{MS}}$ renormalization scheme

$$\mu_R = \frac{\bar{\mu}_R}{4\pi e^{-\gamma_E}}. \quad (\text{B.2})$$

Like VAN DER BIJ and VELTMAN (1984) we define a general sunset integral with three different propagators

$$(M_{11}, M_{12}, \dots, M_{1n} | M_{21}, \dots, M_{2n} | M_{31}, \dots, M_{3n}) \equiv \left(\frac{\bar{\mu}_R^2}{4\pi e^{-\gamma_E}} \right)^{4-n} \int \frac{d^n p}{(2\pi)^n} \int \frac{d^n q}{(2\pi)^n} \prod_{i=1}^{n_1} \frac{1}{[p^2 + M_{1i}^2]} \prod_{j=1}^{n_2} \frac{1}{[q^2 + M_{2j}^2]} \prod_{k=1}^{n_3} \frac{1}{[(p+q)^2 + M_{3k}^2]}, \quad (\text{B.3})$$

where n is the number of space time dimensions. With the identity (VAN DER BIJ and VELTMAN, 1984)

$$(M_0|M_1|M_2) = \frac{1}{3-n} \left\{ M_0^2(M_0M_0|M_1|M_2) + M_1^2(M_1M_1|M_0|M_2) + M_2^2(M_2M_2|M_0|M_1) \right\}, \quad (\text{B.4})$$

the sunset graph is reduced to a function of mass dimension zero that can be expanded in $n = 4 - \epsilon$ dimensions — correcting a sign error of VAN DER BIJ and VELTMAN (1984) —

$$(M, M|M_1|M_2) = \frac{1}{(4\pi)^4} \left[\frac{2}{\epsilon^2} + \frac{2}{\epsilon} \left(\frac{1}{2} - \ln \frac{M^2}{\bar{\mu}_R^2} \right) + \frac{1}{2} + \frac{\pi^2}{12} + \left(-\ln \frac{M^2}{\bar{\mu}_R^2} \right)^2 - \ln \frac{M^2}{\bar{\mu}_R^2} + f(a, b) \right] + \mathcal{O}(\epsilon) \quad (\text{B.5})$$

and

$$\frac{1}{3-n} (M, M|M_1|M_2) = \frac{1}{(4\pi)^4} \left[-\frac{2}{\epsilon^2} - \frac{2}{\epsilon} \left(\frac{3}{2} - \ln \frac{M^2}{\bar{\mu}_R^2} \right) - \frac{7}{2} - \frac{\pi^2}{12} - \left(-\ln \frac{M^2}{\bar{\mu}_R^2} \right)^2 - \left(-\ln \frac{M^2}{\bar{\mu}_R^2} \right) - f(a, b) \right] + \mathcal{O}(\epsilon). \quad (\text{B.6})$$

The function $f(a, b)$ contains an integration over a FEYNMAN parameter

$$f(a, b) = \int_0^1 dx \left(\text{Sp}(1 - \mu^2) - \frac{\mu^2 \ln \mu^2}{1 - \mu^2} \right), \quad (\text{B.7})$$

where

$$\mu^2 = \frac{ax + b(1-x)}{x(1-x)}, \quad a = \frac{M_1^2}{M^2}, \quad b = \frac{M_2^2}{M^2}$$

and $\text{Sp}(x)$ is SPENCE's integral (or the dilogarithm)

$$\text{Sp}(x) = - \int_0^x dt \frac{\ln(1-t)}{t}. \quad (\text{B.8})$$

This function fulfills the following identities

$$\text{Sp}(1-x) = -\text{Sp}(x) - \ln x \ln(1-x) + \frac{\pi^2}{6} \quad (\text{B.9a})$$

$$\text{Sp}\left(\frac{1}{x}\right) = -\text{Sp}(x) - \frac{1}{2} \ln^2(-x) - \frac{\pi^2}{6}. \quad (\text{B.9b})$$

Performing the remaining parameter integration over x the function $f(a, b)$ simplifies to

$$f(a, b) = -\frac{1}{2} \ln a \ln b - \left(\frac{a+b-1}{\sqrt{\Delta}} \right) \left[\text{Sp} \left(\frac{-x_2}{y_1} \right) + \text{Sp} \left(\frac{-y_2}{x_1} \right) + \frac{1}{4} \ln^2 \frac{x_2}{y_1} + \frac{1}{4} \ln^2 \frac{y_2}{x_1} + \frac{1}{4} \ln^2 \frac{x_1}{y_1} - \frac{1}{4} \ln^2 \frac{x_2}{y_2} + \zeta(2) \right], \quad (\text{B.10})$$

with

$$\Delta = 1 - 2(a+b) + (a-b)^2, \quad x_{1,2} = \frac{1}{2} \left(1 + b - a \pm \sqrt{\Delta} \right), \quad y_{1,2} = \frac{1}{2} \left(1 + a - b \pm \sqrt{\Delta} \right) \quad (\text{B.11})$$

and ζ is RIEMANN'S zeta function or explicitly $\zeta(2) = \frac{\pi^2}{6}$.

B.2 Sunset graph at finite temperature

We use the MATSUBARA formalism to evaluate the sunset graph at finite temperature. At a temperature $T = 1/\beta$ it reads

$$(m_i | m_j | m_k)_\beta = \left(\frac{\bar{\mu}_R^2}{4\pi e^{-\gamma_E}} \right)^{4-n} T^3 \sum_{n_i, n_j, n_k} \int \frac{d^{n-1} p_i}{(2\pi)^{n-1}} \frac{d^{n-1} p_j}{(2\pi)^{n-1}} \frac{d^{n-1} p_k}{(2\pi)^{n-1}} (2\pi)^{n-1} \times \delta(\mathbf{p}_i + \mathbf{p}_j + \mathbf{p}_k) \beta \delta_{n_i+n_j, n_k} \frac{1}{p_i^2 + m_i^2} \frac{1}{p_j^2 + m_j^2} \frac{1}{p_k^2 + m_k^2} \quad (\text{B.12})$$

where the zero component of each momentum p_i is a discrete MATSUBARA frequency

$$p_i^0 = 2\pi n_i T.$$

The so-called *Saclay method* (PISARSKI, 1988) suggests a partial FOURIER transform of the propagator

$$\frac{1}{p + m_i^2} = \int_0^\beta d\tau e^{ip^0\tau} \Delta_i(\tau, \mathbf{p}) \quad \text{with} \quad p^0 = 2\pi T n_i, \quad (\text{B.13})$$

with

$$\begin{aligned}\Delta_i(\tau, \mathbf{p}) &= \frac{1}{2E_i(\mathbf{p})} \{ [1 + n(\mathbf{p})] e^{-E_i(\mathbf{p})\tau} + n(\mathbf{p}) e^{+E_i(\mathbf{p})\tau} \} \\ n_i(\mathbf{p}) &= \frac{1}{e^{\beta E_i(\mathbf{p})} - 1} \\ E_i(\mathbf{p}) &= \sqrt{\mathbf{p}^2 + m_i^2} .\end{aligned}$$

We substitute this into the expression for the thermal sunset (B.12). At first, we sum over n_3 , which makes the KRONECKER delta $\delta_{n_1+n_2, n_3}$ vanish. The remaining summations over exponentials yield $\beta \delta(\tau_2 + \tau_3)$ and then $\beta \delta(\tau_1 - \tau_2)$, so that finally we have traded three MATSUBARA summations in Eq. (B.12) for a single integration over τ

$$\begin{aligned}(m_i | m_j | m_k)_\beta &= \int_0^\beta d\tau \left(\frac{\bar{\mu}_R^2}{4\pi e^{-\gamma E}} \right)^{4-n} \int \frac{d^{n-1}p_i}{(2\pi)^{n-1}} \frac{d^{n-1}p_j}{(2\pi)^{n-1}} \frac{d^{n-1}p_k}{(2\pi)^{n-1}} (2\pi)^{n-1} \\ &\quad \times \delta(\mathbf{p}_i + \mathbf{p}_j + \mathbf{p}_k) \Delta_i(\tau, \mathbf{p}_i) \Delta_j(\tau, \mathbf{p}_j) \Delta_k(\tau, \mathbf{p}_k) .\end{aligned}\quad (\text{B.14})$$

To write the result (B.14) in a short form we define

$$S(E_i, E_j, E_k) := \frac{1}{E_i + E_j + E_k} \quad \text{with} \quad E_\ell = \sqrt{\mathbf{p}_\ell^2 + m_\ell^2}, \quad \ell = i, j, k ,$$

which can be used to express the outcome of the integration

$$\begin{aligned}
 \int_0^\beta d\tau \Delta_i \Delta_j \Delta_k = \frac{1}{4E_i E_j E_k} \left\{ S(E_i, E_j, E_k) + n_i \left[S(E_i, E_j, E_k) + S(-E_i, E_j, E_k) \right] \right. \\
 + n_j \left[S(E_i, E_j, E_k) + S(E_i, -E_j, E_k) \right] \\
 + n_k \left[S(E_i, E_j, E_k) + S(E_i, E_j, -E_k) \right] \\
 + n_i n_j \left[S(E_i, E_j, E_k) + S(-E_i, E_j, E_k) \right. \\
 \left. + S(E_i, -E_j, E_k) + S(-E_i, -E_j, E_k) \right] \\
 + n_i n_k \left[S(E_i, E_j, E_k) + S(-E_i, E_j, E_k) \right. \\
 \left. + S(E_i, E_j, -E_k) + S(-E_i, E_j, -E_k) \right] \\
 + n_j n_k \left[S(E_i, E_j, E_k) + S(E_i, -E_j, E_k) \right. \\
 \left. + S(E_i, E_j, -E_k) + S(E_i, -E_j, -E_k) \right] \left. \right\}. \tag{B.15}
 \end{aligned}$$

The first term corresponds to the result for $T = 0$. The remaining terms can be split into two parts

$$S_{(i)jk} = \left(\frac{\bar{\mu}_R^2}{4\pi e^{-\gamma E}} \right)^{4-n} \int \frac{d^{n-1}p_i}{(2\pi)^{n-1}} \frac{d^{n-1}p_j}{(2\pi)^{n-1}} \frac{n_i}{4E_i E_j E_k} \left[S(E_i, E_j, E_k) + S(-E_i, E_j, E_k) \right] \tag{B.16}$$

$$\begin{aligned}
 S_{(ij)k} = \left(\frac{\bar{\mu}_R^2}{4\pi e^{-\gamma E}} \right)^{4-n} \int \frac{d^{n-1}p_i}{(2\pi)^{n-1}} \frac{d^{n-1}p_j}{(2\pi)^{n-1}} \frac{n_i n_j}{4E_i E_j E_k} \left[S(E_i, E_j, E_k) + S(-E_i, E_j, E_k) \right. \\
 \left. + S(E_i, -E_j, E_k) + S(-E_i, -E_j, E_k) \right]. \tag{B.17}
 \end{aligned}$$

The integrand of Eq. (B.17) can be simplified so that

$$\begin{aligned}
 \frac{n_i n_j}{4E_i E_j E_k} \left[S(E_i, E_j, E_k) + S(-E_i, E_j, E_k) + S(E_i, -E_j, E_k) + S(-E_i, -E_j, E_k) \right] \\
 = \frac{n_i n_j}{4E_i E_j E_k} \left[\frac{-2E_k}{(E_i + E_j)^2 - E_k^2} + \frac{-2E_k}{(E_i - E_j)^2 - E_k^2} \right] \\
 = -\frac{n_i n_j}{2E_i E_j} \left[\frac{1}{(E_i + E_j)^2 - E_k^2} + \frac{1}{(E_i - E_j)^2 - E_k^2} \right].
 \end{aligned}$$

The \mathbf{p}_k integration in Eq. (B.14) replaces the δ -function by the condition

$$\mathbf{p}_k = \mathbf{p}_i + \mathbf{p}_j \quad \Rightarrow \quad E_k^2 = \mathbf{p}_i^2 + \mathbf{p}_j^2 + m_k^2 + 2p_i p_j \cos \theta .$$

The angular integration over θ can be performed using

$$\int_{-1}^1 \frac{d \cos \theta}{a \cos \theta + b} = \int_{-a}^a \frac{dz}{a} \frac{1}{z + b} = \frac{1}{a} \ln \left| \frac{b + a}{b - a} \right| .$$

Substituting this relation into Eq. (B.17) we find (for $n = 4$)

$$\begin{aligned} S_{(ij)k} &= \int \frac{d^3 p_i}{(2\pi)^3} \frac{d^3 p_j}{(2\pi)^3} \frac{-n_i n_j}{2E_i E_j} \left[\frac{1}{(E_i + E_j)^2 - E_k^2} + \frac{1}{(E_i - E_j)^2 - E_k^2} \right] \\ &= \frac{1}{8\pi^4} \int_0^\infty dp_i dp_j \frac{n_i n_j p_i p_j}{4E_i E_j} \ln \left| \frac{Y^+}{Y^-} \right| , \end{aligned} \quad (\text{B.18})$$

where

$$Y^\pm = [(E_i + E_j)^2 - (E_k^\pm)^2][(E_i - E_j)^2 - (E_k^\pm)^2]$$

and

$$E_k^\pm = \sqrt{(p_i \pm p_j)^2 + m_k^2} .$$

The p_j integral in Eq. (B.16) still contains divergences which can be read off an expansion for large E_j

$$\begin{aligned} S_{(i)jk} &= \left(\frac{\bar{\mu}_R^2}{4\pi e^{-\gamma_E}} \right)^{\epsilon/2} \int \frac{d^{3-\epsilon} p_i}{(2\pi)^{3-\epsilon}} \frac{n_i}{E_i} \int \frac{d^{3-\epsilon} p_j}{(2\pi)^{3-\epsilon}} \left\{ \frac{1}{4E_j^3} + O(E_j^{-5}) \right\} \\ &= \left(\frac{\bar{\mu}_R^2}{4\pi e^{-\gamma_E}} \right)^{\epsilon/2} \int \frac{d^{3-\epsilon} p_i}{(2\pi)^{3-\epsilon}} \frac{n_i}{E_i} \frac{1}{4(4\pi)^{\frac{3-\epsilon}{2}}} \frac{\Gamma(\frac{\epsilon}{2})}{\Gamma(\frac{3}{2})} + O(m_j^{-2}) \\ &= \left(\frac{\bar{\mu}_R^2}{4\pi e^{-\gamma_E}} \right)^{\epsilon/2} \int \frac{d^{n-1} p_i}{(2\pi)^{n-1}} \frac{n_i}{E_i} \frac{1}{4 \cdot 8\sqrt{\pi}^3 \cdot \frac{1}{2}\sqrt{\pi}} \Gamma\left(\frac{\epsilon}{2}\right) \left(\frac{4\pi}{m_j^2}\right)^{\epsilon/2} + O(m_j^{-2}) \\ &= \int \frac{d^{n-1} p_i}{(2\pi)^{n-1}} \frac{n_i}{E_i} \frac{1}{(4\pi)^2} \left(\frac{2}{\epsilon} - \ln \frac{m_j^2}{\bar{\mu}_R^2} + O(\epsilon) \right) + O(m_j^{-2}) . \end{aligned}$$

We decompose expression (B.16) into three parts

$$S_{(i)jk} = F_i^{(0)} + F_{(i)j}^{(1)} + F_{(i)jk}^{(2)} , \quad (\text{B.19})$$

defined as

$$F_i^{(0)} = \frac{I_\beta^\epsilon(m_i^2) 2}{(4\pi)^2 \epsilon} \quad (\text{B.20a})$$

$$F_{(i)j}^{(1)} = -\frac{I_\beta^{\epsilon \rightarrow 0}(m_i^2)}{(4\pi)^2} \ln \frac{m_j^2}{\bar{\mu}_R^2} \quad (\text{B.20b})$$

$$F_{(i)jk}^{(2)} = \frac{1}{2(2\pi)^4} \int_0^\infty dp_i \frac{p_i n_i}{E_i} \int_0^\infty dp_j \frac{p_j}{E_j} \left(\ln \left| \frac{X_k^+}{X_k^-} \right| - 2 \frac{p_i p_j}{E_j^2} \right), \quad (\text{B.20c})$$

where

$$X_k^\pm = [E_i + E_j + E_k^\pm] \cdot [-E_i + E_j + E_k^\pm]$$

and

$$\begin{aligned} I_\beta^\epsilon(m_i^2) &= \left(\frac{\bar{\mu}_R^2}{4\pi e^{-\gamma_E}} \right)^{\frac{4-n}{2}} \int \frac{d^{n-1}p_i}{(2\pi)^{n-1}} \frac{n_i(\mathbf{p}_i)}{E_i(\mathbf{p}_i)} \\ &= \left(\frac{1}{4\pi e^{-\gamma_E}} \right)^{\frac{\epsilon}{2}} \frac{1}{(2\pi)^{3-\epsilon}} \frac{2\pi^{\frac{3-\epsilon}{2}}}{\Gamma\left(\frac{3-\epsilon}{2}\right)} \int_0^\infty dp_i p_i^2 \left(\frac{p_i^2}{\bar{\mu}_R^2} \right)^{-\epsilon/2} \frac{n_i(p_i)}{E_i(p_i)} \\ &= \frac{1}{2\pi^2} \int_0^\infty dp_i p_i^2 \left[1 - \frac{\epsilon}{2} \left(\ln \frac{p_i^2}{\bar{\mu}_R^2} + 2 \ln 2 - 2 + \gamma_E \right) + \mathcal{O}(\epsilon^2) \right] \frac{n_i(p_i)}{E_i(p_i)}. \end{aligned}$$

Using all abbreviations defined within this section the sunset graph with three masses M_i , M_j and M_k at a temperature T reads

$$\begin{aligned} S_{ijk} &= (M_i|M_j|M_k) + S_{(i)jk} + S_{(j)ki} + S_{(k)ij} \\ &\quad + S_{(ij)k} + S_{(jk)i} + S_{(ki)j} \end{aligned} \quad (\text{B.21})$$

and can be numerically computed.

Appendix C

1/N expansion and resummation schemes

This chapter is meant to clarify all ambiguities that might arise when applying 1/N counting within different resummation schemes. It is necessary to go back to the level of one-particle irreducible graphs in the effective action in order to compare resummation schemes.

As an application of resummation we take a scalar Φ^4 model with $O(N)$ symmetry. The action functional is given by

$$\mathcal{S}[\Phi] = \int d^4x \mathcal{L}[\Phi] = \int d^4x \left[\frac{1}{2} (\partial_\mu \Phi_i)^2 - \frac{1}{2} m^2 \Phi_i^2 - \frac{\lambda}{4N} (\Phi_i^2)^2 \right]. \quad (\text{C.1})$$

We compute the effective action in terms of one-particle irreducible graphs and count their order of 1/N.

C.1 Counting 1PI graphs

Each component of the field Φ_i gets *the same* expectation value, so that the square of the field is of order N

$$\langle \Phi_i \rangle = \phi \quad \Rightarrow \quad \langle \Phi_i \rangle \langle \Phi_i \rangle = N \phi. \quad (\text{C.2})$$

Without loss of generality one could perform an $O(N)$ rotation and adjust the expectation value to one direction in

$$\langle \Phi_i \rangle = \delta_{1i} \sqrt{N} \phi. \quad (\text{C.3})$$

Propagators are local and diagonal

$$i\mathcal{D}_{ij}^{-1}[\phi; k] = (k^2 - m^2 - \lambda\phi^2) \delta_{ij} - 2\lambda\phi^2 \delta_{i1}\delta_{j1} \quad (\text{C.4})$$

which makes counting and computing rather simple.

C.1.1 Leading order

The classical part of the effective action scales with a factor N (we neglect an overall volume factor here)

$$\Gamma_{\text{cl}}[\phi] = -N \left[\frac{1}{2}m^2\phi^2 + \frac{\lambda}{4}\phi^4 \right]. \quad (\text{C.5})$$

It certainly belongs to the leading order in a $1/N$ expansion. So we have to look for all other vacuum graphs that are of order N . At one-loop level there is the logarithm of the functional determinant

$$\Gamma_1[\phi] = \frac{i}{2} \ln \det i\mathcal{D}^{-1}(\phi). \quad (\text{C.6})$$

This contributes at leading order since the matrix \mathcal{D}^{-1} has N eigenvalues.

There are also two-loop graphs that scale with a factor of N . Those are double bubble graphs without flavor exchange at the vertex [see Figure C.1(a)]. Each vertex yields a factor of $1/N$ because the coupling is λ/N and each closed line with the same index at both ends results in a factor of N . Consequently, a double bubble graph as in Figure C.1(a) is of leading order

$$\Gamma_{\text{db}}^{\text{LO}} = -\frac{\lambda}{4N} \sum_{ij} \Delta_{ii}\Delta_{jj} \sim \frac{1}{N} \sum_{ij} \delta_{ii} \delta_{jj} = \sum_i 1 = N \quad (\text{C.7})$$

and graphs like those in Figure C.1(b) are of next-to-leading order

$$\Gamma_{\text{db}}^{\text{NLO}} = -\frac{\lambda}{4N} \sum_{ij} \Delta_{ij}\Delta_{ij} \sim \frac{1}{N} \sum_{ij} \delta_{ij} \delta_{ij} = \frac{1}{N} \sum_i 1 = 1 = N^0. \quad (\text{C.8})$$

Let us have a look at multiloop (daisy) graphs shown in Figure C.2. In these graphs we find a resummation of one-loop propagator insertions without flavor exchange at the vertex. We determine one of these insertions into a propagator $\mathcal{D}_{ii'}$ as in Figure C.3(a). Such an insertion is diagonal and of the form

$$\Delta_{kk} \sim \frac{1}{N} \sum_j \delta_{jj} \sim 1. \quad (\text{C.9})$$

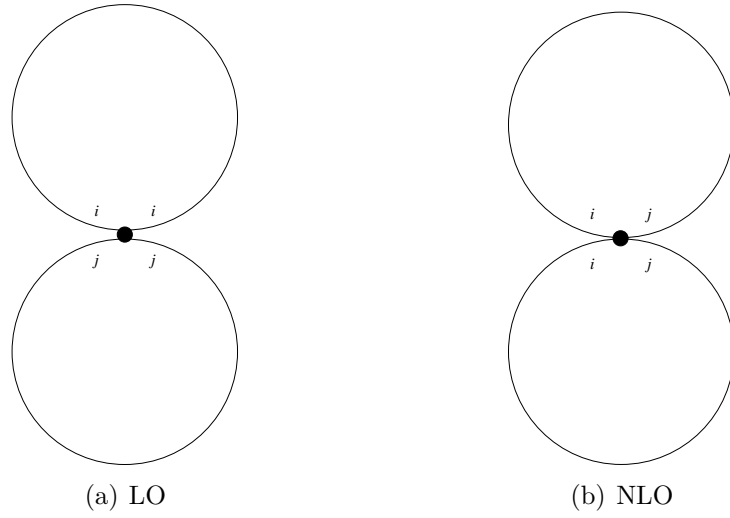


Figure C.1: The double bubble graph with a “diagonal” vertex without flavor exchange between both loops is of leading (LO) whereas the a “non-diagonal” vertex leads to a graph of next-to-leading order (NLO).

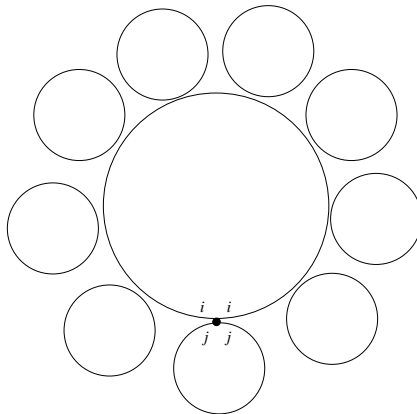


Figure C.2: Daisy graphs with “diagonal” vertices are of leading order.

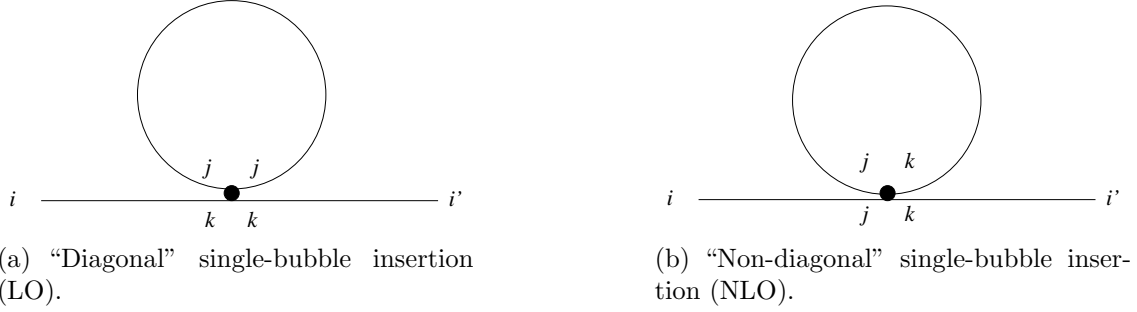


Figure C.3: Single-bubble insertions into a propagator $\mathcal{D}_{ii'}$ can be of leading (LO) or of next-to-leading order (NLO).

So, a propagator with one of these insertion scales like

$$\mathcal{D}_{ii'} \sim \sum_{jk} \delta_{ik} \left(\frac{1}{N} \delta_{jj} \right) \delta_{ki'} = \sum_k \delta_{ik} \delta_{ki'} = \delta_{ii'} \quad (\text{C.10})$$

and is of the same order as the propagator without an insertion. We conclude that a (diagonal) mass insertion like in Eq. (C.9) does not affect the order of the graph. Therefore, all super-daisy graphs consisting of diagonal bubble insertions are of leading order in the $1/N$ expansion.

In contrast to this, each mass insertion with a flavor-exchanging vertex [Figure C.3(b)] changes the order of a graph by $1/N$. A propagator with one of those insertions scales like

$$\mathcal{D}_{ii'} \sim \sum_{jk} \delta_{ik} \left(\frac{1}{N} \delta_{kj} \right) \delta_{ji'} = \frac{1}{N} \sum_k \delta_{ik} \delta_{ki'} = \frac{1}{N} \delta_{ii'} . \quad (\text{C.11})$$

One can imagine that another insertion of that type increases the order even more; n bubble insertions of NLO produce a propagator of $\mathcal{O}(N^{-n})$ or (next-to) n -leading order.

We can conclude that the leading order of a $1/N$ expansion of the effective action is proportional to N and consists of the classical action (C.5), the one-loop determinant (C.6) and all super-daisy graphs with vertices that keep the flavor inside the loops (Fig.C.2). To describe the resummation of such super-daisy graphs one can use gap equations for an effective mass matrix

$$M_{ij}^2(\phi) = (m^2 + \lambda\phi^2) \delta_{ij} + 2 \frac{\lambda}{N} \phi_i \phi_j + \frac{\lambda}{N} \sum_k \Delta_{kk} \quad (\text{C.12})$$

that is as diagonal as the propagator (C.4) if $\phi_i = \phi \delta_{i1}$ and is described by its two eigenvalues

$$M_\sigma^2(\phi) = m^2 + 3\lambda \phi^2 + \frac{\lambda}{N} [\Delta_\sigma + (N-1) \Delta_\pi] \quad (\text{C.13a})$$

$$M_\pi^2(\phi) = m^2 + \lambda \phi^2 + \frac{\lambda}{N} [\Delta_\sigma + (N-1) \Delta_\pi] , \quad (\text{C.13b})$$

where Δ_σ and Δ_π are diagonal single-bubble mass corrections and the propagator is given by the effective mass M_π or M_σ . Note that due to symmetry

$$M_\sigma^2(\phi) = M_\pi^2(\phi) + 2\lambda \phi^2 .$$

Both masses are functions of the vacuum expectation value and therefore become degenerate when $\phi = 0$ (no spontaneous symmetry breaking).

One could go even further and take the strict limit $N \rightarrow \infty$ in Eqs. (C.13) so that

$$M_\sigma^2(\phi) = m^2 + \lambda(3\phi^2 + \Delta_\pi) \quad (\text{C.14a})$$

$$M_\pi^2(\phi) = m^2 + \lambda(\phi^2 + \Delta_\pi) . \quad (\text{C.14b})$$

These equations occur in the 1PI effective action formalism with an auxiliary field introduced by ROOT (1974) which is discussed in Section C.3.

C.1.2 Next-to-leading order

In the previous section we have seen that each mass insertion with a flavor-exchanging vertex changes the order of a graph by a factor of $1/N$. One contribution to next-to-leading order (NLO) is therefore the double bubble graph with flavors passing from one bubble to the other [Figure C.1(b)]. The propagators in these graphs are to be described by the LO-resummed effective masses (C.13) and thus contain infinitely many *diagonal* insertions.

Let us have a look at the remaining graphs with two loops. Figure C.4 shows two possible sunset graphs whose order is

$$\text{Sunset}_{\text{NLO}} \sim \frac{1}{N^2} \sum_{ij'j'} \delta_{jj'} \delta_{jj'} \delta_{ii'} = \frac{1}{N^2} \sum_{ij} = 1 = N^0 = \text{NLO} \quad (\text{C.15a})$$

$$\text{Sunset}_{\text{NNLO}} \sim \frac{1}{N^2} \sum_{ij'j'} \delta_{j'i'} \delta_{jj'} \delta_{ij'} = \frac{1}{N^2} \sum_{ji} \delta_{ji} = N^{-1} = \text{NNLO} . \quad (\text{C.15b})$$

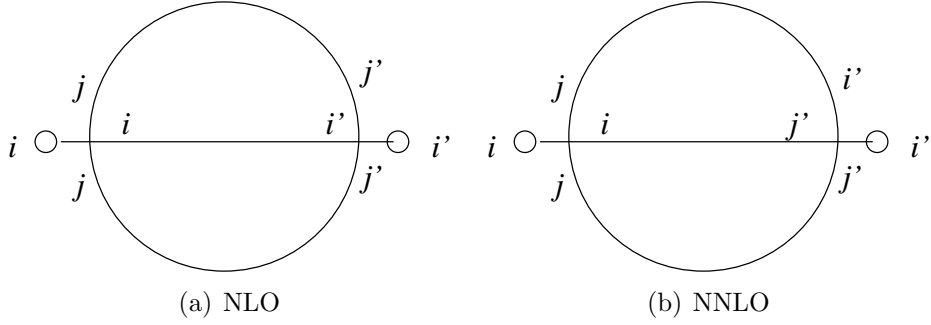


Figure C.4: Sunset graphs of next-to-leading and next-to-next-to-leading order

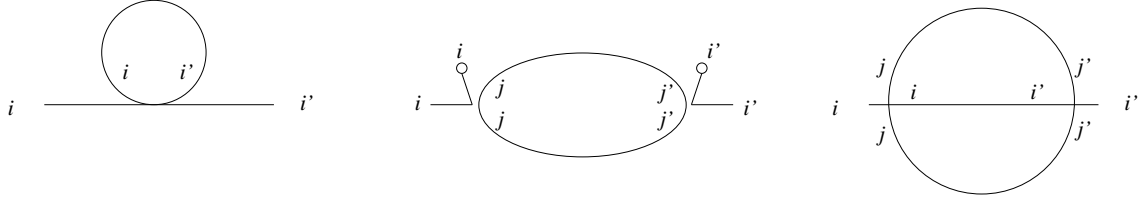


Figure C.5: Next-to-leading order corrections to the self-energy. Each vertex yields a factor of $1/N$ but all graphs contain loops with N flavors running around.

Here, we count each component of the condensate field $\langle \Phi_i \rangle = \phi$. One could also count each three-vertex like $\frac{\lambda}{N} \sqrt{N} \phi$ and require that one of the three indices equals one via an additional **KRONECKER** delta. One can consider both sunsets as LO one-loop graphs with fish graphs inserted. One of the two possible fish insertions (Fig. C.5) is proportional to $1/N$,

$$\mathcal{F}_{jj'}^{\text{NLO}} \sim \frac{1}{N^2} \sum_{ii'} \delta_{ii'} = \frac{1}{N} = \text{NLO} , \quad (\text{C.16a})$$

so that the sunset graph with this insertion is of NLO as well. The other fish insertion scales with $1/N^2$ and makes the respective sunset only contribute at NNLO

$$\mathcal{F}_{jj'}^{\text{NNLO}} \sim \frac{1}{N^2} \sum_{ii'} \delta_{ji'} \delta_{ij'} = \frac{1}{N^2} \sum_i \delta_{ij'} = \frac{1}{N^2} = \text{NNLO} . \quad (\text{C.16b})$$

Apart from the NLO fish and the single bubble with the non-diagonal vertex there is a sunset contribution to the self-energy as depicted in Fig. C.5. It scales like

$$\mathcal{S}_{ii'}^{\text{NLO}} \sim \frac{1}{N^2} \sum_{jj'} \delta_{jj'} \delta_{ii'} = \frac{1}{N} \delta_{ii'} . \quad (\text{C.17})$$

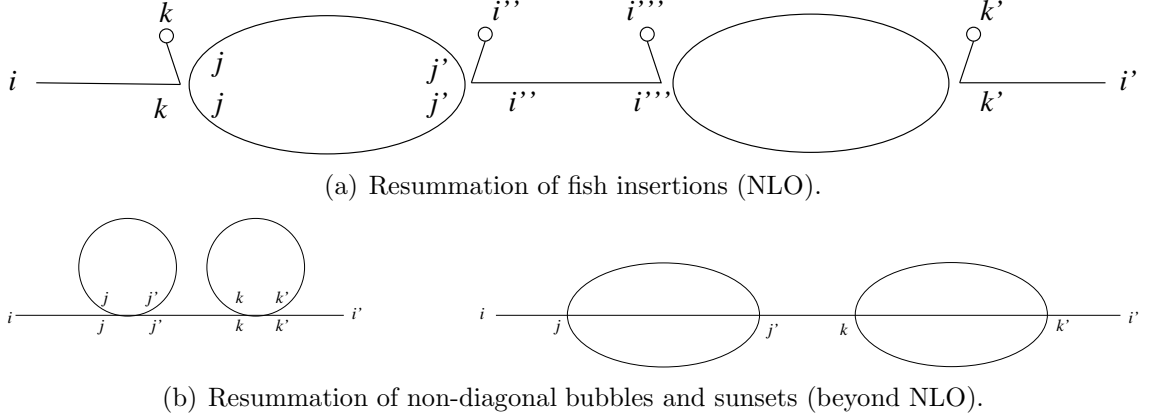


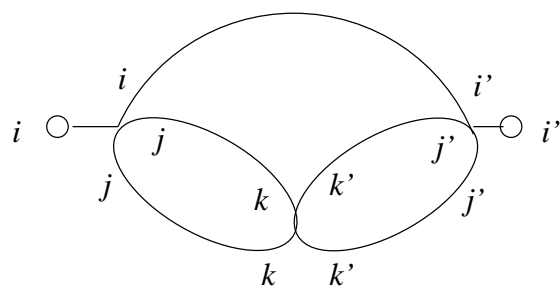
Figure C.6: Propagator with resummed NLO self-energy corrections. Although all self-energy contributions in Fig. C.5 are of NLO only the resummation of fish insertions leaves the order of the propagator unaffected.

It is instructive to study what happens to the order of the propagator when all self-energy contributions of Fig. C.5 are resummed via the standard definition of the propagator

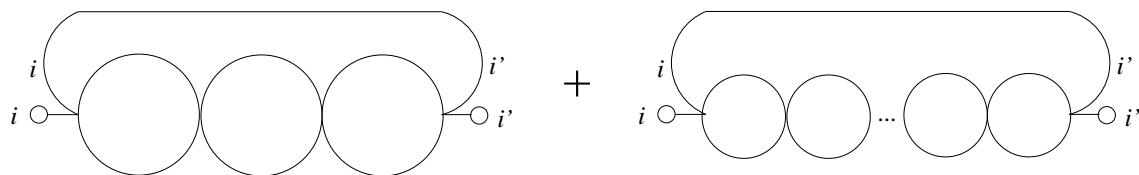
$$G(p) = \frac{i}{i\mathcal{D}^{-1} - \Sigma(p)} = \mathcal{D} \frac{1}{1 + i\Sigma\mathcal{D}} = \mathcal{D} - \mathcal{D}i\Sigma\mathcal{D} + \mathcal{D}i\Sigma\mathcal{D}i\Sigma\mathcal{D} \mp \dots \quad (\text{C.18})$$

For the sake of brevity the indices were left away here. A propagator with n NLO single-bubble and sunset insertions is $\mathcal{O}(N^{-n})$ which is (next-to) n -leading order. But a series of n NLO fish self-energies leaves the propagator at NLO (cf. Fig. C.6). So there is a way to modify the propagator using arbitrarily many insertions such that it stays of next-to-leading order. Figure C.7 depicts the way this can be done: Take the NLO sunset graph [Fig. C.4(a)] and cut both lines labelled with j and j' . Then connect the two open legs labelled j' of the right hand vertex in Fig. C.4(a) to form a loop with inner indices j' and k' . The additional vertex yields a factor of $1/N$ but the summation over j' and k' results in an overall factor of N^0 for the modified vertex. So, a sunset with two bubbles at the bottom [Fig. C.7(a)] is of next-to-leading order as well. Since one vertex modification does not change the order of the graph, two and more will neither do so, *i.e.*, all bubble-chain sunsets [Figure C.7(b)] are to be taken into account at NLO as well.

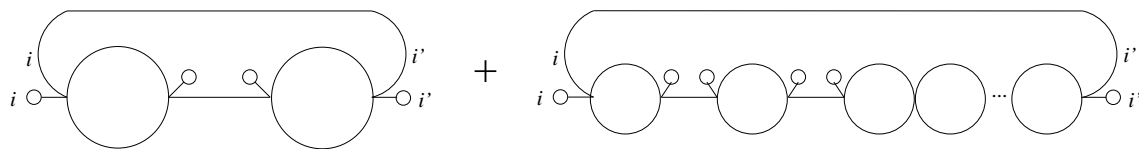
Let us have a look at a chain of at least three bubbles in Fig. C.7(b). We cut one of the propagators of one of the inner bubbles and pin its two endpoints to the background field ϕ and obtain the graphs of Fig. C.7(c). The contribution from the cut bubble is still of $\mathcal{O}(N)$ when counting because there are N background fields



(a) Three-loop sunset



(b) Higher-loop sunsets



(c) Higher-loop sunsets with σ line and background field insertions.

Figure C.7: Multi-loop sunset-type graphs contributing at NLO.

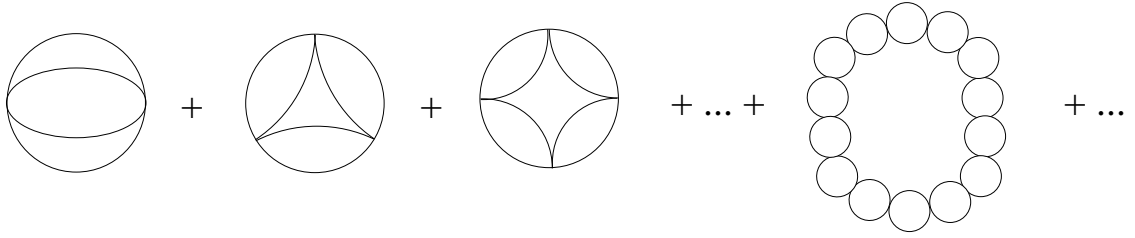


Figure C.8: Basketball graph and chains of pearls at next-to-leading order.

ϕ_i (or just one but with a factor of \sqrt{N} at each endpoint). For a background field pointing in the 1-direction the propagator becomes a σ line. So we have to resum a combination of bubble chains of all possible lengths and insertions made of a σ line and two background fields [Fig. C.7(c)].

Applying this insight to the (generic) NLO sunset graph in Fig. C.4(a) we can produce another three-loop vacuum graph of NLO. We take the two background “pins” and connect them to a propagator which produces a basketball graph of NLO. Furthermore, we can change any vertex in the basketball in the aforementioned manner — *i.e.* trade a local vertex for a fish insertion — to construct “pure” chains of pearls of arbitrary length (Fig. C.8).

C.1.3 Higher orders

We have already seen that the sunset graph in the effective action (Fig. C.4) contributes at NLO and NNLO depending on how the indices are contracted. The indices in the basketball graph (three-loop graph in Fig. C.8) can also be contracted such that it scales like $1/N$ (NNLO). With each additional loop in the chains of bubbles (Figs. C.7 and C.8) there is an additional possibility to contract indices at the vertex in a non-diagonal way similar to the bubble in Fig. C.3(b). So the more loops (and σ propagators with two background fields) there are in a graph the higher is the order of $1/N$ to which it *can* contribute if the indices are contracted appropriately.

Furthermore, there are generic vacuum graphs at NNLO that cannot be created with the procedures described up to here. Figure C.9 shows examples of such graphs.

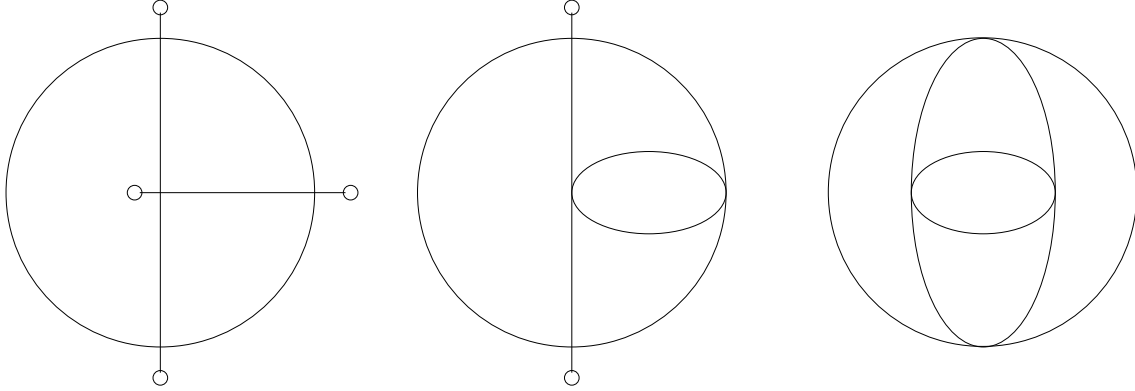


Figure C.9: Some generic NNLO graphs.

C.2 2PPI effective action

C.2.1 General formalism

The two-particle point-irreducible effective action consists of all graphs that do not fall apart when two lines meeting at the same vertex are cut (VERSHELDE and COPPENS, 1992). The effective action is a function of the expectation values

$$\phi_i = \langle \Phi_i \rangle \quad \text{and} \quad \Delta_{ij} = \langle \Phi_i \Phi_j \rangle$$

where Δ_{ij} is the expectation value of a *local* composite operator, *i.e.*, it is *not* a two-point GREEN function but resembles a loop with one (arbitrarily complicated) propagator. In EUCLIDEAN space-time the effective action is given by the expression

$$\Gamma[\phi, \Delta] = \mathcal{S}[\phi_i] - \frac{\lambda}{4N} \int_x (\Delta_{ii} \Delta_{jj} + 2 \Delta_{ij}^2) + \Gamma_q[\phi, \Delta]. \quad (\text{C.19})$$

The 2PPI formalism (VERSHELDE and COPPENS, 1992; VERSHELDE and DE PESSEMIER, 2002) suggests a shift of variables from Δ_{ij} to effective masses M_{ij}^2 in a HARTREE-FOCK-like way

$$M_{ij}^2(\phi) = (m^2 + \lambda\phi^2) \delta_{ij} + 2 \frac{\lambda}{N} \phi_i \phi_j + \frac{\lambda}{N} \left(\sum_k \Delta_{kk} + 2 \Delta_{ij} \right), \quad (\text{C.20})$$

so that the expectation values become explicit functions of ϕ_i and M_{ij}^2 . Without quantum correction, *i.e.* $\Gamma_q = 0$, the derivative with respect to the effective masses

$$\Delta = \text{[Diagram 1]} + \text{[Diagram 2]} + \text{[Diagram 3]} + \text{[Diagram 4]} + \text{[Diagram 5]} + \text{[Diagram 6]}$$

Figure C.10: Local mass correction Δ derived from 2PPI vacuum graphs. All but the first one are higher than leading order, *i.e.*, the propagator is modified at any order of $1/N$ by such a mass correction.

yields equations for the tree-level masses as in the propagator (C.4)

$$\frac{\delta\Gamma[\phi, M^2]}{\delta M_{ij}^2} = 0 \quad \Rightarrow \quad M_{ij}^2 = (m^2 + \lambda\phi^2) \delta_{ij} + 2 \frac{\lambda}{N} \phi_i \phi_j \quad (\text{C.21})$$

Taking all 2PPI graphs into account — except for the double bubble which is considered by the terms proportional to Δ^2 in Eq. (C.19) — the self-consistency condition for the effective masses becomes equal to Eq. (C.20) where the mass corrections are given by

$$\Delta_{ij} = 2 \frac{\delta\Gamma_q[M^2, \phi]}{\delta M_{ij}^2} . \quad (\text{C.22})$$

By comparison with Eq. (C.12) we observe that the resummation in Eq. (C.20) also incorporates the term $2 \frac{\lambda}{N} \Delta_{ij}$ which is $\mathcal{O}(N^{-1})$ or of NLO. Consequently the mass matrix, and also the corresponding one of the propagators, consists of terms of any order of $1/N$. Looking at the graphs that the local mass correction Δ_{ij} , defined by Eq. (C.22), consists of we conclude that the condition (C.20) incorporates the resummation of sunset- or basketball-type propagator insertions (Fig. C.10). Even when assuming that they are resummed diagonally they are of the same order as the pure sunset or basketball which means a mass correction of NLO that contributes to all orders when resummed. Therefore, in order to consistently describe the leading order of the $1/N$ expansion, we have to modify the formalism such that orders of $1/N$ are disentangled.

C.2.2 Leading order

For the leading order of a $1/N$ expansion we modify the term bilinear in Δ in the effective action such that it resembles the LO double-bubble term of Figure C.1(a). The only LO quantum corrections in Γ_q are the one-loop determinants. With a

σ - π decomposition the effective action at leading order reads

$$\begin{aligned} \Gamma^{\text{LO}}[\phi, M^2] &= N \mathcal{S}[\phi] + \frac{\lambda}{4N} [\Delta_\sigma + (N-1)\Delta_\pi]^2 \\ &+ \frac{1}{2} \text{Tr} \ln(\partial^2 + M_\sigma^2) + \frac{N-1}{2} \text{Tr} \ln(\partial^2 + M_\pi^2) . \end{aligned} \quad (\text{C.23})$$

The mass gap equations are

$$M_\sigma^2(\phi) = m^2 + 3\lambda\phi^2 + \frac{\lambda}{N} [\Delta_\sigma + (N-1)\Delta_\pi] \quad (\text{C.24a})$$

$$M_\pi^2(\phi) = m^2 + \lambda\phi^2 + \frac{\lambda}{N} [\Delta_\sigma + (N-1)\Delta_\pi] , \quad (\text{C.24b})$$

where the quantum corrections are the single bubbles

$$\Delta_\sigma = \int_k \frac{1}{k^2 + M_\sigma^2} \quad \text{and} \quad \Delta_\pi = \int_k \frac{1}{k^2 + M_\pi^2} \quad (\text{C.25})$$

so that we reproduce the results of Section C.1.1.

C.2.3 Next-to-leading order

At next-to-leading order we have to consider all 2PPI graphs discussed in Section C.1.2 which are the pearl necklaces (Fig. C.8), the NLO sunset [Fig. C.4(a)] and higher-loop sunset graphs (Fig. C.7). Furthermore we have to include the NLO double bubble graph

$$\Gamma_{\text{db}}^{\text{NLO}} = -\frac{\lambda}{2N} \Delta_{ij}^2 = -\frac{\lambda}{2N} [\Delta_\sigma^2 + (N-1)\Delta_\pi^2] . \quad (\text{C.26})$$

With these additional double bubble terms the mass gap equations (C.20) become

$$M_\sigma^2(\phi) = m^2 + 3\lambda\phi^2 + \frac{\lambda}{N} [3\Delta_\sigma + (N-1)\Delta_\pi] \quad (\text{C.27a})$$

$$M_\pi^2(\phi) = m^2 + \lambda\phi^2 + \frac{\lambda}{N} [\Delta_\sigma + (N+1)\Delta_\pi] . \quad (\text{C.27b})$$

They are similar to those of the HARTREE-FOCK approximation but the quantum corrections are determined by Eq. (C.22) and consist of arbitrarily complicated but *local* self-energy corrections. An explicit form of them is discussed in Section 8.2 and some of them are shown in Fig. C.10. Note that all of them except for the single (diagonal) bubble are of NLO. The analysis in Section C.1.2 has shown that a resummation of NLO mass corrections yields 1PI vacuum graphs of NNLO and higher. Therefore the NLO of a $1/N$ expansion of the 2PPI effective action (as investigated in Part II of this thesis) also produces 1PI graphs in the effective potential that are of NNLO and higher orders.

C.3 1PI effective action with an auxiliary field

C.3.1 The formalism

ROOT (1974) has performed a $1/N$ expansion of the effective action using an auxiliary field X to resum the bubbles as in Eqs. (C.13). It is introduced into the action (C.1) in the following manner

$$\begin{aligned}\mathcal{L}[\Phi, X] &= \mathcal{L}[\Phi] + \frac{N}{4\lambda} \left(X - \frac{\lambda}{N} \Phi_i^2 - m^2 \right)^2 \\ &= \frac{1}{2} (\partial_\mu \Phi_i)^2 + \frac{N}{4\lambda} X^2 - \frac{1}{2} X \Phi_i^2 - \frac{N}{2\lambda} m^2 X + \frac{N}{4\lambda} m^4.\end{aligned}\tag{C.28}$$

The field X acts like a LAGRANGE multiplier because it has no dynamics, *i.e.*, no kinetic term. Its equation of motion is an equation for the tree-level pion mass

$$X(\Phi) = m^2 + \frac{\lambda}{N} \Phi_i^2.\tag{C.29}$$

In order to compute the effective action we have to introduce expectation values and shift the fields

$$\Phi_i(x) = \langle \Phi_i \rangle + \varphi_i(x) = \left[\sqrt{N} \phi + \sigma(x) \right] \delta_{i1} + \pi_i(x) (1 - \delta_{i1})\tag{C.30}$$

$$X(x) = \langle X \rangle = \chi + \tilde{\chi}.\tag{C.31}$$

The second functional derivatives of the quadratic part of the shifted action form the inverse of the propagator matrix. Its entries are

$$i\mathcal{D}_{\sigma\sigma}^{-1}(\chi, \phi) = (-\partial^2 - X)\tag{C.32a}$$

$$i\mathcal{D}_{ij}^{-1}(\chi, \phi) = (-\partial^2 - X) \delta_{ij} \quad \text{with } i, j = 2, \dots, N\tag{C.32b}$$

$$i\mathcal{D}_{\chi\chi}^{-1}(\chi, \phi) = \frac{N}{2\lambda}\tag{C.32c}$$

$$i\mathcal{D}_{\chi\sigma}^{-1}(\chi, \phi) = -\phi\sqrt{N}.\tag{C.32d}$$

Inverting this matrix we find the relevant propagators (ROOT, 1974)

$$\mathcal{D}_{\sigma\sigma} = \frac{i}{k^2 - \chi - 2\lambda\phi^2}\tag{C.33a}$$

$$\mathcal{D}_{ij} = \frac{i}{k^2 - \chi} \delta_{ij} \quad \text{with } i, j = 2, \dots, N\tag{C.33b}$$

$$\mathcal{D}_{\chi\chi} = i \frac{2\lambda}{N} \frac{k^2 - \chi}{k^2 - \chi - 2\lambda\phi}\tag{C.33c}$$

$$\mathcal{D}_{\chi\sigma} = \frac{2\lambda\phi}{\sqrt{N}} \mathcal{D}_{\sigma\sigma}.\tag{C.33d}$$

The effective action consists of all 1PI vacuum graphs made of these propagators and the $\tilde{\chi}\varphi_i\varphi_i$ vertex that has no prefactor as can be seen already from the classical action (C.28). The $1/N$ counting rules are the following. A closed loop of φ fields yields a factor of N , a propagator $\mathcal{D}_{\chi\chi}$ a factor of $1/N$. A factor of $1/\sqrt{N}$ is associated with the mixed propagator $\mathcal{D}_{\chi\sigma}$ but graphs that involve this propagator are of NNLO and higher.

C.3.2 Leading order

The leading order of the $1/N$ expansion of the effective action is proportional to N and consists of the classical part

$$\Gamma_{\text{cl}}[\phi, \chi] = -\frac{N}{2} \chi \left(\phi^2 + \frac{m^2}{\lambda} - \frac{\chi}{2\lambda} \right), \quad (\text{C.34})$$

and the one-loop (pion) logarithms

$$\Gamma^{\text{LO}}[\phi, \chi] = \frac{i}{2} N \ln \det(-\partial^2 - \chi). \quad (\text{C.35})$$

The stationarity condition of the effective action

$$\left. \frac{\delta\Gamma[\chi, \phi]}{\delta\chi} \right|_{\chi=\chi(\phi)} = 0 \quad (\text{C.36})$$

produces Eq. (C.13b) in the limit $N \rightarrow \infty$

$$\chi(\phi) = m^2 + \lambda (\phi^2 + \Delta), \quad (\text{C.37})$$

where Δ denotes a single bubble derived from the equation

$$\Delta(\chi, \phi) = \frac{2}{N} \frac{\partial\Gamma^{\text{LO}}[\phi, \chi]}{\partial\chi}. \quad (\text{C.38})$$

The pion double bubble of Fig.C.1(a) is contained in the χ^2 terms in the classical part of the effective action (C.34) when χ is the solution of Eq. (C.37). All contributions with σ propagators are not of leading order in ROOT's strict $1/N$ counting.

C.3.3 Next-to-leading order

The one-loop logarithms that are not directly proportional to N are of next-to-leading order according to ROOT (1974). This is the difference of the σ and the pion loop

$$\Gamma_{1\text{-loop}}^{\text{NLO}}[\phi, \chi] = \frac{i}{2} \ln \det \frac{-\partial^2 - \chi - 2\lambda\phi^2}{-\partial^2 - \chi}. \quad (\text{C.39})$$

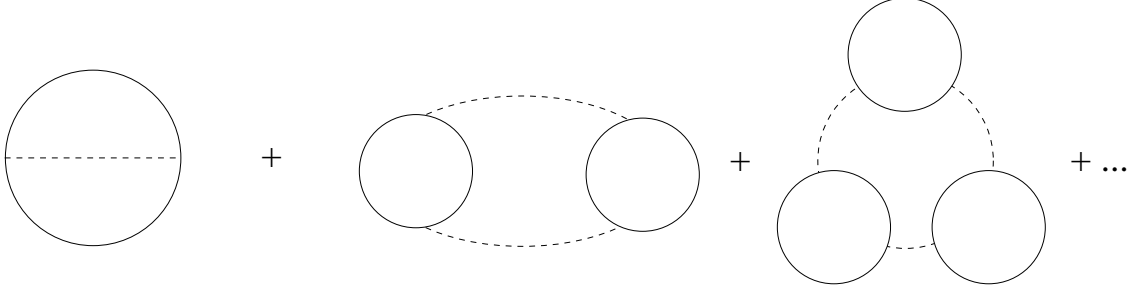


Figure C.11: NLO contributions in the auxiliary field formalism. Solid lines represent pion propagators and dashed lines $\chi\chi$ propagators.

All other NLO graphs are displayed in Figure C.11. They consist of φ (fish) loops which are connected to a chain by $\chi\chi$ propagators. The number of loops and $\chi\chi$ lines are identical so that all such graphs are of order $\mathcal{O}(N^0)$. Topologically, complete φ loops [with one σ and $(N - 1)$ pions] are allowed as well but they count like

$$\begin{aligned} \sum_{ij} \mathcal{D}_{\varphi_i\varphi_j}(x, y) \mathcal{D}_{\varphi_i\varphi_j}(x, y) &= [\mathcal{D}_{\sigma\sigma}(x, y)]^2 + (N - 1) [\mathcal{D}_{\pi\pi}(x, y)]^2 \\ &= N [\mathcal{D}_{\pi\pi}(x, y)]^2 + \mathcal{O}(N^0), \end{aligned} \quad (\text{C.40})$$

so that only their pion part is relevant at NLO. Expanding the graphs in Figure C.11 in terms of σ and pion lines one reproduces the graphs in Figures C.8 and C.7 but with all propagators being pion propagators with a mass χ .

The mixed π - σ double bubble from the expansion of the graph in Fig. C.1(a) (with a prefactor N^0) is taken into account as well but as an extra pion double bubble. It is contained in the sunset graph in Fig. C.11 when using the first term of the expansion

$$\mathcal{D}_{\chi\chi} = \frac{2\lambda}{N} \frac{i}{1 - 2\lambda\phi^2 \mathcal{D}_{\pi\pi}} = i \frac{2\lambda}{N} (1 + 2\lambda\phi^2 \mathcal{D}_{\pi\pi} \mp \dots)$$

where the χ propagator behaves like a vertex. The second term of this expansion applied to the same (sunset) graph in Fig. C.11 yields the NLO sunset graph [cf. Figure C.4(a)] but with only pion lines.

The stationarity condition (C.36) incorporates the derivative of all NLO graphs with respect to χ . The gap equation for the pion mass (C.37) implies a resummation of mass corrections

$$\Delta(\chi, \phi) = \frac{2}{N} \frac{\partial \Gamma[\chi, \phi]}{\partial \chi} = \frac{2}{N} \frac{\partial \Gamma^{\text{LO}}[\chi, \phi]}{\partial \chi} + \mathcal{O}(1/N). \quad (\text{C.41})$$

ROOT (1974) argues that the NLO of the effective action is to be computed by solving Eq. (C.37) to leading order because any NLO correction to χ contributes to the action only at NNLO. Hence, the effective action at NLO obtained in the 1PI auxiliary field formalism has only terms from LO and NLO and no higher corrections like *e.g.* the 2PPI effective action.

C.4 2PI effective action

C.4.1 General formalism

The 2PI effective action (CORNWALL *et al.*, 1974) is given by the expression

$$\Gamma[G, \phi] = \mathcal{S}[\phi] + \frac{1}{2}i\mathcal{D}_{ij}^{-1}G_{ij} + \frac{i}{2} \ln \det iG^{-1} + \Gamma_2[G, \phi] . \quad (\text{C.42})$$

The symbol Γ_2 represents all two-particle irreducible (2PI)¹ vacuum graphs with at least two loops. Among the graphs discussed in Section C.1 these are the double bubbles (Fig. C.1), the sunset with a bubble chain in the bottom part [Fig. C.7(b)], pure necklaces of bubbles (Fig. C.8) and higher-loop graphs (Fig. C.9). Any graph discussed in Section C.1 with more than one (explicit) σ line falls apart when cut twice.

The stationarity condition

$$\frac{\delta\Gamma[G, \phi]}{\delta G_{ij}} = 0$$

for the effective action is a DYSON-SCHWINGER equation for the propagator G that prescribes the resummation

$$iG_{ij}^{-1}(\phi; k) = i\mathcal{D}_{ij}^{-1}(\phi; k) - \Sigma_{ij}(G, \phi; k) \quad (\text{C.43})$$

where the self-energy is the functional derivative of the complete set of all 2PI graphs

$$\Sigma_{ij}(G, \phi; k) = 2i \frac{\delta\Gamma_2[G, \phi]}{\delta G_{ij}(\phi; k)} . \quad (\text{C.44})$$

If it contains 1PI graphs of NLO any graph computed using this propagator will contribute at all orders of $1/N$ due to the resummation condition (C.43), see Fig. C.6 for an example. A graphical comparison between the 2PI and the 2PPI formalism can be found in the literature (BAACKE and MICHALSKI, 2003a, Appendix B).

¹Graphs that do not fall apart if two arbitrary lines are cut.

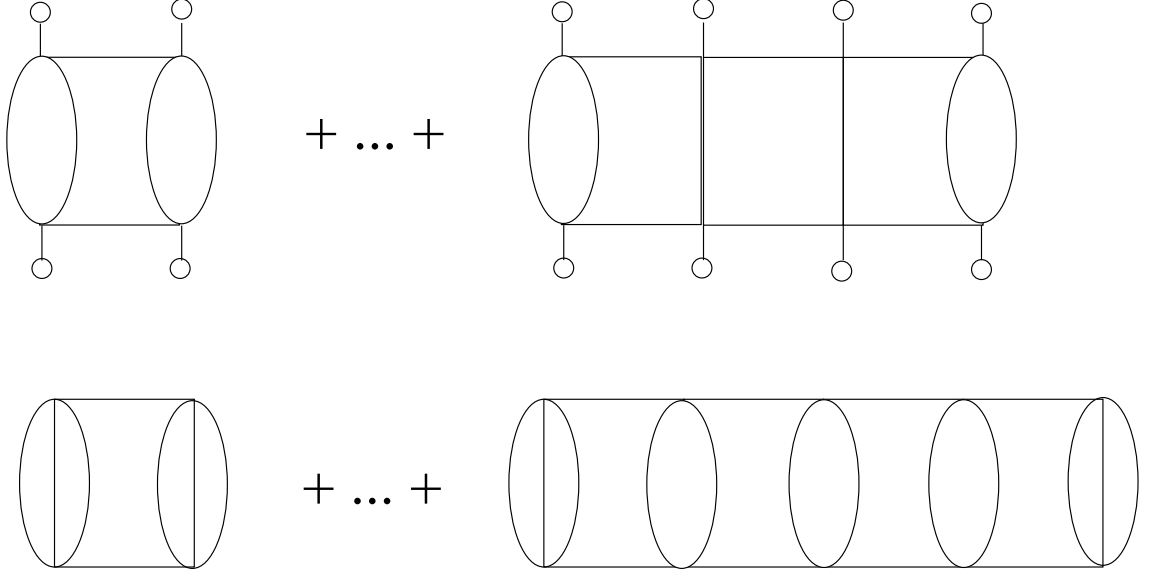


Figure C.12: Ladder graphs that arise from the resummation of non-local self-energies. The leftmost graph in the upper line is of NLO since it belongs to the class of chain graphs in Fig. C.7(c). All other graphs are beyond next-to-leading order. Mixtures of sunset and fish “rungs” are possible as well but not displayed.

In contrast to the resummation schemes dealt with in the preceding part of this Appendix, the 2PI formalism prescribes a resummation of non-local mass correction (self-energies) which produces 1PI ladder graphs with arbitrarily many rungs (Fig. C.12). Those ladders are of NNLO and higher as will be shown later.

C.4.2 Leading order

Leading-order contributions are those parts of the effective action that scale with N . With the usual expectation values (C.3) and the resulting σ - π distinction we obtain

$$\begin{aligned} \Gamma^{\text{LO}}[G, \phi] = & N \mathcal{S}[\phi] + \frac{1}{2} \text{Tr} \, i\mathcal{D}_\sigma^{-1} G_\sigma + \frac{N-1}{2} \text{Tr} \, i\mathcal{D}_\pi^{-1} G_\pi \\ & + \frac{i}{2} \ln \det iG_\sigma^{-1} + \frac{i}{2} (N-1) \ln \det iG_\pi^{-1} + \Gamma_2^{\text{LO}}[G, \phi] . \end{aligned} \quad (\text{C.45})$$

Higher-loop graphs are only double-bubbles

$$\Gamma_2^{\text{LO}}[G] = -i \frac{\lambda}{4N} \int_x [G_{ii}(x, x) G_{jj}(x, x)] = -i \frac{\lambda}{4N} \int_x [G_\sigma(x, x) + (N-1) G_\pi(x, x)]^2 . \quad (\text{C.46})$$

The corresponding matrix of self-energies is diagonal and of leading order

$$\Sigma_{ij}^{\text{LO}}(G, \phi) = 2i \frac{\delta \Gamma_2^{\text{LO}}}{\delta G_{ij}} = \frac{\lambda}{N} \sum_\ell \int_p G_{\ell\ell}(p) \delta_{ij} \sim N^0 \quad (\text{C.47})$$

which is in accordance with Eq. (C.12). The self-energies for the σ and the pion are identical.

C.4.3 Next-to-leading order

It is interesting to investigate what classes of graphs are involved at next-to-leading order of a *topological* $1/N$ expansion within the 2PI effective action formalism. One considers all 2PI graphs of NLO in a $1/N$ expansion but with full self-consistency required by a DYSON-SCHWINGER equation. This approximation is called 2PI-1/ N and has been studied by AARTS *et al.* (2002), ALFORD *et al.* (2004) and BERGES *et al.* (2005). Additional graphs in the effective action are the pearls (Fig. C.8) and generalized sunsets [Fig. C.7(b)].

The resummation of self-energy contributions obtained from NLO vacuum graphs produces 1PI graphs of *all* orders of $1/N$. The NLO vacuum graphs are all NLO graphs discussed in Section C.1.2 which are 2PI. So, if we truncate the 2PI effective action at NLO of the 2PI-1/ N expansion the error of the effective potential is $\mathcal{O}(\frac{1}{N})$ and that of the propagator $\mathcal{O}(\frac{1}{N^2})$ — the same estimate as in the other formalisms. Nevertheless, it is worthwhile to think about the resummation through the DYSON-SCHWINGER equation (C.43). As stated in Section C.4.1, its solution requires a ladder resummation of non-local self-energies. The first step of the iteration of the DYSON-SCHWINGER equation yields contributions to the propagator displayed in Fig. C.6. Plugging these into the one-loop determinants, *i.e.* closing them to a loop, generates 1PI graphs that are of NNLO and higher with one exception. The resummations of fish insertions with a σ propagator in between [Fig. C.6(a)] produces higher-loop sunset graphs with σ lines [Fig. C.7(c)] which are of NLO. So, the first step of the iteration of the DYSON-SCHWINGER equation is necessary for that the 1PI effective action contains all NLO graphs.

With a fully solved DYSON-SCHWINGER equation the error of the 2PI effective action at NLO of a 2PI-1/ N expansion is proportional to $1/N$ which is NNLO. However,

the graphs that contribute beyond NLO in the 2PI formalism are different to those in the 2PPI effective action.

C.4.4 Comparison with 1PI formalism

With a strict $1/N$ counting that does not equally treat σ and pion contributions it is possible to reconstruct the NLO result of the 1PI formalism with an auxiliary field. The price to pay is thermodynamic consistency of the 2PI effective action, *i.e.*, the equations for the propagators do not follow from the same effective action. This procedure has been carried out by RÖDER (2005) up to two loops of NLO.

After a σ - π decomposition the part of the effective action proportional to N lacks σ contributions entirely

$$\Gamma[\phi, G] = N \mathcal{S}[\phi] + \frac{N}{2} \text{Tr} \, i\mathcal{D}_\pi^{-1} G_\pi + \frac{i}{2} N \ln \det iG_\pi^{-1} - i \frac{\lambda}{4} N \int_x G_\pi^2(x, x) + \mathcal{O}(N^0) .$$

There are only pions and the effective action would coincide with the leading order of the 1PI formalism with an auxiliary field (cf. Section C.3.2) including the self-consistency condition.

The next order incorporates all contributions proportional to N^0 , *i.e.*, the σ trace and the σ logarithm in Eq. (C.45). With these terms there is also a DYSON-SCHWINGER equation for the σ propagator. Furthermore, we get sunsets [Figure C.7(b)] and bubble chains (Fig. C.8). All bubble chains are only made of pions ($N - 1$ pions plus one σ equal N pions plus terms of higher order). The only σ lines that occur in multiloop graphs are the single σ lines in the generalized sunsets [Fig. C.7(c)]. The double bubble graphs up to order N^0 are given by

$$\Gamma_2^{\text{db}}[G, \phi] = -i N \frac{\lambda}{4} \int_x G_\pi^2(x, x) - i \frac{\lambda}{2} \int_x G_\pi(x, x) G_\sigma(x, x) .$$

The DYSON-SCHWINGER equation for the self-energies of momentum p read

$$\Sigma_\sigma(p) = \lambda \int_k G_\pi(k) + N^0 \times \phi^2 \cdot [\text{pion bubble chains}](p) \quad (\text{C.48a})$$

$$\begin{aligned} \Sigma_\pi(p) &= \frac{N}{N-1} \lambda \int_k G_\pi(k) + \frac{\lambda}{N-1} \int_k G_\sigma + \frac{1}{N-1} \times \mathcal{O}(N^0) \\ &= \lambda \int_k G_\pi(k) + \mathcal{O}(1/N) . \end{aligned} \quad (\text{C.48b})$$

Approximating the DYSON-SCHWINGER equations to order N^0 may destroy thermodynamic consistency but it correctly reproduces 1PI graphs of order N and N^0 .

The one-loop σ logarithm (proportional to N^0)

$$\frac{i}{2}\text{Tr} \ln(\mathcal{D}_\sigma^{-1} - \Sigma_\sigma) = \frac{i}{2}\text{Tr} \ln \mathcal{D}_\sigma^{-1} + \frac{i}{2}\text{Tr} \ln(1 - \mathcal{D}_\sigma \Sigma_\sigma)$$

then resums the graphs in Fig. C.7(c) with but with pion bubbles. Note that, in spite of multiloop graphs in the effective action, there is no ladder resummation because the only non-local self-energy contributions are pion graphs in the σ self-energy.

One might suspect that corrections of order $1/N$ to the pion self-energy could contribute to the effective action at order N^0 (by plugging these corrections into LO graphs). But such corrections do not occur because the generated 1PI graphs are the same as in the 1PI auxiliary-field formalism. The error in the effective action in this approximation is also $\mathcal{O}(N^{-1})$.

C.5 Conclusion

The analysis in this Appendix has shown each method of generating 1PI graphs in a $1/N$ expansion of the effective action has errors of NNLO if it is performed up to NLO. For sufficiently large N all resummation schemes should yield the same result. In a computation of critical exponents in the $O(N)$ model ALFORD *et al.* (2004) have shown that for small N , the 2PI- $1/N$ expansion at NLO converges faster to the true result than the 1PI-NLO expansion. A calculation in two dimensions (see also BAACKE and MICHALSKI, 2004a) shows that the 2PPI effective potential at NLO rather behaves like the one in the HARTREE-FOCK approximation than like its 2PI or 1PI counterpart; it exhibits spontaneous symmetry breaking in two dimensions, an unphysical feature (cf. Chapter 9).

C

Bibliography

- G. AARTS *et al.*, 2002. *Far-from-equilibrium dynamics with broken symmetries from the $2PI-1/N$ expansion*. Phys. Rev. **D66**, 045008. hep-ph/0201308.
- M. ALFORD, J. BERGES and J. M. CHEYNE, 2004. *Critical phenomena from the two-particle irreducible $1/N$ expansion*. Phys. Rev. **D70**, 125002. hep-ph/0404059.
- B. ALLÉS, M. D'ELIA and A. DI GIACOMO, 1997. *Topological susceptibility at zero and finite T in $SU(3)$ Yang-Mills theory*. Nucl. Phys. **B494**, 281–292. Erratum-ibid. **B679**, 397 (2004), hep-lat/9605013.
- B. ALLÉS *et al.*, 1999. *Topological properties of full QCD at the phase transition*. Nucl. Phys. Proc. Suppl. **73**, 518–520. hep-lat/9808004.
- G. AMELINO-CAMELIA, 1997. *Thermal effective potential of the $O(N)$ linear sigma model*. Phys. Lett. **B407**, 268–274. hep-ph/9702403.
- G. AMELINO-CAMELIA and S.-Y. PI, 1993. *Selfconsistent improvement of the finite temperature effective potential*. Phys. Rev. **D47**, 2356–2362. hep-ph/9211211.
- J. O. ANDERSEN, D. BOER and H. J. WARRINGA, 2004. *Thermodynamics of $O(N)$ sigma models: $1/N$ corrections*. Phys. Rev. **D70**, 116007. hep-ph/0408033.
- Y. AOKI *et al.*, 2006. *The QCD transition temperature: Results with physical masses in the continuum limit* hep-lat/0609068.
- J. BAACKE and S. MICHALSKI, 2003a. *The $O(N)$ linear sigma model at finite temperature beyond the Hartree approximation*. Phys. Rev. **D67**, 085006. hep-ph/0210060.
- J. BAACKE and S. MICHALSKI, 2003b. *$O(N)$ linear sigma model beyond the Hartree approximation at finite temperature*. In K. A. MILTON (Editor), *Quantum field*

- theory under the influence of external conditions (QFEXT'03)*, pages 282–287. Norman, Oklahoma, Rinton Press. [hep-ph/0312031](#).
- J. BAACKE and S. MICHALSKI, 2004a. *The 2PI finite temperature effective potential of the $O(N)$ linear sigma model in 1+1 dimensions, at next-to-leading order in $1/N$* . Phys. Rev. **D70**, 085002. [hep-ph/0407152](#).
- J. BAACKE and S. MICHALSKI, 2004b. *Scalar $O(N)$ model at finite temperature: 2PI effective potential in different approximations*. In K. J. ESKOLA *et al.* (Editors), *Strong and electroweak matter (SEWM) 2004*, pages 401–405. Helsinki, World Scientific. [hep-ph/0409153](#).
- W. A. BARDEEN and M. MOSHE, 1983. *Phase structure of the $O(N)$ vector model*. Phys. Rev. **D28**, 1372.
- W. A. BARDEEN and M. MOSHE, 1986. *Comment on the finite temperature behavior of $\lambda(\phi^2)^2$ in four-dimensions theory*. Phys. Rev. **D34**, 1229–1231.
- G. BAYM and G. GRINSTEIN, 1977. *Phase transition in the sigma model at finite temperature*. Phys. Rev. **D15**, 2897–2912.
- J. BERGES *et al.*, 2005. *Renormalized thermodynamics from the 2PI effective action*. Phys. Rev. **D71**, 105004. [hep-ph/0409123](#).
- C. W. BERNARD *et al.*, 1997. *Which chiral symmetry is restored in high temperature QCD?* Phys. Rev. Lett. **78**, 598–601. [hep-lat/9611031](#).
- J. VAN DER BIJ and M. J. G. VELTMAN, 1984. *Two Loop Large Higgs Mass Correction to the ρ Parameter*. Nucl. Phys. **B231**, 205.
- J.-P. BLAIZOT, E. IANCU and U. REINOSA, 2004. *Renormalization of Φ -derivable approximations in scalar field theories*. Nucl. Phys. **A736**, 149–200. [hep-ph/0312085](#).
- A. BOCHKAREV and J. I. KAPUSTA, 1996. *Chiral symmetry at finite temperature: linear vs nonlinear σ -models*. Phys. Rev. **D54**, 4066–4079. [hep-ph/9602405](#).
- E. BRAATEN and R. D. PISARSKI, 1990a. *Resummation and gauge invariance of the gluon damping rate in hot QCD*. Phys. Rev. Lett. **64**, 1338.
- E. BRAATEN and R. D. PISARSKI, 1990b. *Soft amplitudes in hot gauge theories: a general analysis*. Nucl. Phys. **B337**, 569.

-
- H. C. G. CALDAS, A. L. MOTA and M. C. NEMES, 2001. *The chiral fermion meson model at finite temperature*. Phys. Rev. **D63**, 056011. hep-ph/0005180.
- S. CHANDRASEKHARAN *et al.*, 1999. *Anomalous chiral symmetry breaking above the QCD phase transition*. Phys. Rev. Lett. **82**, 2463–2466. hep-lat/9807018.
- S.-J. CHANG, 1976. *The existence of a second-order phase transition in the two-dimensional ϕ^4 field theory*. Phys. Rev. **D13**, 2778.
- P. CHEN *et al.*, 1998. *Toward the chiral limit of QCD: Quenched and dynamical domain wall fermions* hep-lat/9812011.
- S. CHIKU and T. HATSUDA, 1998. *Optimized perturbation theory at finite temperature*. Phys. Rev. **D58**, 076001. hep-ph/9803226.
- M. C. CHU and S. SCHRAMM, 1995. *Instanton content of finite temperature QCD matter*. Phys. Rev. **D51**, 4580–4586. nucl-th/9412016.
- M. C. CHU *et al.*, 2000. *Temperature dependence of instantons in QCD*. Phys. Rev. **D62**, 094508. hep-lat/9712023.
- S. R. COLEMAN, 1973. *There are no Goldstone bosons in two-dimensions*. Commun. Math. Phys. **31**, 259–264.
- S. R. COLEMAN, 1975. *Quantum sine-Gordon equation as the massive Thirring model*. Phys. Rev. **D11**, 2088.
- S. R. COLEMAN, R. JACKIW and H. D. POLITZER, 1974. *Spontaneous symmetry breaking in the $O(N)$ model for large N* . Phys. Rev. **D10**, 2491.
- S. R. COLEMAN and E. WEINBERG, 1973. *Radiative corrections as the origin of spontaneous symmetry breaking*. Phys. Rev. **D7**, 1888–1910.
- J. C. COLLINS and M. J. PERRY, 1975. *Superdense matter: neutrons or asymptotically free quarks?* Phys. Rev. Lett. **34**, 1353.
- F. COOPER, B. MIHAILA and J. F. DAWSON, 2004. *Renormalizing the Schwinger-Dyson equations in the auxiliary field formulation of $\lambda\phi^4$ field theory* hep-ph/0407119.
- J. M. CORNWALL, R. JACKIW and E. TOMBOULIS, 1974. *Effective action for composite operators*. Phys. Rev. **D10**, 2428–2445.

- P. COSTA *et al.*, 2004. *Effective restoration of the $U(1)_A$ symmetry with temperature and density*. Phys. Rev. **D70**, 116013. [hep-ph/0408177](#).
- P. COSTA *et al.*, 2005. *Analysis of the $U(1)_A$ symmetry-breaking and restoration effects on scalar-pseudoscalar spectrum*. Phys. Rev. **D71**, 116002. [hep-ph/0503258](#).
- L. DOLAN and R. JACKIW, 1974a. *Symmetry behavior at finite temperature*. Phys. Rev. **D9**, 3320–3341.
- L. DOLAN and R. JACKIW, 1974b. *Symmetry behavior at finite temperature*. Phys. Rev. **D9**, 3320–3341.
- S. EIDELMAN *et al.* (Particle Data Group), 2004. *Review of particle physics*. Phys. Lett. **B592**, 1. URL <http://pdg.lbl.gov>.
- Z. FODOR and S. D. KATZ, 2004. *Critical point of QCD at finite T and μ , lattice results for physical quark masses*. JHEP **04**, 050. [hep-lat/0402006](#).
- P. DE FORCRAND and O. PHILIPSEN, 2002. *The QCD phase diagram for small densities from imaginary chemical potential*. Nucl. Phys. **B642**, 290–306. [hep-lat/0205016](#).
- R. GAVAI and S. GUPTA, 2006a. *The critical end point of quantum chromodynamics*. PoS **LAT2005**, 160. [hep-lat/0509151](#).
- R. V. GAVAI and S. GUPTA, 2006b. *The critical end point in QCD* [hep-lat/0608022](#).
- H. B. GEDDES, 1980. *The spin-0 mass spectrum in the one-loop approximation in a linear $SU(4)$ sigma model*. Phys. Rev. **D21**, 278.
- M. GELL-MANN and M. LEVY, 1960. *The axial vector current in beta decay*. Nuovo Cim. **16**, 705.
- H. C. DE GODOY CALDAS, 2002. *Dressing a scalar mass up to two-loop order at finite temperature*. Phys. Rev. **D65**, 065005. [hep-th/0111194](#).
- S. A. GOTTLIEB *et al.*, 1997. *Thermodynamics of lattice QCD with two light quark flavours on a $16^3 \times 8$ lattice. II*. Phys. Rev. **D55**, 6852–6860. [hep-lat/9612020](#).
- D. J. GROSS and F. WILCZEK, 1973. *Ultraviolet behavior of non-Abelian gauge theories*. Phys. Rev. Lett. **30**, 1343–1346.

-
- M. A. HALASZ *et al.*, 1998. *On the phase diagram of QCD*. Phys. Rev. **D58**, 096007. hep-ph/9804290.
- S. HANDS, 2001. *The phase diagram of QCD*. Contemp. Phys. **42**, 209–225. physics/0105022.
- H. VAN HEES and J. KNOLL, 2002a. *Renormalization in self-consistent approximation schemes at finite temperature. III: Global symmetries*. Phys. Rev. **D66**, 025028. hep-ph/0203008.
- H. VAN HEES and J. KNOLL, 2002b. *Renormalization in self-consistent approximations schemes at finite temperature. I: Theory*. Phys. Rev. **D65**, 025010. hep-ph/0107200.
- H. VAN HEES and J. KNOLL, 2002c. *Renormalization of self-consistent approximation schemes. II: Applications to the sunset diagram*. Phys. Rev. **D65**, 105005. hep-ph/0111193.
- G. 'T HOOFT, 1976a. *Computation of the quantum effects due to a four- dimensional pseudoparticle*. Phys. Rev. **D14**, 3432–3450.
- G. 'T HOOFT, 1976b. *Symmetry breaking through Bell-Jackiw anomalies*. Phys. Rev. Lett. **37**, 8–11.
- G. 'T HOOFT and M. J. G. VELTMAN, 1972. *Regularization and renormalization of gauge fields*. Nucl. Phys. **B44**, 189–213.
- R. JACKIW, 1974. *Functional evaluation of the effective potential*. Phys. Rev. **D9**, 1686.
- F. KARSCH, 2002. *Lattice QCD at high temperature and density*. Lect. Notes Phys. **583**, 209–249. hep-lat/0106019.
- D. A. KIRZHNITS and A. D. LINDE, 1975. *A Relativistic phase transition*. Sov. Phys. JETP. **40**, 628.
- J. B. KOGUT, J. F. LAGAE and D. K. SINCLAIR, 1998. *Topology, fermionic zero modes and flavor singlet correlators in finite temperature QCD*. Phys. Rev. **D58**, 054504. hep-lat/9801020.
- E. LAERMANN and O. PHILIPSEN, 2003. *Status of lattice QCD at finite temperature*. Ann. Rev. Nucl. Part. Sci. **53**, 163–198. hep-ph/0303042.

- J. T. LENAGHAN and D. H. RISCHKE, 2000. *The $O(N)$ model at finite temperature: Renormalization of the gap equations in Hartree and large- N approximation.* J. Phys. **G26**, 431–450. [nucl-th/9901049](#).
- J. T. LENAGHAN, D. H. RISCHKE and J. SCHAFFNER-BIELICH, 2000. *Chiral symmetry restoration at nonzero temperature in the $SU(3)_r \times SU(3)_l$ linear sigma model.* Phys. Rev. **D62**, 085008. [nucl-th/0004006](#).
- H. LEUTWYLER, 1994. *On the foundations of chiral perturbation theory.* Ann. Phys. **235**, 165–203. [hep-ph/9311274](#).
- S. P. MARTIN and D. G. ROBERTSON, 2006. *TSIL: A program for the calculation of two-loop self-energy integrals.* Comput. Phys. Commun. **174**, 133–151. [hep-ph/0501132](#).
- S. MICHALSKI, 2006. *Chiral and $U(1)$ axial symmetry restoration in linear sigma models with two quark flavors* [hep-ph/0601255](#).
- Á. MÓCSY, I. N. MISHUSTIN and P. J. ELLIS, 2004. *Role of fluctuations in the linear sigma model with quarks.* Phys. Rev. **C70**, 015204. [nucl-th/0402070](#).
- B. MÜLLER, 2005. *Quark matter 2005: Theoretical summary* [nucl-th/0508062](#).
- Y. NEMOTO, K. NAITO and M. OKA, 2000. *Effective potential of $O(N)$ linear sigma model at finite temperature.* Eur. Phys. J. **A9**, 245–259. [hep-ph/9911431](#).
- R. R. PARWANI, 1992. *Resummation in a hot scalar field theory.* Phys. Rev. **D45**, 4695–4705. [hep-ph/9204216](#).
- A. PATKÓS, Z. SZÉP and P. SZÉPFALUSY, 2002. *Finite temperature spectral functions of the linear $O(N)$ model at large N applied to the π - σ system.* Phys. Lett. **B537**, 77–85. [hep-ph/0202261](#).
- N. PETROPOULOS, 1999. *Linear sigma model and chiral symmetry at finite temperature.* J. Phys. **G25**, 2225–2241. [hep-ph/9807331](#).
- R. D. PISARSKI, 1988. *Computing finite temperature loops with ease.* Nucl. Phys. **B309**, 476.
- R. D. PISARSKI and F. WILCZEK, 1984. *Remarks on the chiral phase transition in chromodynamics.* Phys. Rev. **D29**, 338–341.
- H. D. POLITZER, 1973. *Reliable perturbative results for strong interactions?* Phys. Rev. Lett. **30**, 1346–1349.

- D. H. RISCHKE, 2004. *The quark-gluon plasma in equilibrium*. Prog. Part. Nucl. Phys. **52**, 197–296. nucl-th/0305030.
- D. RÖDER, 2005. *Selfconsistent calculations of sigma-meson properties at finite temperature* hep-ph/0509232.
- D. RÖDER, J. RUPPERT and D. H. RISCHKE, 2003. *Chiral symmetry restoration in linear sigma models with different numbers of quark flavors*. Phys. Rev. **D68**, 016003. nucl-th/0301085.
- D. RÖDER, J. RUPPERT and D. H. RISCHKE, 2005. *Selfconsistent calculations of spectral densities in the $O(N)$ model: Improving the Hartree-Fock approximation by including nonzero decay widths* hep-ph/0503042.
- H.-S. ROH and T. MATSUI, 1998. *Chiral phase transition at finite temperature in the linear sigma model*. Eur. Phys. J. **A1**, 205–220. nucl-th/9611050.
- R. G. ROOT, 1974. *Effective potential for the $O(N)$ model to order $1/N$* . Phys. Rev. **D10**, 3322.
- J. SCHAFFNER-BIELICH, 2000. *Effective restoration of the $U(1)_A$ symmetry in the $SU(3)$ linear sigma model*. Phys. Rev. Lett. **84**, 3261. hep-ph/9906361.
- S. SCHERER and M. R. SCHINDLER, 2005. *A chiral perturbation theory primer* hep-ph/0505265.
- H. J. SCHNITZER, 1974. *Nonperturbative effective potential for $\lambda\phi^4$ theory in the many-field limit*. Phys. Rev. **D10**, 1800.
- G. SMET *et al.*, 2002. *A 2-loop 2PPI analysis of $\lambda\phi^4$ at finite temperature*. Phys. Rev. **D65**, 045015. hep-th/0108163.
- C. VAFA and E. WITTEN, 1984. *Restrictions on symmetry breaking in vector-like gauge theories*. Nucl. Phys. **B234**, 173.
- H. VERSCHELDE, 2001. *Summation and renormalization of bubble graphs to all orders*. Phys. Lett. **B497**, 165–171. hep-th/0009123.
- H. VERSCHELDE and M. COPPENS, 1992. *A variational approach to quantum field theory*. Phys. Lett. **B287**, 133–137.
- H. VERSCHELDE and M. COPPENS, 1993. *General analysis of n loop corrections in the 2PPI variational approach to $\lambda\phi^4$* . Z. Phys. **C58**, 319–323.

- H. VERSHELDE and J. DE PESSEMIER, 2002. *Study of the $O(N)$ linear sigma model at finite temperature using the 2PPI expansion.* Eur. Phys. J. **C22**, 771–779. hep-th/0009241.